ABSTRACT

Title of dissertation: THEORETICAL INVESTIGATION OF
COLLISIONS OF CH$_2$ WITH He: ENERGY
TRANSFER WITHIN AND BETWEEN THE
$\tilde{a}$ AND $\tilde{X}$ ELECTRONIC STATES OF CH$_2$

Lifang Ma, Doctor of Philosophy, 2014

Dissertation directed by: Professor Millard H. Alexander
Department of Chemistry and Biochemistry;
Institute for Physical Science and Technology

Adjunct Professor Paul J. Dagdigian
Department of Chemistry and Biochemistry

This dissertation focuses on energy transfer (rotational, vibrational, and electronic) of CH$_2$ in its ground and first excited electronic states ($\tilde{X}\,^3B_1$ and $\tilde{a}\,^1A_1$), by collisions with the helium atom.

Initially we investigate energy transfer within the two electronic states separately. We carry out *ab initio* calculations to determine the potential energy surfaces for the interaction of He with CH$_2$ in these two states. The PES for He–CH$_2(\tilde{a})$ is more anisotropic than for He–CH$_2(\tilde{X})$. In the former case we perform quantum scattering calculations and report state-to-state and overall removal cross sections, from which we compute room temperature rate constants.

For He–CH$_2(\tilde{X})$ we determined the dependence of the PES on the CH$_2$ bending degree of freedom. By averaging over the bending vibrational wave functions, we were able to investigate collisional relaxation of both rotation and the molecular

bending. The PES of the $\tilde{X}$ state is less anisotropic than that of the $\tilde{a}$ state, resulting in a less efficient relaxation process. Vibrational relaxation is very inefficient, with cross sections less than 1% of those for rotational relaxation.

By taking into account the weak spin-orbit coupling between the $\tilde{a}$ and $\tilde{X}$ states, we explore collision-induced electronically inelastic processes. We invoke, the mixed-state model, in which transitions are due entirely to the mixing of nearly-degenerate pairs of rotational levels. We compare the computed removal rate constants with experimental results by Hall and Sears at Brookhaven.

Finally, we simulate the time evolution of the singlet-triplet relaxation of CH_2 by solving the relaxation master equation. The simulation shows that relaxation occurs in three stages: immediate re-distribution between the two mixed states, fast rotational relaxation within the $\tilde{a}$ state and a much slower relaxation within the $\tilde{X}$ state. Eventually, most of the population relaxes to the $\tilde{X}$ state.

Theoretical Investigation of Collisions of CH_2 with He:
Energy Transfer within and between the
$\tilde{a}$ and $\tilde{X}$ Electronic States of CH_2

by

Lifang Ma

Dissertation submitted to the Faculty of the Graduate School of the
University of Maryland, College Park in partial fulfillment
of the requirements for the degree of
Doctor of Philosophy
2014

Advisory Committee:
Professor Millard H. Alexander, Chair/Advisor
Professor Paul J. Dagdigian, Advisor
Professor Russell R. Dickerson
Professor Amy Mullin
Professor John D. Weeks

Acknowledgments

First and foremost I want to express my deepest gratitude to my advisor, Professor Millard Alexander, for his continuous support and help during this long journey. I appreciate all his time, advice, and especially, encouragement in supporting me to complete my PhD. It would be impossible to finish this dissertation as well as all the work presented in this dissertation without his patient guidance and consideration.

My sincere gratitude is reserved for Professor Paul Dagdigian, for his generous help and advice from the very beginning of this work, and for his time and unmatched work in modifying the HIBRIDON code which made our calculations possible. I am blessed to have such an enriching experience working with Professor Alexander and Professor Dagdigian.

I am very grateful to other members of my advisory committee, who are more than generous with their expertise and time. I also want to thank all professors taught me in last a few years, especially Dr. Robert Walker, Dr. Amy Mullin, Dr. Yuhuang Wang and Dr. Paulo Bedaque, for teaching me knowledge in advanced physical chemistry and physics that is frequently used in my research.

Thanks to the Hall and Sears group at Brookhaven National Laboratory, who kindly shared their data with us, held two information meetings for us, and always patiently wrote long emails in discussing problems. I also want to thank Professor Per Jensen for sharing us data on the ro-vibrational energies of CH_2. I am appreciative of the support from other members (especially, Dr. Jacek Klos, Mick Warehime

and Qianli Ma) in the Alexander Group and the Dagdigian Group.

Special thanks go to my lovely roommates and friends at Maryland, without whom I would have lost a lot of fun in traveling, sports, and most importantly, enjoying homemade food.

Last but not least I want to thank my parents, my brother and my dear husband, who are standing behind me and backing me up in all circumstances, for their love and support. It makes me feel that I am the luckiest and happiest person in the world, for being their family.

Table of Contents

List of Tables

List of Figures

List of Abbreviations

CCSD(T)	Coupled Cluster Method with Inclusion of Single, Double, and (Perturbatively) Triple Excitations
CIISC	Collision-Induced Intersystem Crossing
JCP	Journal of Chemical Physics
MO	Molecular Orbital
PES	Potential Energy Surface
RCCSD(T)	Restricted Coupled Cluster Method with Inclusion of Single, Double, and (Perturbatively) Triple Excitations
RET	Rotational Energy Transfer

Chapter 1:   Overview

The subject of this dissertation is collisions of CH_2 molecules with He. The goal is the investigation of collision-induced relaxation within and between the two lowest electronic states of CH_2: the ground $\tilde{X}^3B_1$ state and the first excited $\tilde{a}^1A_1$ state. First, we investigate relaxation within each state separately. We then model electronic energy transfer between these two states by including the weak spin-orbit coupling between them.

The triatomic molecule CH_2 is an important intermediate in organic synthesis [1–3], chemical combustion [4,5] and atmospheric photochemistry [6–8]. The $\tilde{a}$ and the $\tilde{X}$ states of CH_2 should be considered as two different species because of their significantly different reactivities [9]. Collisional transfer between these states is crucial to understanding the chemistry of CH_2. Bley and Temps [10] applied the "mixed-state model" to study this intersystem crossing, determining the degree of mixing for pairs of accidentally degenerate rotational levels. Hall, Sears and co-workers [11–14] studied experimentally the role of these mixed states in collisions of CH_2 with noble gases. Recent measurements by Gannon, Seakins and co workers [15] further support the assumptions of the "mixed-state model". Since spectroscopists designate transitions between states of different multiplicity as "intersystem cross-

ing" [16], we shall designate the collisional analogue as "collision-induced intersystem crossing".

Prior to the description of our three major research projects (Chapters 4, 5, 6), we include two introductory chapters. The first, Chapter 2 reviews briefly the electronic structure and ro-vibrational level structure of the $^3\tilde{X}$ and $^1\tilde{a}$ states of CH_2, the "mixed-state model" for collision-induced transitions between these two states, and, in conclusion, a review of relevant experiments. Chapter 3 introduces the methods we used for the *ab initio* calculations of the CH_2-He potential energy surfaces and the subsequent quantum scattering calculations.

Motivated by work in the group of Hall and Sears at Brookhaven, we initially investigated (Chapter 4) rotationally inelastic collisions of $CH_2(\tilde{a})$ with the helium atom. [17] We determined accurate potential energy surfaces (PES) for the interaction between $CH_2(\tilde{a})$ and He, treating the CH_2 molecule as rigid with a fixed bond length and a fixed bending angle. We then carried out quantum scattering calculations of state-to-state and the overall inelastic cross sections. From these, we calculated room temperature rate constants as a thermal average of the energy dependence of these cross sections.

Following the study of the $\tilde{a}$ state, we investigated (Chapter 5) rotational energy transfer within the ground $\tilde{X}^3B_1$ state. [18] In contrast to our study of $CH_2(\tilde{a})$, because of the low barrier to linearity in the $CH_2(\tilde{X})$ state, [19] we allowed the bond angle to vary in the *ab initio* calculations. We then averaged the PES over the bond angle, weighting by the square of the bending wave function.

For the $\tilde{X}$ state, we carried out separate scattering calculations for rotational

transitions within each of the four lowest bending vibrational manifolds $(0,v_2,0)$ $[v_2 = 0, 1, 2, 3]$. From this we determined the dependence of the rotational inelasticity (both state-to-state cross sections and room-temperature rate constants) on the bending vibrational quantum number. Both the cross sections, and, consequently, the rate constants, were found to be smaller than those of the $\tilde{a}$ state.

Subsequently, again for the $\tilde{X}$ state, we included the small coupling between rotational levels associated with different bending vibrational levels to investigate the ro-vibrational relaxation, also described in Chapter 5. Ro-vibrational relaxation of $CH_2(\tilde{X})$ was found to be several orders of magnitude less efficient than rotational relaxation within a given bending vibrational manifold.

In Chapter 6 we present results on collision-induced transitions between the $\tilde{a}^1$ state and the $\tilde{X}^3$ state. To treat collision-induced intersystem crossing, we adopted the "gateway" model [10]. The spin-orbit coupling between the $\tilde{a}$ and $\tilde{X}$ states of the isolated CH_2 molecule is weak. Nevertheless, this coupling becomes significant whenever the energy gap between two levels of the same rotational quantum number in the two electronic states is less than the magnitude of this spin-orbit coupling. The mixing between a pair of nearly degenerate "gateway" (or mixed) states allows transitions between the full rotational manifolds of both the $\tilde{a}$ and the $\tilde{X}$ states.

Subsequently, we solve the relaxation master equation to simulate the time-dependent relaxation of these coupled singlet-triplet manifolds. This multilevel relaxation encompasses three distinct steps: (i) immediate re-distribution among the two mixed states, (ii) fast rotational relaxation within the $\tilde{a}$ state, and (iii) slower rotational relaxation within the $\tilde{X}$ state.

Finally, following the technical material in Chaps. 4–6, we conclude with a short summary and discussion. Some technical material is contained in Appendices A and B.

The two studies on rotational inelastic collisions within the two electronic states, Chap. 4 and a major fraction of Chap. 5 of this dissertation, have been published in the Journal of Chemical Physics (JCP):

[1] L. Ma, M. H. Alexander and P. J. Dagdigian, *Theoretical investigation of rotationally inelastic collisions of* $CH_2(\tilde{a})$ *with helium*, J. Chem. Phys. **134**, 154307 (2011). [17]

[2] L. Ma, P. J. Dagdigian and M. H. Alexander, *Theoretical investigation of rotationally inelastic collisions of* $CH_2(\tilde{X})$ *with helium*, J. Chem. Phys. **136**, 224306 (2012). [18]

Chapter 2:   Methylene

2.1   General Considerations

Methylene (CH_2), a small molecule with only six valence electrons, is an impor-
tant intermediate in organic synthesis [1–3], chemical combustion [4,5] and planetary
photochemistry [6–8]. The molecule is the simplest carbene, one of the most reactive
intermediates in organic chemistry. [1] The highest two filled molecular orbitals of
CH_2 are, in linear geometry, the non-bonding $2p_x$ and $2p_y$ atomic orbitals on the C
atom (we assume that the linear molecule defines the z axis). In singlet CH_2 one of
these orbitals is doubly occupied, and the other unoccupied, so that it can react as
either an electron donor or an electron acceptor. In the ground triplet state, each
of these orbitals is singly occupied. The ground state behaves as a diradical which
can dimerize and quickly form ethylene. In both insertion and addition reactions
(to multiple bonds), the mechanisms for reactions of the singlet and triplet carbenes
are quite distinct. [2,3]

In combustion environments, the $\tilde{a}$ state CH_2 reacts rapidly with radicals
as well as with many stable molecules, including but not limited to O_2 [20–22],
NO [21, 22], N_2 [21], CO [21], CH_4 [21, 23, 24] and H_2 [20, 21, 23, 25]. The $\tilde{X}$ state
reacts only with a few very reactive species like O, O_2 [22, 26, 27], NO [26, 28] and

5

C_2H_2 [29], but at a slower rate compared to the singlet. [4, 5, 9]

In planetary atmospheres, methylene is a common product of the photochemical destruction of methane. On the outer Jovian planets (Jupiter, Saturn, Uranus and Neptune), CH_2, in both singlet and triplet states, forms by Lyman α dissociation of methane. On these planets the more reactive $\tilde{a}$ state reacts rapidly with H_2 to produce another reactive radical: CH_3. The less reactive $\tilde{X}$ state reacts with this CH_3. The CH_2 molecule also acts as an intermediate in the reforming of hydrocarbons.

By contrast, on planets with nitrogen atmospheres (Titan, for example) the hydrocarbon cycle completes in a significantly different way. Here, collisions of the $\tilde{a}$ state with N_2 lead to rapid intersystem crossing, so that the $\tilde{a}$ state CH_2 radicals are no longer available to react with H_2. This affects the entire hydrocarbon cycle. [7, 8]

Since the reactivities of CH_2 in its ground triplet and first excited singlet states are so different, [9, 30] these two states are often treated as distinct species in kinetic simulations. Thus, understanding the collisional relaxation of each electronic state, as well collision-induced intersystem crossing between them, is essential in a proper modeling of reaction networks involving methylene.

2.2 Structure and Rotational Levels of CH_2

2.2.1 Electronic Structure

The structure of CH_2 is similar to that of one of our most familiar molecules: H_2O. A triatomic with two equivalent H atoms, CH_2 molecule is planar with a C_2
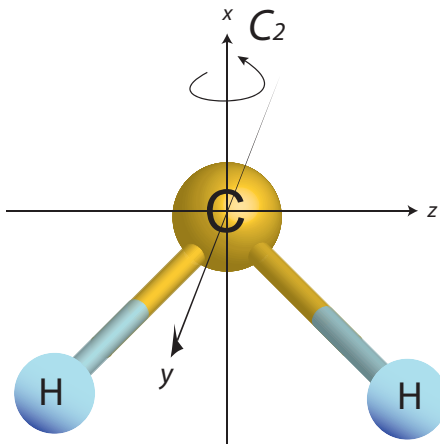
Figure 2.1: Geometry of the CH$_2$ molecule. The x axis is assumed to be the C_2 symmetry axis. The molecule lies in the xz plane.

axis, as shown in Fig. 2.1. The molecular plane (xz plane) contains the principal C_2 axis which is also a σ_v reflection plane. Both the ground state and the first excited state of CH$_2$ are bent. This geometry will be assumed by default here in this thesis, unless pointed out specifically.

Another σ_v plane (the xy plane) intersects perpendicularly the molecular plane. With one C_2 axis and two σ_v planes, bent CH$_2$ belongs to the C_{2v} point group.

For a C_{2v} molecule, all molecular orbitals correspond to the four characters: a_1, a_2, b_1 and b_2. Table 2.1 lists the symmetries of these four types with respect to the three C_{2v} symmetry operations, as well as (trivially) to the identity operator.

The $1s$, $2s$ and $2p_x$ orbitals of the carbon atom belong to a_1 symmetry (fully symmetric). The $2p_y$ and $2p_z$ orbitals, have, respectively, b_1 and b_2 character. Molecular orbitals are formed as linear combinations of the carbon orbitals with the symmetric ($1s_a + 1s_b$; a_1 symmetry) and antisymmetric ($1s_a - 1s_b$; b_2 symmetry)

Table 2.1: Character table for a C_{2v} point group

C_{2v}	E	$C_2(x)$	$\sigma_v(xz)$	$\sigma_v(xy)$
a_1	$+1$	$+1$	$+1$	$+1$
a_2	$+1$	$+1$	-1	-1
b_1	$+1$	-1	-1	$+1$
b_2	$+1$	-1	$+1$	-1

combinations of the $1s$ orbitals on the two H atoms. Thus the 5 C atomic orbitals and 2 H atomic orbitals combine to form 7 molecular orbitals, 4 of a_1 symmetry, 2 of b_2 symmetry and 1 of b_1 symmetry.

The relative energies of these molecular orbitals are shown in Fig. 2.2. At very low energy (not shown on the figure) lies the $1a_1$ orbital which is essentially the C $1s$ orbital. The second and third orbitals of a_1 symmetry are combinations of the carbon $2s$ and $2p_x$ orbitals and the positive linear combination of the $1s$ orbitals of the hydrogen. The $1b_2$ orbital, also bonding, is a combination of the $2p_z$ orbital on the C and the negative linear combination of the $1s$ orbitals of the hydrogen. The out-of-plane $2p_y$ orbital on the C forms the non-bonding $1b_1$ orbital.

As shown in Fig. 2.3, in the lowest singlet state of CH_2 all MO's up to and including the $3a_1$ orbital are doubly filled. This state is a classic example of Walsh's rules . In linear geometry, the $3a_1$ and $1b_1$ orbitals are non-bonding, corresponding, respectively, to the $2p_x$ and $2p_y$ orbitals on the C atom. As the molecule bends, the $3a_1$ orbital becomes a bonding orbital, while the $1b_1$ orbital remains non-bonding.
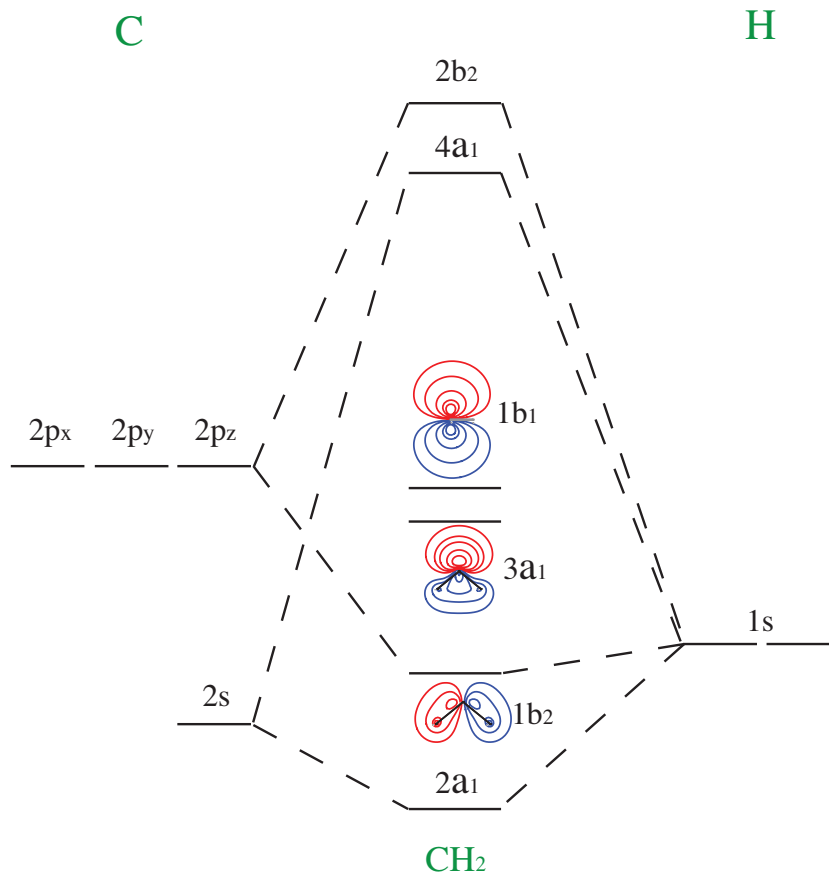
Figure 2.2: Relative energies of the molecular orbitals of H, C, and CH_2. The $1a_1$ ($1s$) orbital lies at much lower energy and is not shown. The contour plots of the $1b_2$, $3a_1$ and $1b_1$ orbitals are also shown (below or above the levels, in blue and red).

Thus, CH_2 in the $\tilde{a}$ state is strongly bent. Because all the MOs are doubly filled in this singlet state, designated $\tilde{a}$, is fully symmetric (A_1). At slightly lower energy lies the $\tilde{X}$ state. This is a triplet-coupled di-radical (multiplicity 3), in which the one electron is transferred from the $3a_1$ orbital to the $1b_1$ orbital. The overall symmetry of this state is then B_1.

Since the $3a_1$ orbital – the orbital which strongly favors bent geometry – is only singly-occupied in the $\tilde{X}\,^3B_1$ state, the bending minimum occurs at a larger HCH angle (134° for the $\tilde{X}$ state [31] compared with 102° for the $\tilde{a}$ state [32] and
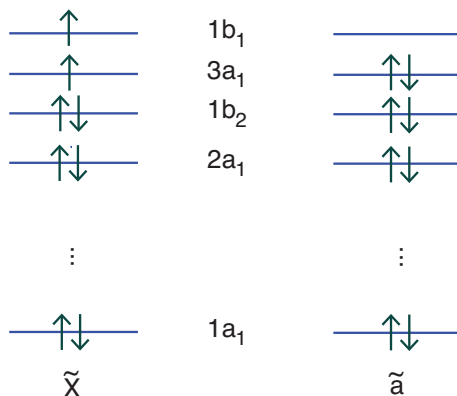
Figure 2.3: (Left Panel) Electron occupancy in the ground $\tilde{X}^3B_1$ state of CH_2 $[1a_1{}^2 2a_1{}^2 1b_2{}^2 3a_1{}^1 1b_1{}^1]$, and (Right Panel) in the the first-excited $\tilde{a}^1A_1$ state $[1a_1{}^2 2a_1{}^2 1b_2{}^2 3a_1{}^2]$.

the barrier to bending inversion is much smaller in the $\tilde{X}$ state ($\sim$1900 cm^{-1} [19] as compared to > 8000 cm^{-1} for the $\tilde{a}$ state [33]).

The marked difference in reactivity CH_2 in its two lowest electronic states can be explained by their different orbital occupancies. In the $\tilde{a}$ state, the empty $1b_1$ orbital perpendicular to the plane of the triatomic can act as an electron "acceptor" when another atom or molecule approaches perpendicular to the xz plane in Fig. 2.1, or, alternatively as an electron donor when the attacking species approaches along the x axis. Contrastingly, this Lewis acid-base amphoterism is absent in the $\tilde{X}$ state.

2.2.2 Rotational Structure: General Considerations

2.2.2.1 Rotational Motion of a Rigid Molecule

To understand the rotational motion of an asymmetric top molecule, let us first consider the rotational motions of a rigid ellipsoid. An ellipsoid centered at the

origin of a Cartesian coordinate system satisfies the equation

$$\frac{x^2}{a^2} + \frac{y^2}{b^2} + \frac{z^2}{c^2} = 1, \tag{2.1}$$

where a, b, and c are the length of its semi-principal axes along the x, y, and z axes. In treating the rotation of a non-linear molecule with non-uniform density, we will replace the semi-principal axes by the moments of inertia. [34]

In a coordinate system with origin at the center-of-mass of the molecule, the moments of inertia about the three Cartesian axes of a rigid-rotor are

$$\begin{aligned} I_{xx} &= \sum_i m_i(y_i^2 + z_i^2) \\ I_{yy} &= \sum_i m_i(x_i^2 + z_i^2) \\ I_{zz} &= \sum_i m_i(x_i^2 + y_i^2), \end{aligned} \tag{2.2}$$

while the products of inertia are

$$\begin{aligned} I_{xy} &= -\sum_i m_i x_i y_i \\ I_{yz} &= -\sum_i m_i y_i z_i \\ I_{xz} &= -\sum_i m_i x_i z_i. \end{aligned} \tag{2.3}$$

The inertia tensor is a symmetric matrix of these quantities defined as

$$
I = \begin{pmatrix} I_{xx} & I_{xy} & I_{xz} \\ I_{yx} & I_{yy} & I_{yz} \\ I_{zx} & I_{zy} & I_{zz} \end{pmatrix},
\tag{2.4}
$$

The three principal axes of inertia can be identified by diagonalizing this matrix. The eigenvalues, designated I_a, I_b, and I_c, are the new moments of inertia along the principal axes. The latter are defined by the eigenvectors. By convention, one orders these three principal moments of inertia from lowest to highest, in other words, $I_a \leq I_b \leq I_c$. The top of highest symmetry is called a spherical top. It has three equal moments of inertia $I_a = I_b = I_c$. Methane (CH_4) is an example. When two of the moments of inertia are equal, but different from the third, the molecule is called a symmetric top (NH_3 as an example). As illustrated in Fig. 2.4, there are two cases: the prolate symmetric top with $I_a < I_b = I_c$ and the oblate symmetric top with $I_a = I_b < I_c$. Finally, when all three moments of inertia differ, the molecule
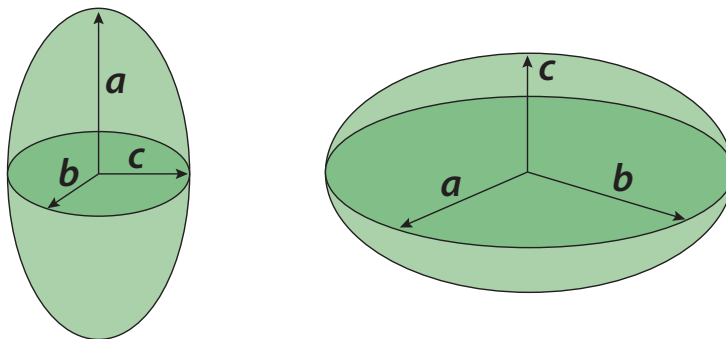
Figure 2.4: (Left Panel) Schematic rendition of a prolate symmetric top; the moments of inertia along the b and c axes are equal ($a > b = c$). (Right Panel) Similar rendition of an oblate symmetric top; the moments of inertia along the a and b axes are equal ($a = b > c$).

is called an asymmetric top. Often, an asymmetric top will be either close to the prolate limit, with $I_b \approx I_c$, or close to the oblate limit, with $I_b \approx I_a$.

The rotational Hamiltonian of a rigid rotor is [34]

$$H_r = \frac{1}{2}I_a\,\omega_a^2 + \frac{1}{2}I_b\,\omega_b^2 + \frac{1}{2}I_c\,\omega_c^2 \;, \qquad (2.5)$$

where $\omega_i(i = a, b, c)$ are angular velocities about the corresponding principal axes. We can write this rotational Hamiltonian in terms of angular momenta:

$$H_r = \frac{n_a{}^2}{2I_a} + \frac{n_b{}^2}{2I_b} + \frac{n_c{}^2}{2I_c} \;, \qquad (2.6)$$

where the angular momentum $\vec{n}_i$ is the product of the moment of inertia and the angular velocity, namely $\vec{n}_i = I_i\vec{\omega}_i$. In quantum mechanics, the expression is analogous, but involving angular momentum operators, $\hat{n}^2$, $\hat{n}_a^2$, etc.

The operator for the magnitude of the total angular momentum $\hat{n}^2$, where $\vec{n} = \vec{n}_a + \vec{n}_b + \vec{n}_c$, commutes with each of its Cartesian components, in other words $[\hat{n}^2, \hat{n}_i] = 0$. Thus, the rotational Hamiltonian $\hat{H}_r$ commutes with $\hat{n}^2 = \hat{n}_a^2 + \hat{n}_b^2 + \hat{n}_c^2$ since $[\hat{n}^2, \hat{n}_a] = [\hat{n}^2, \hat{n}_b] = [\hat{n}^2, \hat{n}_c] = 0$. However, $\hat{H}_r$ does not commute with $\hat{n}_i$ unless the other two moments of inertia are identical. For example,

$$[\hat{H}_r, \hat{n}_a] = i\hbar \left(\frac{1}{2I_c} - \frac{1}{2I_b}\right)(\hat{n}_b\hat{n}_c + \hat{n}_c\hat{n}_b). \qquad (2.7)$$

The rotational Hamiltonian will commute with $\hat{n}_a$ if and only if $I_b = I_c$. Similarly, $[\hat{H}_r, \hat{n}_b] = 0$ if and only if $I_a = I_c$ and $[\hat{H}_r, \hat{n}_c] = 0$ if and only if $I_a = I_b$.

The rotational spectrum of rigid molecular tops are constrained by these considerations. Specifically, we have

a) Spherical top

For a spherical top, $I_a = I_b = I_c = I$, so the rotational Hamiltonian is

$$\hat{H}_r = \hat{n}^2/(2I)$$

The eigenvalues (rotational energies) are then

$$E_n = \hbar^2 n(n+1)/(2I) \equiv Bn(n+1)$$

where n is the rotational quantum number and $B = \hbar^2/(2I)$ is the rotational constant. Since all the principal axis moments of inertia are the same, $\hat{H}_r$ commutes with each one, and the projection of the rotational angular momentum along any one (but only one) of the principal axes is also a good quantum number.

$$
\begin{aligned}
\hat{n}^2 \, |nk\rangle &= \hbar^2 n(n+1) \, |nk\rangle \\
\hat{n}_c \, |nk\rangle &= \hbar k \, |nk\rangle
\end{aligned}
\tag{2.8}
$$

b) Symmetric top

For a prolate symmetric top, $I_b = I_c$, so that $[\hat{H}_r, \hat{n}_a] = 0$ [Eq. (2.7)]. Since $\hat{n}_a$ commutes with the rotational Hamiltonian, its eigenvalue k_a, the projection of the rotational angular momentum on the a axis, is also a good quantum number.

14

Thus, for a prolate top

$$\hat{n}^2 \, |nk_a\rangle = \hbar^2 n(n+1) \, |nk_a\rangle$$

$$\hat{n}_a \, |nk_a\rangle = \hbar k_a \, |nk_a\rangle \tag{2.9}$$

In addition, the rotational Hamiltonian of a prolate top [Eq. (2.6)] can be rewritten as

$$\hat{H}_r = \frac{\hat{n}^2}{2I_b} + \hat{n}_a^2 \left(\frac{1}{2I_a} - \frac{1}{2I_b} \right), \tag{2.10}$$

By combining Eqs. (2.9) and (2.10) we find

$$\hat{H}_r \, |nk_a\rangle = \left[\frac{\hbar^2 n(n+1)}{2I_b} + \hbar^2 k_a^2 \left(\frac{1}{2I_a} - \frac{1}{2I_b} \right) \right] \, |nk_a\rangle. \tag{2.11}$$

Thus the rotational energies for a prolate top are given by

$$E_{r,pro}(n, k_a) = Bn(n+1) + (A - B)k_a^2, \tag{2.12}$$

where A designates the rotational constant for rotation around the a axis, namely $\hbar^2/(2I_a)$.

Entirely similarly, the rotational energies of an oblate top have energies of

$$E_{r,ob}(n, k_c) = Bn(n+1) + (C - B)k_c^2. \tag{2.13}$$

where k_c is the projection of the rotational angular momentum on the c axis,

15

$C = \hbar^2/(2I_c)$ $(A \geq B \geq C$, since $I_a \leq I_b \leq I_c)$, and $\hat{n}_c \, |nk_c\rangle = \hbar k_c \, |nk_c\rangle$.

c) Asymmetric top

In an asymmetric top none of the principal axis moments of inertia are equal. Thus, as Eq. (2.7) reveals, the projection of the angular momentum along any principal axis is not a good quantum number. There are no simple expressions for the rotational energies. These can be obtained only by diagonalizing $\hat{H}_r$ in a basis of symmetric top ($|nk\rangle$) functions. (Note, however, that the total rotational angular momentum n is still a good quantum number). Thus, the wave functions for a given n are linear combinations of the $|nk_c\rangle$ (oblate) or $|nk_a\rangle$ (prolate) functions.

The so-called Ray asymmetry parameter κ [35]

$$\kappa = \frac{2B - A - C}{A - C}. \tag{2.14}$$

is a measure of the degree of deviation from symmetric top behavior. The value of κ varies from -1 (prolate tops, $B = C$) to $+1$ (oblate tops, $A = B$). When κ is very close to $+1$ or -1, the molecule is also called a slightly symmetric top. The energies are then well predicted by the appropriate symmetric top expressions.

The rotational levels of an asymmetric top are designated as $n_{k_a k_c}$ (or $n_{k_p k_o}$), where k_a and k_c are the projection quantum numbers in the prolate and oblate limits. The CH_2 molecule in its $\tilde{a}$ and $\tilde{X}$ states is near prolate, so that the rotational wave function is most compactly expanded in terms of the prolate

16

symmetric top functions

$$|n_{k_a k_c}\rangle = \sum_{k_a} C_{k_a k_c} |n_{k_a}\rangle$$

where the coordinate-space representations of the $|n_{k_a}\rangle$ are Wigner rotation matrix elements. [36]

2.2.2.2 Spin Multiplets

For molecules with non-zero electronic spin, the spin angular momentum vector couples with $\vec{n}$ to form the total angular momentum $\vec{j}$, in other words $\vec{j} = \vec{n} + \vec{s}$. For a triplet state, $s = 1$ so that $j = n + 1, n$ and $n - 1$, which are labeled, respectively, F_1, F_2, and F_3. [37] The largest coupling is due to the dipolar interaction between the spins of the two unpaired electrons. The full Hamiltonian is then diagonalized in a set of spin-rotation prolate top functions. These are written as linear combinations of the $|nk\rangle$ and $|sk_s\rangle$ states,

$$|nsjk_j\rangle = \sum_{k_a \, k_s} (nk_a sk_s | jk_j) |nk_a\rangle |sk_s\rangle \tag{2.15}$$

where $(....|..)$ is a Clebsch-Gordan coefficient, and, for simplicity, we are assuming that the projection quantum numbers of both $\vec{s}$ and $\vec{j}$ refer to the same inertial axis system as $\vec{n}$.

Experimental work by Sears *et al.* shows that the splittings between the three spin-multiplets are on the order of only several tenths of a wavenumber (see Table

17

VIII of Ref. [37]), much smaller than the splittings between the rotational levels.

2.2.2.3   Nuclear Permutation Symmetry

As discussed in more detail in Appendix A, for a triatomic hydride HMH (where M designates a heavy atom), the total Hamiltonian is anti-symmetric with respect to interchange of the two H atoms. The spins of the two hydrogen atoms can be coupled to form either an $I = 1$ state (statistical weight of 3) which is symmetric with respect to interchange or an $I = 0$ state (statistical weight of 1) which is antisymmetric with respect to interchange. (Here, I designates the total nuclear spin).

As with the diatomic molecule H_2, the overall requirement that the system be a fermion, imposes restrictions on which rotational states of the molecule can be combined with which nuclear spin isomer ($I = 0$ or $I = 1$). The two sets of rotation-nuclear spin isomers are denoted *ortho* and *para*, with the former designating the state of larger statistical weight. Appendix A presents a more complete discussion of this topic.

2.2.3   Rotational Structure of CH_2

For a highly symmetric molecule like CH_2, there is a simple method to identify the principal axes. As depicted in Fig. 2.5, we adopt the coordinate system of Fig. 2.1, but centered at the center-of-mass. This is the coordinate system in which, later, we will expand the CH_2–He PES for our scattering calculations (see Secs. 3.2

and 4.2 for details). Because of symmetry, and the positioning of the origin, the products of inertia [Eq. (2.3)] are all zero. Thus, the three principal axes are just the CH_2 Cartesian axes shown in Fig. 2.5.
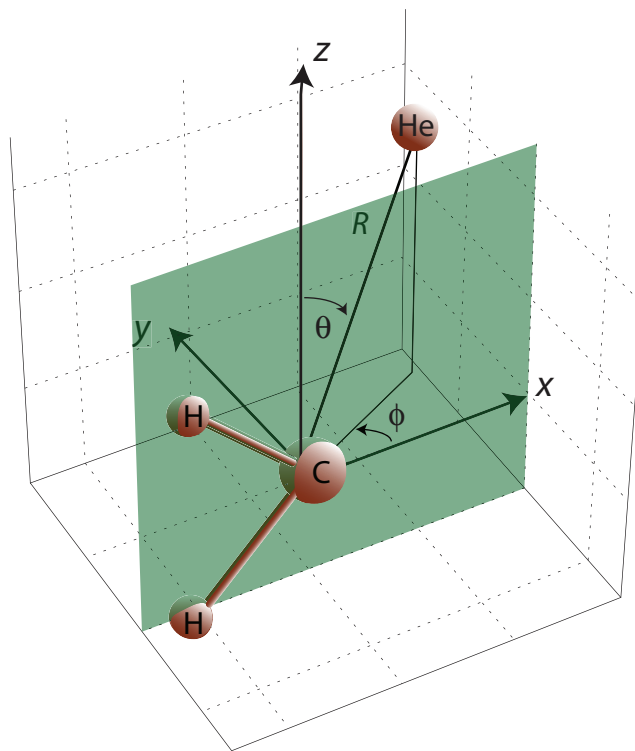
Figure 2.5: Body-frame coordinate system used to specify the orientation of the helium atom with respect to the center of mass of the CH_2 molecule. The body-frame z axis is defined to lie along the a inertial axis of the molecule. The molecule lies in the xz-plane, shown here in light green. Note that the origin is at the center of mass, which is displaced (slightly) toward negative x from the C atom.

For H_2, permutation of the two H nuclei corresponds, for the electronic degrees of freedom, to an inversion of the coordinate system. In the case of CH_2, permutation of the two H nuclei corresponds to a 180° rotation around the molecular axis. The electronic wave function for the $\tilde{a}^1A_1$ state is symmetric with respect to this operation, while that for the $\tilde{X}^3B_1$ state is antisymmetric. Thus, the attribution of which rotational levels are associated with the two ($I = 1$ and $I = 0$) nuclear spin

19

species reverses for these two states. For the $\tilde{a}$ state, rotational level $n_{k_a k_c}$ is a *para* level if and only if $k_a + k_c =$ even (or, equivalently, if k_a and k_c are both even or both odd), but is an *ortho* level when $k_a + k_c =$ odd. For the $\tilde{X}$ state, an even value of $k_a + k_c$ corresponds to an *ortho* level while an odd value of $k_a + k_c$ corresponds to a *para* level. The details of this assignment are explained in Appendix A.
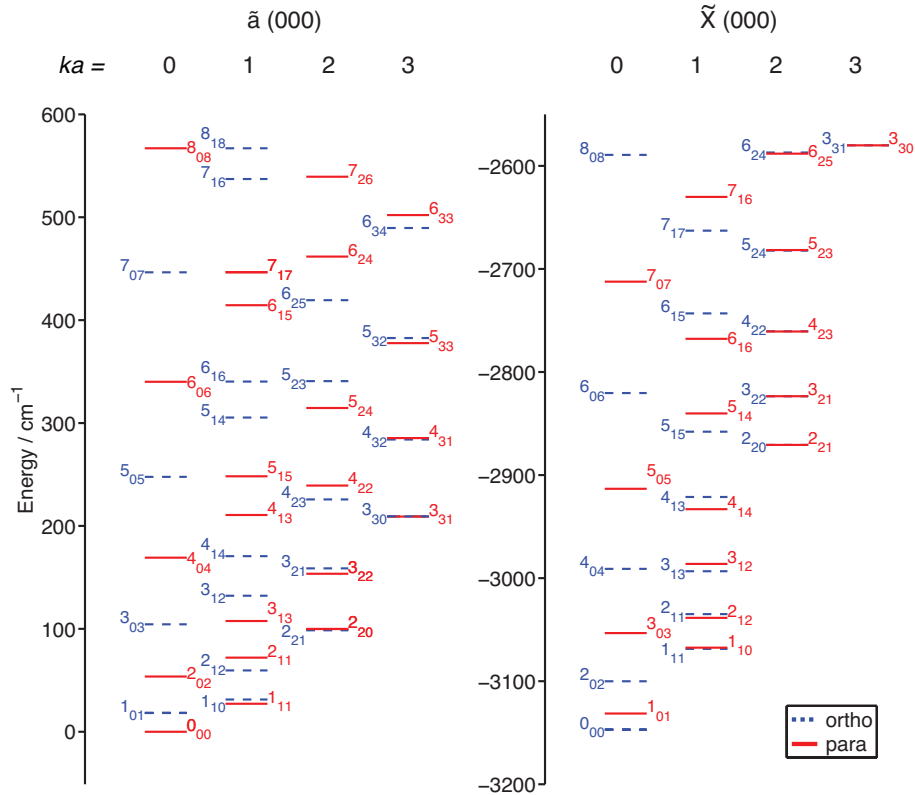
Figure 2.6: Rotational levels of *ortho* (dashed) and *para* (solid) $CH_2(\tilde{a})$ (Left Panel) and $CH_2(\tilde{X})$ (Right Panel). The rotational constants for the $\tilde{a}$ state are $A = 20.118$ cm^{-1}, $B = 11.205$ cm^{-1} and $C = 7.069$ cm^{-1}, [38, 39] while for the $\tilde{X}$ state, $A = 73.811$ cm^{-1}, $B = 8.450$ cm^{-1} and $C = 7.184$ cm^{-1}. [40] We set the energy of the lowest rotational level of the (0,0,0) origin of the $\tilde{a}$ state to zero.

We treat the CH_2 molecule in its $\tilde{a}$ state as a rigid-rotor with a C$-$H bond length of 1.11 Å and an H$-$C$-$H bending angle of 102° [32]. From Eq. (2.2), we can calculate the moments of inertia of $CH_2(\tilde{a})$ along the three moments of inertia

[Eq.(2.2)]. We find (in atomic units) $I_{xx} = 9761$, $I_{yy} = 15242$ and $I_{zz} = 5481$. As discussed earlier, for the highly symmetric CH_2 radical, the coordinate system of Fig. 2.5 does define the principal axis frame, with $a \to z$, $b \to x$, and $c \to y$.

The situation for the $\tilde{X}$ state is more complicated. The arrangement of the principal inertia axes is identical to that of the $\tilde{a}$ state, namely $a \to z$, $b \to x$, $c \to y$. But, as we discussed briefly in Chap. 1, we cannot treat $CH_2(\tilde{X})$ as a rigid molecule, due to a low barrier to linearity (more details in Chap. 5). In describing the potential energy surface for the interaction of He with $CH_2(\tilde{X})$ we have to consider the variation with respect to the HCH angle. Then, in carrying out the scattering calculations, we have to average over this degree of freedom, weighting by the square of the bending vibrational wave function.

2.2.4 Singlet-Triplet Mixing in CH_2

As stated earlier in this dissertation, the difference in electronic structures of the $\tilde{a}$ and $\tilde{X}$ states CH_2 leads to significantly different reactivities. In addition, as our work (Chaps. 4, 5 and 6) will show, rotational relaxation within the $\tilde{a}$ state is 2~3 times faster than within the $\tilde{X}$ state. [17, 18] Because the two states lie close in energy, collisional transfer between these states can be important.

Although CH_2 contains only few-electron (light) atoms, there will be a small spin-orbit coupling between the $^3\tilde{X}$ and $^1\tilde{a}$ states, on the order of a few wave numbers. [10] Appendix B of this thesis discusses the spin-orbit coupling in full detail. The spin-orbit coupling will cause significant state mixing whenever rotation-

vibration levels associated with these two electronic states lie within a few wave numbers of each other. There are two further restrictions: these nearly degenerate levels will be coupled only if they have the same total angular momentum j and only when they correspond to the same permutation symmetry.

Since CH_2 is a hydride, the rotational level distributions are sparse. Additionally, only roughly half of the levels belong to a given permutation species. Thus, the occurrence of a pair of $\tilde{X} - \tilde{a}$ levels which are significantly mixed is rare. To illustrate this, Fig. 2.7 shows a slice from of Fig. 2.6 at higher resolution in the vicinity of several nearly-degenerate $\tilde{X} - \tilde{a}$ pairs.

In developing a first-order model for collision-induced transitions between the vibration-rotation manifolds of the two electronic states, one need consider only couplings arising from these rare pairs of mixed levels. A kinetic model based on this approximation was first developed by Freed and co-workers. [41–43] Because of the availability of spectroscopic and kinetics data on the methylene radical (as summarized in references [44] and [9]), CH_2 is an ideal species to assess the accuracy of the mixed-state model of Gelbart and Freed. [10, 12, 15].

In this model, intersystem crossings occur only through a few pairs of "gateway" (or mixed) levels. These have partial singlet and partial triplet character. For notational simplicity, let the rovibronic (rotational-vibrational-electronic) state of the $\tilde{X}$ and $\tilde{a}$ components of a mixed pair be

$$|\psi_s\rangle = |\chi_v^s j k_a^s k_c^s\rangle|^1A_1\rangle \tag{2.16}$$
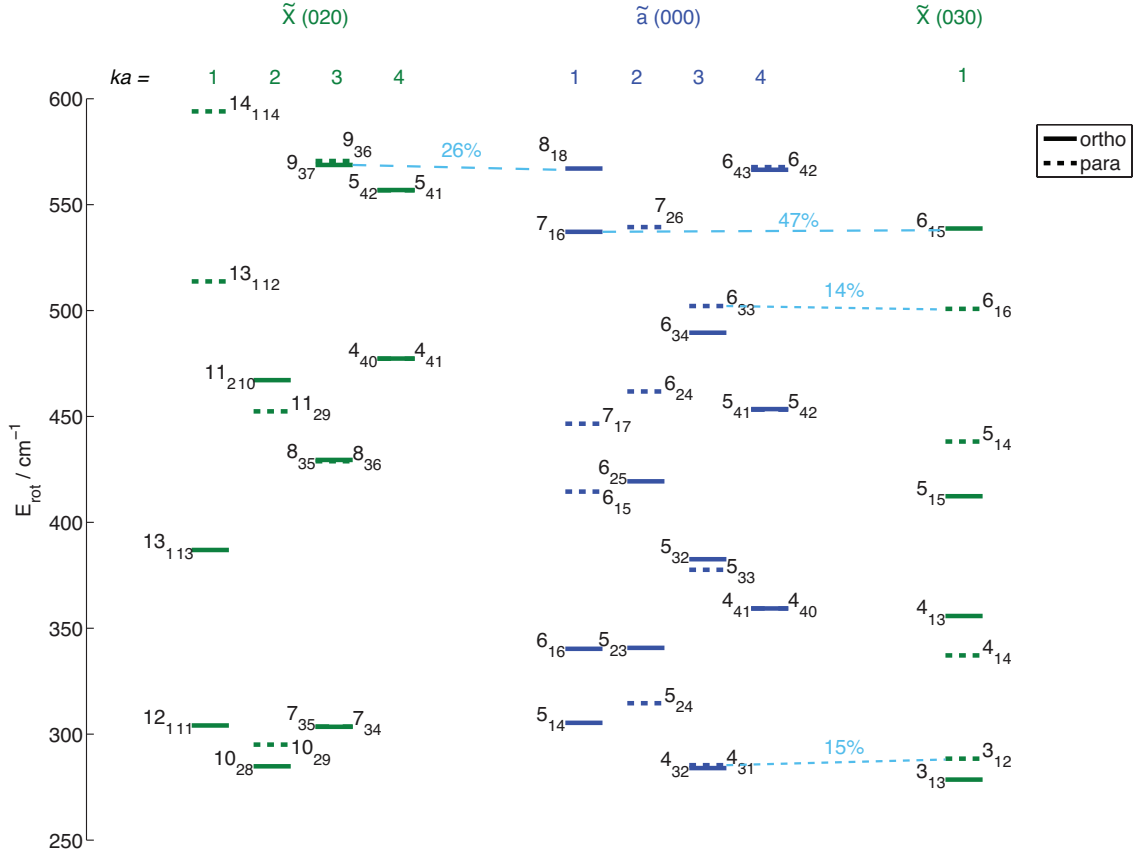
Figure 2.7: Energy diagram of the four low-lying strongly-mixed "gateway" pairs in the energy range of 250–600 cm^{-1}, measured relative to the lowest rotational level of the (0,0,0) origin of the $\tilde{a}$ state. This figure is a slice of Fig. 2.6 over a smaller range of energy. The percentage mixing determined by Bley and Temps [10] are shown in light blue. This is the square (multiplied by 100) of the sine of the mixing angle defined below in Eq. (2.20). Note that we have ignored the spin of the $\tilde{X}$ state, labeling the levels in this state by the rotational quantum number n and its projections. In reality, each of these levels will be a triplet with $j = n + 1, n$ and $n - 1$. Only one of these will have a value of j identical to that of the nearly-degenerate level in the $\tilde{a}$ state level (where $j = n$). Shown are levels from the (0,2,0) and (0,3,0) bending manifolds of the $\tilde{X}$ state and from the vibrational ground state (0,0,0) of the $\tilde{a}$ state. In the energy range shown, the pair with the most complete mixing (nearly 50:50) is the $6_{15}(j = 7)$ level of the (0,3,0) vibrational manifold of the $\tilde{X}$ state and the 7_{16} level of the $\tilde{a}$ state.

and

$$|\psi_t\rangle = |\chi_v^t j n^t k_a^t k_c^t\rangle|^3 B_1\rangle \tag{2.17}$$

Here, we have introduced the eponymous indices t and s for the triplet and sin-

glet states, and have subsumed the three vibrational quantum numbers (symmetric stretch, antisymmetric stretch, bend) into a single index. In Eqs. (2.16) and (2.17) we have explicitly appended the electronic wave functions of the two states. Note that although the total angular momentum j has to be the same for the two levels, in the $\tilde{X}$ state the rotational quantum number n can be different, since three spin-multiplets occur for all values of $n \geq 1$, namely $j = n$ and $n \pm 1$.

The matrix element of the spin-orbit Hamiltonian, $\hat{H}_{so}$ is

$$H_{st} = \langle \psi_s | \hat{H}_{so} | \psi_t \rangle = \langle \chi_v^s | \langle j k_a{}^s k_c{}^s | \langle {}^1A_1 | \hat{H}_{so} | {}^3B_1 \rangle | j n^t k_a{}^t k_c{}^t \rangle | \chi_v^t \rangle$$

Here, $\langle {}^1A_1 | \hat{H}_{so} | {}^3B_1 \rangle$ is the electronic spin-orbit matrix element (see Appendix B), which is a function of the nuclear coordinates. This is then integrated over the product of the two rotational wave functions, and, ultimately, over the product of the vibrational wave functions. If we assume that the electronic matrix element is a constant, then the integral over the product of rotational wave functions is a double sum of integrals of products of rotation matrix elements. Finally, the integral over the vibrational wave functions constitutes a multidimensional Franck-Condon factor.

The mixing between states $|\psi_s\rangle$ and $|\psi_t\rangle$ is obtained by diagonalizing the 2×2 matrix

$$\mathbf{H} = \begin{bmatrix} E_s & H_{st} \\ H_{st} & E_t \end{bmatrix}$$

where E_s and E_t are the energies of the singlet and triplet states, defined by

Eqs. (2.16) and (2.17). In terms of the pure singlet and triplet states, the wave functions for the mixed states can be written as

$$|\psi_A\rangle = -\cos\theta\,|\psi_s\rangle + \sin\theta\,|\psi_t\rangle,\qquad(2.18)$$

and

$$|\psi_X\rangle = \sin\theta\,|\psi_s\rangle + \cos\theta\,|\psi_t\rangle.\qquad(2.19)$$

where θ, the so-called "mixing angle", is

$$\theta = \frac{1}{2}\tan^{-1}\left(\frac{2H_{st}}{E_t - E_s}\right)\qquad(2.20)$$

The fractional mixing, is measured by the magnitude of $\sin^2\theta$, can rise as high as 50% (0.5) when the nominal singlet and nominal triplet levels are degenerate.

Bley and Temps [10] conducted a meticulous determination of the degree of $\tilde{X} - \tilde{a}$ mixing in CH_2 for over 100 rotational levels of the ground vibrational level of the $\tilde{a}$ state in rotational levels up to and including $n = 10$ and $k_a = 6$. They found (Table 5 of [10]) that only 16 pairs have fractional mixings larger than 0.01, and, of these only 5 pairs have fractional mixing larger than 0.1 (Table 2.2). In our study, we focus on the first four pairs listed in the table. The $9_{45}[\tilde{a}]$ and $9_{46}[\tilde{X}(020)]$ pair have both high energy and large k_a. They are consequently difficult to investigate both experimentally and theoretically.

Outside of the four pairs of "mixed" or "perturbed" states, we shall assume that all other rotation-vibration levels are unmixed by the spin-orbit coupling. As

Table 2.2: Energies and mixing coefficients (from [10]) of the most strongly mixed pairs in Fig. 2.7. All $\tilde{a}$ state levels are in the vibrational ground state (0,0,0). The zero of energy is the lowest rotational level of this manifold.

| o/p | $\tilde{a}$ | $\tilde{X}$ | | $E_s(\text{cm}^{-1})$ | $E_t(\text{cm}^{-1})$ | $\sin^2\theta$ |
		$(v_1 v_2 v_3)$	$j, n_{k_a k_c}$			
$para$	4_{31}	(0,3,0)	$4, 3_{12}$	285.366	287.376	0.149
$para$	6_{33}	(0,3,0)	$6, 6_{16}$	502.132	501.302	0.138
$ortho$	7_{16}	(0,3,0)	$7, 6_{15}$	537.160	537.560	0.463
$ortho$	8_{18}	(0,2,0)	$8, 9_{37}$	567.028	568.728	0.256
$ortho$	9_{45}	(0,2,0)	$9, 9_{46}$	1042.44	1031.40	0.240

will be discussed below in Sec. 3.2 [see Eq. (3.25)], in the absence of spin-orbit coupling we determine the cross sections for transitions between any two levels, in, separately, either the $\tilde{X}$ or $\tilde{a}$ state, by fully quantum scattering calculations. For this, we use the HIBRIDON code. [45]

Formally, the amplitude between an initial $|i\rangle$ and a final $|f\rangle$ state can be written as

$$\langle i|\hat{T}|f\rangle \equiv T_{if} \tag{2.21}$$

where $\hat{T}$ denotes a generalized transition operator. In the mixed state model, the T matrix is computed, separately, for the unmixed $\tilde{X}$ and $\tilde{a}$ levels. Then, Eq. (2.21) is extended, to take into the mixed character of the pair. This will allow collision-induced coupling between the two mixed levels in the vibrational manifolds of both electronic states.

In the simplest approximation, we will treat each pair of mixed levels separately. The wavefunctions of the mixed pair are given by Eq. (2.18) and (2.19). The transition amplitudes involving transitions to/from one or the other of the pair of mixed states from/to any unmixed level will be straightforward linear combinations of the T-matrix elements between the unmixed states.

For example, from the mixed level with nominal $\tilde{a}$ character, whose wave function is given by Eq. (2.18), into an unmixed level in the singlet $\tilde{a}$ state, which we designate $|s'\rangle$, we have

$$
\begin{aligned}
T_{As'} &= \langle\psi_A|\hat{T}|\psi_{s'}\rangle \\
&= (-\cos\theta\,\langle\psi_s| + \sin\theta\,\langle\psi_t|)\hat{T}|\psi_{s'}\rangle = -\cos\theta\,\langle\psi_s|\hat{T}|\psi_{s'}\rangle + \sin\theta\,\langle\psi_t|\hat{T}|\psi_{s'}\rangle \\
&= -\cos\theta\,T_{ss'}. \tag{2.22}
\end{aligned}
$$

The cancellation of the $\langle\psi_t|\hat{T}|\psi_{s'}\rangle$ term in going from the 2nd to the 3rd line occurs because we assume no coupling between the singlet and triplet rovibronic manifolds in the absence of spin-orbit mixing. In other words, in the mixed-state model, the weak spin-orbit coupling in the isolated CH_2 molecules allows for a mixing of the nearly-degenerate pairs. Outside of this mixing, we ignore any direct spin-orbit coupling during the course of the collision.

Similarly, from the mixed level with nominal $\tilde{X}$ character, whose wave function is given by Eq. (2.19), into an unmixed level in the singlet $\tilde{a}$ state, which we designate $|s'\rangle$, we have

$$
T_{Xs'} = \sin\theta\,T_{ss'} \tag{2.23}
$$

Also, for transitions from the mixed pair into unmixed levels in the triplet $\tilde{X}$ state, we have

$$T_{Xt'} = \cos\theta \; T_{tt'} \tag{2.24}$$

and

$$T_{At'} = \sin\theta \; T_{tt'} \tag{2.25}$$

The T-matrix elements for transitions between the pair of gateway states are more complicated. There are two terms in both Eq. (2.18) and (2.19). This gives rise to four possible mixed T-matrix elements. Of these, two vanish because of the absence of coupling between the unmixed ro-vibronic levels of the two states. We then find, taking as an example the state of nominal $\tilde{a}$ character,

$$
\begin{aligned}
T_{AA} &= \langle \psi_a | \hat{T} | \psi_a \rangle \\
&= (-\cos\theta \, \langle \psi_s | + \sin\theta \, \langle \psi_t |) \hat{T} (-\cos\theta \, |\psi_s\rangle + \sin\theta \, |\psi_t\rangle) \\
&= \cos^2\theta \, \langle \psi_s | \hat{T} | \psi_s \rangle + \sin^2\theta \, \langle \psi_t | \hat{T} | \psi_t \rangle = \cos^2\theta \, T_{ss} + \sin^2\theta \, T_{tt}. \quad (2.26)
\end{aligned}
$$

For the three other possible couplings (XX, AX and XA) we find

$$T_{XX} = \sin^2\theta \; T_{ss} + \cos^2\theta \; T_{tt} \tag{2.27}$$

and

$$T_{XA} = T_{AX} = \cos\theta \sin\theta \, (-T_{ss} + T_{tt}) \tag{2.28}$$

We note, in passing, that the T-matrix elements between the two different com-

ponents of a mixed pair are linear combinations of the elastic T_{ss} and T_{tt} matrix elements, which can be expected to be both large in magnitude, but certainly not identical. Thus, the T-matrix elements connecting the two mixed states "borrow" from the T-matrix elements for elastic transitions, which are large. Thus we anticipate that the collisional transfer between the components of a mixed pair will be efficient.

2.3 Previous Experimental Studies of Collisions of CH_2 with Noble Gases

The group of Hall and Sears at the Brookhaven National Laboratory have investigated experimentally the role of mixed states in the kinetics of the thermalization CH_2 with both Ar and He as the collision partner. [12,14,46] Photodissociation of ketene at 308 nm produces singlet CH_2 in nearly unit yield. [47] The nascent CH_2 molecules are translationally hot, with a rotational rotational distribution that can be well described as a Boltzmann distribution at 700–800 K.

Hall and Sears measured the time dependence of the populations of selected *ortho*- and *para*-$CH_2(\tilde{a})$ levels. As the molecules cool to a room temperature Boltzmann distribution, the population of each individual CH_2 rotational level exhibited a double exponentially decay. Hall and Sears discovered that initially the rotational levels with higher energies depleted faster than those with lower energies. In fact, the latter showed initial *increases* in populations, followed by slow depletion at longer times. Eventually all levels decayed at the same rate.

Hall and Sears also reported that the decays of the 8_{18} level of the $\tilde{a}$ and the $9_{37}(020)$ level of the $\tilde{X}$ state quickly exhibited identical time dependence. These two levels constitute one of the mixed pairs listed in Table 2.2. The 7_{16} and 6_{15} pair in this table is nearly completely mixed. As a consequence, it was difficult to distinguish experimentally the relaxation of the the two components. The other two pairs in Tab.2.2 have low fractional mixings ($\sim 15\%$). This is too small to allow as clean an analysis as was possible for the 8_{18}–9_{37} pair. Hall and Sears concluded that to explain their results, collisional interconversion of the two levels of this mixed pair needed to be at least ten times more efficient than rotational inelastic collisions between other levels. Accordingly, in Chap. 6 below, we shall focus on the 8_{18}–9_{37} pair.

Subsequent to relaxation to a room-temperature distribution, Hall and Sears investigated the saturation recovery of *ortho*-CH_2. These experiments involve bleaching a single rotational level and monitoring the return of the population in that level. This is kinetically equivalent to watching the total removal rate in an experiment in which only the initial rotational level is populated. [48] They carried out saturation recovery experiments for bleaching of both components of the 8_{18}–9_{37} pair as well as for some other $k_a = 1$ rotational levels of the ground vibrational level of the $\tilde{a}$ state. [14] As predicted, the most efficient saturation recovery occurs when one of a pair of mixed-pair levels is initially depleted. Subsequent equilibration of the population of the mixed-pair is then very fast. The collisional recovery of bleached unmixed levels is much slower.

In another recent study on CH_2, Gannon, Seakins and co-workers investigated

experimentally some predictions of the gateway model and estimated the accuracy of the mixed state model. [15]. Among the five strongest mixed pairs predicted by Bley and Temps, and listed in Table 2.2, the two pairs for the *para* nuclear spin species occur at lower energy than the remaining three pairs, which correspond to rotational levels of o-CH_2. Thus, at low temperature, where the lower rotational populations are preferentially populated, one would expect gateway-induced relaxation of p-CH_2 to be faster than that of o-CH_2. As the temperature increases, we might expect this preference to decrease. Gannon *et al.* observed a *para* vs. *ortho* preference for $195 \leqslant T \leqslant 298$ K, but not at higher temperatures. They conjectured that other mixed pairs, accessible only at high temperature, might not yet have been identified.

Gannon and Seakins also analyzed the dependence of the *para/ortho* removal rate on the size of collider. In the gateway model the spin-orbit coupling between the nearly-degenerate pairs of $\tilde{a}$ and $\tilde{X}$ rotational levels is assumed unchanged during the collision. Thus, to a first approximation, one might expect the efficiency of the gateway to be independent of the collision partner, at least for the noble gasses. In contrast, experimentally they detected significant changes in the ratio of the *para/ortho* removal rates with various noble gas colliders at low temperature. They suggested that since the collision will cause transient changes in the energy separations of the CH_2 rotational states, the mixing between the nearly-degenerate pairs will vary during the course of the collision, and not necessarily remain fixed at its asymptotic value.

We might argue, in response, that the effect of the mixing is most manifest in the intra-pair couplings, in which differences in the elastic T-matrix elements

intervene [see Eqs. (2.26)-(2.28)]. The elastic scattering of CH_2 will be quite dependent on the collision partner, especially the phases of the elastic T-matrix elements. Thus, we would not necessarily anticipate a lack of dependence on the identity of the collision partner.

Gannon and Seakins concluded that their observations strongly supported the gateway model, but suggested that some small modifications to the model might be necessary.

Chapter 3: Theoretical Methods

3.1 Potential Energy Surfaces and *ab initio* Calculations

To investigate the collision-induced relaxation of CH_2 we solve the time-independent Schrödinger equation

$$\hat{H}\Psi(\mathbf{Q}, \mathbf{q}) = \mathcal{E}\Psi(\mathbf{Q}, \mathbf{q}), \tag{3.1}$$

for the $He-CH_2$ system, where $\mathcal{E}$ is the total energy. Here, $\mathbf{Q}$ and $\mathbf{q}$ denote the coordinates of, respectively, the nuclei and the electrons. Under the assumption that all nuclei and electrons are point masses, the Hamiltonian [49] of a polyatomic system is

$$\begin{aligned}
\hat{H}(\mathbf{Q}, \mathbf{q}) =& \hat{T}_N(\mathbf{Q}) + \hat{T}_e(\mathbf{q}) + \hat{V}_{NN}(\mathbf{Q}) + \hat{V}_{eN}(\mathbf{Q}, \mathbf{q}) + \hat{V}_{ee}(\mathbf{q}) + \hat{H}_{so} \\
=& -\frac{\hbar^2}{2}\sum_\alpha \frac{1}{m_\alpha}\nabla_\alpha^2 - \frac{\hbar^2}{2m_e}\sum_i \nabla_i^2 + \sum_\alpha \sum_{\beta>\alpha} \frac{Z_\alpha Z_\beta e^2}{r_{\alpha\beta}} \\
& -\sum_\alpha \sum_i \frac{Z_\alpha e^2}{r_{i\alpha}} + \sum_j \sum_{i>j} \frac{e^2}{r_{ij}} + \hat{H}_{so}
\end{aligned} \tag{3.2}$$

The indices α, β refer to the nuclei, while the indices i, j refer to the electrons. The first five terms are, respectively, the operators for the kinetic energy of the nuclei ($\hat{T}_N$), of the electrons ($\hat{T}_e$), the operator for the repulsive nuclear-nuclear interaction

(V_{NN}), the attractive electron-nuclear interaction (V_{eN}), and the repulsive electron-electron interaction (V_{ee}). For the time being we ignore the spin-orbit coupling $\hat{H}_{so}$. Our goal is to simplify the equation and eventually find the approximate solutions of this Schrödinger equation.

Due to the presence of the electron-nuclear interaction V_{eN} term, the electronic and nuclear motions of the system are not separable. To accomplish this separation, and thereby simplify the problem, we introduce the Born-Oppenheimer approximation. [50] Under the Born-Oppenheimer approximation, we can separate the electronic motion of the system, obtaining the electronic Schrödinger equation:

$$\hat{H}_e(\mathbf{Q}, \mathbf{q})\Phi_e^{(k)}(\mathbf{Q}, \mathbf{q}) = E_e^{(k)}(\mathbf{Q})\Phi_e^{(k)}(\mathbf{Q}, \mathbf{q}), \qquad (3.3)$$

where the electronic Hamiltonian is defined as

$$\hat{H}_e(\mathbf{Q}, \mathbf{q}) = \hat{T}_e(\mathbf{q}) + \hat{V}_{eN}(\mathbf{Q}, \mathbf{q}) + \hat{V}_{ee}(\mathbf{q}), \qquad (3.4)$$

In Eq. (3.3) the superscript index k designates a particular electronic state (in our case $k = 1$ or 2 designates, respectively, the ${}^3\tilde{X}$ or ${}^1\tilde{a}$ states of CH_2). The electronic wavefunction $\Phi_e^{(k)}$ is a function of the electronic coordinates but depends also on the position of the nuclei $\mathbf{Q}$. The total wave function of Eq. (3.1) is

$$\Psi^{(k)}(\mathbf{Q}, \mathbf{q}) = \Phi_e^{(k)}(\mathbf{Q}, \mathbf{q})\Phi_N^{(k)}(\mathbf{Q}). \qquad (3.5)$$

In our research, at each set of nuclear coordinates $\mathbf{Q}$, we carry out *ab initio*

calculations for the electronic wave functions $\Phi_e^{(k)}(\mathbf{Q}, \mathbf{q})$ and the electronic energies $E_e^{(k)}(\mathbf{Q})$. By performing *ab initio* calculations at various $\mathbf{Q}$, we obtain the electronic energy of state k as a function of the positions of the nuclei. This defines the potential energy (or potential energy surface, PES) which subsequently governs the motion of the nuclei. For these *ab initio* calculations we used the MOLPRO program suite [51], versions 2009.1 and 2010.1.

The PES is the sum of the electronic energy as a function of relative positions of the nuclei as well as the repulsion between the nuclei themselves. For a diatomic system, besides the three coordinates used to locate the position of the center of mass and two angles to specify the orientation of the bond axis, a final distance R is needed to specify the distance between the two nuclei. The potential of a diatomic system is only a function of this latter, as shown in Fig. 3.1.
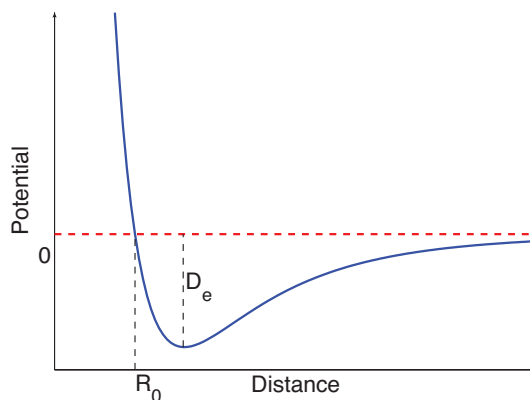
Figure 3.1: Schematic plot of the dependence of the potential energy potential on the atom-atom distance for a diatomic system. R_0 is the extent of the repulsive interaction and D_e is the depth of the potential.

In general, $3M$ coordinates are necessary to characterize the location of the nuclei in a nonlinear $M-$atom system, of which three coordinates define the location

35

of the overall center of mass, and another three specify the orientation of the system. Consequently there are $3M - 6$ internal degrees of freedom. The complexity of the *ab initio* calculation and the extent of the PES will increase swiftly with the increase of the size of the molecules. In the case of He–CH$_2$, if the two C−H bond lengths and the H−C−H bending angle are fixed, the relative position of the He atom with respect to the center-of-mass of the CH$_2$ can be described by three spherical polar coordinates R, θ and ϕ.[Fig. (3.2)] For a grid of R, θ and ϕ values, we perform *ab initio* calculations and obtain the accurate potential energy surfaces for interaction of He with the first excited ($\tilde{a}$) state of CH$_2$. In the case of the ground ($\tilde{X}$) state, we allow the bending angle to vary, in which case the grid of coordinates is extended to include this degree of freedom.
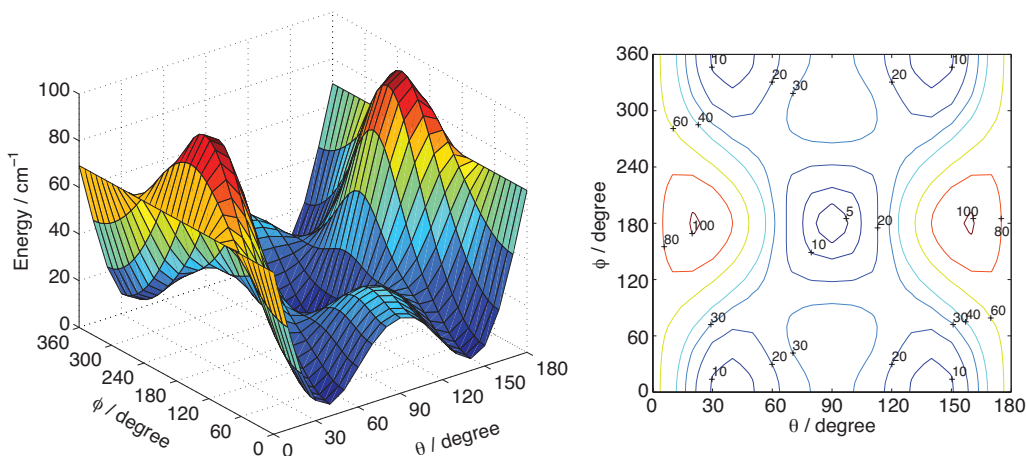
Figure 3.2: (Left Panel) Demonstrative plot of the CH$_2(\tilde{X})$−He potential energy as a function of spherical coordinates θ and ϕ, at a separation distance of R(CH$_2$,He) = 6.0 bohr. (Right Panel) The corresponding contour plot. The PES was calculated by averaging the bending-dependent PESs over the bending probability (see details in Chapter 5).

All our *ab initio* calculations were carried out with the CCSD(T) method [52, 53], a simplified coupled-cluster(CC) expansion of the electronic wave function. In

the configuration-interaction (CI) approach, the electronic wave function of a system is represented by a full set linear combination of products of single-particle functions (or molecular orbitals). If $|\Phi_e^{(0)}\rangle$ designates the dominant electron configuration, then the wave function can be written, formally, as a linear combination of $|\Phi_e^{(0)}\rangle$, along with all single, double, triple, up to N-electron excitations (where $N = 10$ for the CH_2He system), namely (for any chosen electronic state) [54]

$$\Phi_e = \Phi_e^{(0)} + \sum_{S_i} |\Phi_e^{(1)}\rangle + \sum_{D_i} |\Phi_e^{(2)}\rangle + \sum_{T_i} |\Phi_e^{(3)}\rangle + \dots, \qquad (3.6)$$

Here, S, D and T denote, respectively, single, double and triple excitations. In the CCSD(T) method, the single- and double-excitation corrections are determined with an exponential cluster operator while the triple-excitation contribution is determined perturbatively. [52]

The relative (or interaction) energy between CH_2 and He is computed as the difference between the energy of the complex (CH_2-He) and the energy of the separate CH_2 and He fragments [55, 56]

$$V_{CH_2He}(\mathbf{Q}) = E_{CH_2He}(\mathbf{Q}) - E_{CH_2} - E_{He}. \qquad (3.7)$$

If only a finite atomic orbital basis is used to construct the molecular orbitals, then the description of the CH_2 and He components in the CH_2–He might be better than in the separated fragments (for example, the presence of the CH_2 atomic orbitals provides, in principle, a more complete basis for the He wave function than a similar

calculation of just the He fragment). This Basis Set Superposition Error (BSSE) can be eliminated by subtracting from the energy of CH_2–He at a given geometry the energy of the separated He and CH_2, computed at the same geometry with the full (called supermolecular) atomic orbital basis, namely [57]

$$V_{CH_2He}(\mathbf{Q}) = E_{CH_2He}(\mathbf{Q}) - E_{CH_2\overline{He}}(\mathbf{Q}) - E_{\overline{CH_2}He}(\mathbf{Q}). \qquad (3.8)$$

Here the overline indicates that the calculation is done with the full atomic orbital basis but without the presence of the nuclei of the overlined moiety. Note that this equation applies to CH_2 in either electronic state, so that, in complete generality, we should refer to the potential energy surface as $V_{CH_2He}^{(k)}(\mathbf{Q})$. We chose the zero of energy so that this potential vanishes as the CH_2 – He distance goes to infinity.

In our calculations we use the standard augmented correlation consistent polarized quadruple zeta (aug-cc-pVQZ) atomic orbital basis function sets. [58]. We also add a set of additional atomic orbitals (without any accompanying nuclear charges) centered at the midpoint of $\vec{R}$, which joins the center of mass of CH_2 with He. Addition of these "mid-bond functions" has been found to improve accuracy in the calculation of weak non-bonded interactions. [59, 60]

3.2 Time-Independent Scattering Calculations

Once we have solved the electronic Schrodinger equation [Eq. (3.3)], we proceed to solve Eq. (3.5) for the nuclear wavefunction, namely

$$\left[\hat{T}_N(\mathbf{Q}) + E_e^{(k)}(\mathbf{Q}) + V_{NN}(\mathbf{Q}) \right] \Phi_N^{(k)}(\mathbf{Q}) = \left[\hat{T}_N(\mathbf{Q}) + V_N^{(k)}(\mathbf{Q}) \right] \Phi_N^{(k)}(\mathbf{Q}) = \mathcal{E}\Phi_N^{(k)}(\mathbf{Q})$$

(3.9)

where $E_e^{(k)}$ is the CH$_2$–He electronic energy when CH$_2$ is in electronic state k. The nuclear repulsion does not, of course, depend on the electronic state of the molecule. Equation (3.9) also introduces the potential energy surface, $V_N^{(k)}(\mathbf{Q})$, which governs the motion of the nuclei. This PES is the sum of the electronic energy in state k, $E_e^{(k)}(\mathbf{Q})$), and the nuclear repulsion, $V_{NN}(\mathbf{Q})$.

In reality, we carry out separate calculations for scattering of CH$_2$ in each electronic state. As outlined in Sec. 2.2.4, we allow for electronic state mixing, by a transformation of the T matrix elements for the pure-state scattering. Thus, for notational simplicity, from here on we will drop the electronic state index k, except where explicitly needed.

The solutions to Eq. (3.9) correspond to the unbound (scattering) motion of the He atom relative to the CH$_2$ molecule. To obtain these we use a "close-coupling" (CC) method, [61] which entails expanding in a set of functions which span all nuclear coordinates, except for the separation coordinate R between the centers-of-mass of He and CH$_2$. This results in converting the partial differential equation (3.9) to a set of coupled ordinary differential equations – hence the term "close-coupling".

Let us represent all the nuclear coordinates save R as $\mathbf{s} \equiv \{\theta, \phi, \Omega, r_v\}$. Here θ and ϕ are the orientation of $\vec{R}$, Ω is the orientation of the CH$_2$ molecule with

respect to its principal axis, and r_v designates, collectively, the three vibrational coordinates of CH_2. We shall designate by $\xi_m(\mathbf{s})$ the complete set of functions that span the internal space of the He–CH_2 system which we will use in the expansion. These are orthogonal and assumed normalized with respect to integration over $\mathbf{s}$.

The CC expansion is

$$\Phi(R, \mathbf{s}) = \sum_m \frac{C_m(R)}{R} \xi_m(\mathbf{s}),$$ (3.10)

Substitution of Eq. (3.10) into Eq. (3.9), premultiplication by an arbitrary one of the complete set, $\xi_{m'}$ say, and integration over the internal space, gives

$$\int \xi_{m'}^*(\mathbf{s}) \left[\hat{T}_N(R, \mathbf{s}) + \hat{V}_N(R, \mathbf{s}) \right] \xi_m(\mathbf{s}) d\mathbf{s} = \mathcal{E} \int \xi_{m'}^*(\mathbf{s}) \xi_m(\mathbf{s}) d\mathbf{s}$$ (3.11)

The kinetic energy operator is (in atomic units, where $\hbar = 1$)

$$\hat{T}(R, \mathbf{s}) = -\frac{1}{2\mu R^2} \left[\frac{\partial}{\partial R} \left(R \frac{\partial}{\partial R} \right) + \hat{l}^2 \right] + \hat{H}_{CH_2}(\mathbf{r}_v)$$ (3.12)

Here $\hat{l}$ is the operator for the orbital angular momentum of the He around the CH_2, with

$$\vec{l} \equiv \vec{J} - \vec{n}$$ (3.13)

and $\vec{J}$ and $\vec{n}$ being the total angular momentum and the angular momentum of the CH_2 molecule. Here, we will follow Sec. 2.2.2 in using n to denote the rotational angular momentum of the CH_2 in the absence of electronic spin. Note, that we will

ignore, unless explicitly stated otherwise – in particular in Chap. 6 – the spin of CH_2 in the $\tilde{X}$ state.

Finally, $\hat{H}_{CH_2}$ is the Hamiltonian for the vibration-rotation motion of the CH_2 molecule (see Sec. 2.2.2). Notably,

$$\hat{H}_{CH_2}|nk\rangle|v\rangle = \varepsilon_{nkv}|nk\rangle|v\rangle$$

where ε_n is the energy of the nkv^{th} vibration-rotation state of CH_2 (remember that v is a composite index).

The coordinate space representation of the rotational motion of the CH_2 molecule in the state $|nk\rangle$ is proportional to a rotation matrix element $D_{m_nk}^{n}{}^*(\Omega)$. [36] Here k is the projection of $\vec{n}$ about the principal axis, m_n is the projection of $\vec{n}$ about an (arbitrary) external z axis, centered on the center-of-mass of the CH_2, and Ω is the orientation of the CH_2 principal axis with respect to this external coordinate frame. In this external coordinate frame, the rotational motion of He around CH_2 can be described completely by an expansion in spherical harmonics $Y_{l,m_l}(\theta, \phi)$, where the angles again refer to the external (or space-fixed) axis system centered on the center-of-mass of the CH_2 molecule. Here, the quantum number l corresponds to the angular momentum defined in Eq. (3.13).

It is convenient to couple the vectors $\vec{n}$ and $\vec{l}$ to form the total angular momentum $\vec{J}$ [see Eq. (3.13)]. The coupled states are standard transformations of the

41

uncoupled product states $|nkm_n\rangle|lm_l\rangle$, namely

$$
\begin{aligned}
|nklJM\rangle &= \sum_{m_n,m_l} (nm_n lm_l|JM)|lm_l\rangle|nm_nk\rangle \\
&= \sum_{m_n m_l} (nm_n lm_l|JM)Y_{lm_l}(\theta,\phi)D^n_{m_n k}{}^*(\Omega)
\end{aligned}
\qquad (3.14)
$$

where $(\cdots|\cdot\cdot)$ is a Clebsch-Gordan coefficient. In this set of coupled states both n, the rotational angular momentum of the CH_2, and l, the orbital angular momentum of the He–CH_2 pair, are good quantum numbers, along with the total angular momentum J and its space-fixed projection M.

In terms of this coupled, space-frame basis, the wave function is expanded as

$$
\Phi^{(k)}(\mathbf{Q}) = \sum_{nklJM}\sum_{\mathrm{v}} \frac{C_{\mathrm{v}nklJM}(R)}{R}|\mathrm{v}\rangle|nklJM\rangle,
\qquad (3.15)
$$

In the absence of external fields, both the total angular momentum and its projection are conserved, so that the wave function and the expansion coefficients can be indexed in J and M. These indices can be removed from the summation. We have

$$
\Phi^{(JM)}(\mathbf{Q}) = \sum_{\mathrm{v}nkl} \frac{C^{JM}_{\mathrm{v}nkl}(R)}{R}|\mathrm{v}\rangle|nklJM\rangle,
\qquad (3.16)
$$

We then insert this expansion into Eq. (3.9), premultiply by one of the internal functions $\langle n'k'l'J'M'|\langle \mathrm{v}'|$, and integrate over all the internal coordinates (angular and vibrational). The expansion functions are eigenfunctions of $\hat{l}^2$ (because l is a good quantum number) as well as eigenfunctions of $\hat{H}_{CH_2}$. Thus, the matrix of $\hat{T}$ [Eq. (3.12)] is diagonal. The matrix of the potential V_N is block-diagonal in J and

M, and also independent of M (since the scattering can't depend on the orientation of the entire system).

The CC equations are then

$$\left[-\frac{d^2}{dR^2} + \frac{l(l+1)}{R^2} - 2\mu(\mathcal{E} - E_{nkv}) \right] C^J_{vnkl}(R) = -2\mu \sum_{v'n'k'l'} V^J_{v'n'k'l',vnkl}(R) C^J_{v'n'k'l'}(R),$$

(3.17)

where the matrix elements of the coupling potential are

$$V^J_{v'n'k'l',vnkl}(R) = \langle n'k'l'JM | \langle v' | V(\mathbf{Q}) | v \rangle | JMnkl \rangle.$$

(3.18)

In scattering calculations, each $|v\rangle|nkl\rangle$ state included in the wave function expansion is called a "channel". If we use a single index m to designate each channel, then Eq. (3.18) can be written as:

$$\left[-\frac{d^2}{dR^2} + \frac{l_m(l_m+1)}{R^2} - 2\mu(\mathcal{E} - E_m) + 2\mu V_{mm}(R) \right] C^J_m(R) = -2\mu \sum_{m' \neq m} V_{m'm}(R) C^J_{m'}(R),$$

(3.19)

It is cleaner to use a matrix representation of Eq. (3.19), namely

$$\left\{ \mathbf{I} \frac{d^2}{dR^2} + 2\mu \left[\mathbf{E} - \mathbf{V}^J(R) - \mathbf{l}(R) \right] \right\} \mathbf{C}^J(R) = 0,$$

(3.20)

Here $\mathbf{E}$ and $\mathbf{l}(R)$ are diagonal matrices with, respectively, elements $\mathcal{E} - E_m$ (E_m being the internal energy of the mth rovibational state) and $l_m(l_m+1)/R^2$.

If we define

$$\mathbf{W}^J(R) = 2\mu \left[\mathbf{E} - \mathbf{V}^J(R) - \mathbf{l}(R) \right],$$

(3.21)

the CC equations become

$$\left[\mathbf{I}\frac{d^2}{dR^2} + \mathbf{W}^J(R)\right]\mathbf{C}^J(R) = 0, \tag{3.22}$$

Since the interaction potential goes to zero when R is infinitely large,

$$\lim_{R\to\infty} W^J_{m'm}(R) = 2\mu(\mathcal{E} - E_m)\delta_{m'm} = 2\mu E^{(m)}_{col}\delta_{m'm} = k_m^2 \tag{3.23}$$

where k_m is the wave vector of the mth channel, which is proportional to the relative translational momentum of the collision of He with CH_2 in its mth vibration-rotation state at total energy $\mathcal{E}$. At large R, the diagonal elements of the $\mathbf{W}$ matrix are proportional to the collision energy in the mth channel.

The mth column of the $\mathbf{C}^J$ matrix corresponds to the expansion coefficients for a collision of He with CH_2 initially in its vibration-rotation state $|n_m k_m\rangle|v_m\rangle$ and with orbital and total angular momenta l_m and J. This solution matrix is matched to the boundary conditions

$$\lim_{R\to\infty} \mathbf{C}^J(R) = e^{-i\mathbf{k}R} - \mathbf{S}^J e^{i\mathbf{k}R}, \tag{3.24}$$

where $\exp(\pm i\mathbf{k}R)$ are diagonal matrices with elements $\exp(\pm ik_m R)$. Here, $\mathbf{S}^J$ is the scattering matrix. The $(mm')^{th}$ element of $\mathbf{S}^J$ corresponds to the probability amplitude that a collision of CH_2, initially in vibration-rotation state $|n_m l_m\rangle|v_m\rangle$ with He, with orbital angular momentum l_m and total angular momentum J, will end up in state $|n_{m'} k_{m'}\rangle|v_{m'}\rangle$ with orbital angular momentum $l_{m'}$ at the same total

44

angular momentum.

A collision between structureless particles is characterized by the energy $\mathcal{E}$ and the impact parameter b. Classically, $\vec{l} = \vec{r} \times \vec{p} = \mu v b$. [62] Each collision is thus characterized by a single orbital angular momentum l. In the case of an inelastic collision, for a given value of the total angular momentum J and for a given value of the rotational angular momentum n of the CH$_2$ molecule, multiple values of both the initial and final orbital angular momenta will contribute.

The integral cross section for a transition from an initial level nkv to a final level $n'k'$v', summed over all values of the initial and final orbital angular momenta, and averaged over the $2n + 1$ degeneracy of the initial rotational level, can then be calculated from

$$\sigma_{nk\text{v} \rightarrow n'k'\text{v}'} = \frac{\pi}{(2n+1)k^2} \sum_{J,l,l'} (2J+1) \left| T^J_{\text{v}nkl,\text{v}'n'k'l'} \right|^2 \tag{3.25}$$

where the transition matrix $\mathbf{T}^J$ is

$$\mathbf{T}^J = \mathbf{I} - \mathbf{S}^J. \tag{3.26}$$

We use the Hibridon [45] code to calculate cross sections for the scattering of He with CH$_2$, by solution of the close-coupled equations.

Since CH$_2$ is an asymmetric top, the rotational levels for a given n are linear combinations of all the k projection states (see Chap. 2). The same linear combinations are the states used for the CC expansion. We note that the crucial vector

coupling presented in Eq. (3.14) is independent of k, and will thus be preserved for an asymmetric top.

The potential matrix in the asymmetric top basis is then an orthogonal transformation (since the number of states and their orthonormality is preserved) of Eq. (3.18). The diagonal $\mathbf{E}$ matrix is also transformed, so that each matrix element corresponds to the vibation-rotational energy of the asymmetric top levels. Once this is done, the CC equations are solved, exactly as in the case of a symmetric top, to yield an S matrix whose entries are probability amplitudes for transitions between the various asymmetric top levels.

In the discussion of this section, we have assumed that the angular momentum of the CH_2 molecule is due only to its rotational motion in space, with quantum numbers n, k, and m_n. In the absence of spin, the total angular momentum of the molecule, j, is thus just equal to n. In Chaps. (4) and (5) we treat collisions of He with CH_2 in, respectively the $^1\tilde{a}$ state, in which there the spin is 0, and in the $^3\tilde{X}$ state, in which the spin is 1. However, since the multiplet splittings due to the electronic spin in the $\tilde{X}$ state are very small (see Table VIII of Ref. [37]), and since the interaction potential contains no spin-dependent terms, in Chap. 5 we treat the CH_2 molecule in the $\tilde{X}$ state as a spin-free (S=0) system. This approximation will certainly be justified if future experiments probing energy transfer in this state are unable to resolve the spin-multiplets.

Chapter 6 treats collisional coupling between the $\tilde{a}$ and $\tilde{X}$ states, within the framework of the mixed-state model introduced in Sec. 2.2.4. In this Chapter, we still use Eq. (3.25) to determine inelastic cross sections but for transitions involving

one (or two) of the mixed state levels, the T-matrix elements are modified following Eqs. (2.22)–(2.28). Since the mixing angle [Eq. (2.20)] is a function only of the properties of the isolated CH_2 molecule, Eqs. (2.22)–(2.28) can be used without change in all the terms in the summation over the initial and final orbital angular momenta l and l' as well as over the total angular momentum J.

In Chap. 6, specifically in Sec. 6.3.3, we expand the scattering calculation to determine cross sections for transitions between the three spin-multiplets of each rotational level of $CH_2(\tilde{X})$, namely $j = n - 1, n, n + 1$. We will find a strong $\Delta j = \Delta n$ propensity rule: almost all the collision flux occurs for transitions in which the relative orientation of $\vec{n}$ and $\vec{S}$ is preserved.

3.3   Fitting the CH_2-He Potential Energy Surface

To calculate the matrix elements of the interaction potential [Eq. (3.18)] we expand the PES in a set of orthogonal functions. We fit the expansion coefficients to the results of our *ab initio* calculations, which is a set of numerical values of the electronic energy on a grid which spans the coordinate space. As seen explicitly in Eq. (3.18), this coordinate space includes the rotational motion of the CH_2, the vibrational motion of the CH_2, and the motion of the He atom around the center-of-mass of the CH_2. It is simplest to assume a rigid CH_2 molecule, in which case the innermost integration in Eq. (3.18) (the integration over the vibrational motion) is just a delta function corresponding to a rigid molecule in a particular bending

vibrational state. In other words, we assume

$$\langle v'|V(\mathbf{Q})|v\rangle \approx \delta_{vv'}V(\mathbf{Q}_e)$$

Because the CH_2 molecule in the $\tilde{X}$ state is floppy, we determine the dependence of the interaction potential on the bending vibrational coordinate, and then integrate over this coordinate, weighting by the the square of the bending vibrational wave function. We then have a vibrationally-averaged interaction potential $V_{v'v}$.

We then expand the vibrationally-averaged potential or the interaction potential evaluated at $\mathbf{Q}_e$ in a basis consisting of spherical harmonics, for which the z axis is the principal axis of the CH_2 molecule. Earlier studies of the scattering of He with the spherical top NH_3 molecule, [63] also used an expansion in spherical harmonics, but oriented with respect to the C_3 axis.

We have

$$V(R,\theta,\phi) = \sum_{\lambda\mu} v_{\lambda\mu}(R)Y_{\lambda\mu}(\theta,\phi). \tag{3.27}$$

As discussed in Sec. 2.2.1, the CH_2 molecule has two reflection planes: xz and xy in Fig. 2.5. The interaction potential must be symmetric with respect to reflection in these planes. Or, mathematically

$$V(R,\theta,\phi) = V(R,\theta,-\phi) = V(R,\pi-\theta,\phi). \tag{3.28}$$

Because [64,65]

$$Y_{\lambda\mu}(\theta,-\phi) = (-1)^{\mu}Y_{\lambda-\mu}(\theta,\phi)$$

and

$$Y_{\lambda\mu}(\pi - \theta, \phi) = (-1)^{\lambda+\mu}Y_{\lambda\mu}(\theta, \phi)$$

the xz and xy reflection symmetries may be satisfied by restricting the summation in Eq. (3.27) to terms with $(\lambda + \mu)$ even. We then have

$$V(R, \theta, \phi) = \sum_{\lambda, 0 \leq \mu \leq \lambda} v_{\lambda\mu}(R) \left[1 + \delta_{\mu 0}\right]^{-1} \left[Y_{\lambda\mu}(\theta, \phi) + (-1)^{\mu}Y_{\lambda-\mu}(\theta, \phi)\right], \qquad (3.29)$$

Chapters 4 and 5 give more detail on the range of λ and μ included in the expansion of the $CH_2(\tilde{a})$–He and $CH_2(\tilde{X})$–He PES's.

3.4   Thermal Rate Constants and the Master Equation

The inelastic cross sections given by Eq. (3.25) are functions of the collision energy, which is the total energy minus the internal energy of the mth channel. Here, since the He atom is structureless, the internal energy is the rotational-vibrational-electronic (rovibronic) energy of level nkv. Alternatively, the cross section is a function of the initial relative velocity between the He atom the the CH_2 in level nkv, namely

$$v_m = \left[2\mu E_{col}^{(m)}\right]^{1/2}. \qquad (3.30)$$

Multiplication by the collision velocity gives a flux (number per unit time per unit area). If we then multiply by the number density of He, we would obtain the rate (number per unit time) that CH_2 would be converted from level nkv to level $n'k'$v'. Thus, the product of the collision velocity times the cross section is the rate constant

at relative collision velocity v.

At thermal equilibrium there will be a Maxwellian distribution of collision velocities. The thermal rate constant, for a transition from level m to level m' is then

$$k_{mm'}(T) = \int_0^\infty v\sigma_{mm'}(v)f(v)dv$$

where $f(v)$ is the Maxwell velocity distribution [66]

$$f(v) = \left(\frac{\mu}{2\pi k_B T}\right)^{3/2} 4\pi v^2 \exp\left(-\mu v^2/2k_B T\right).$$

Here k_B is the Boltzmann constant. From the relation between the collision energy and the relative velocity [Eq. (3.30)], we can convert the integral over velocity to an integral over collision energy, obtaining [67]

$$k_{mm'}(T) = \left(\frac{8}{\pi\mu(k_B T)^3}\right)^{1/2} \int_0^\infty \sigma_{m\to m'}(E_c)\, E_c \exp\left(-E_c/k_B T\right) dE_c, \qquad (3.31)$$

In practice, cross sections are calculated on a dense grid of total energies $\mathcal{E}$. For a given initial state this grid is shifted, by the internal energy of the initial state, into a grid of collision energies. Interpolation of this data allows us to determine the rate constants at temperature T by numerical integration of Eq. (3.31).

Now consider the relaxation of a manifold of M rotational levels. The time dependence of population in each level is governed by a master equation of dimen-

sionality M. We write this in matrix notation as

$$\frac{d\mathbf{N}}{dt} = \rho\mathbf{K}\mathbf{N} \tag{3.32}$$

Here $\mathbf{N}$ is a column vector of the populations, namely (here we save space by giving the transpose of this column vector)

$$\mathbf{N}^T = \begin{bmatrix} N_{s_1} & \cdots & N_A & \cdots & N_{s_p} & N_{t_1} & \cdots & N_X & \cdots & N_{t_q} \end{bmatrix}$$

Note that we are here using n as a single index for a set of rotation-vibration levels (which have quantum numbers n, k, and v). The ij^{th} element of the matrix of rate constants $\mathbf{K}$ is the rate constant, at temperature T for a transition from level j to level i (note the ordering). The k_{ij} and k_{ji} rate constants satisfy detailed balance, namely

$$g_i \exp\left(-E_i/k_B T\right)k_{i\rightarrow j} = g_j \exp\left(-E_j/k_B T\right)k_{j\rightarrow i}, \tag{3.33}$$

where g_i is the degeneracy of the ith level, k_B is the Boltzmann constant and E_i is the internal energy of the ith level. The diagonal element k_{ii} is equal to the inelastic loss rate for level i, namely

$$k_i = -\sum_{j\neq i} k_{ji}$$

In other words the diagonal elements are the negative of the sum of all the off-diagonal elements in the same column, or, equivalently, each column of the rate constant matrix $\mathbf{K}$ adds to zero.

Alexander, Dagdigian, and Hall [48] have shown how the master equation can be solved by transforming to diagonalizing the problem by working in a basis of linear combinations of the level populations. Each one of these sets of populations decays exponentially, with a rate constant equal to the diagonal elements of the transformed rate matrix. The lowest eigenvalue is zero. The corresponding eigenvector is the Boltzmann equilibrium population. Thus, any arbitrary initial population will always decay to a Boltzmann distribution.

Chapter 4: Rotationally Inelastic Collisions of $CH_2(\tilde{a})$ with Helium

This chapter reports our investigation of rotationally inelastic collisions of $CH_2(\tilde{a})$ with the helium atom. We give the details and results of the *ab initio* calculations for $He-CH_2(\tilde{a})$, done with the CCSD(T) method and MOLPRO suite of programs, [51] both discussed in Chap. 3. As mentioned above in Sec. 2.2.1, in the $\tilde{a}$ state there is a lone pair of electrons in the $3a_1$ orbital and an empty non-bonding orbital perpendicular to the molecular plane. The strongly-anisotropic electron density gives rise to a strongly-anisotropic PES. Hence, we expect significant rotational inelasticity within the $\tilde{a}$ state.

We first fit the calculated interaction energy, for a rigid CH_2 structure, with an expansion in spherical harmonics. We then carried out scattering calculations using the HIBRIDON suite of programs. [45] We present and analyze the state-to-state and total removal cross sections for transitions at a collision energy of 300 cm^{-1}. We attempt to correlate the size of various terms in the expansion with the magnitude of the cross sections. We calculate the room temperature rate constant by averaging the cross sections over a Maxwellian distribution of collision energy. Finally, we compare the computed rate constants for overall depletion of selected $k_a = 1$ levels with experimental results from Komissarov, Hall and Sears. [12]

The following part of this chapter is reproduced with some changes from our published paper: L. Ma, M. H. Alexander and P. J. Dagdigian, *Theoretical investigation of rotationally inelastic collisions of* $CH_2(\tilde{a})$ *with helium*, J. Chem. Phys. **134**, 154307 (2011). [17] As a consequence, some of the introductory material as well as the general descriptions of the calculations, contain material that has already be presented in Chapters 2 and 3 of this dissertation.

In this, as well as in our second published paper on collisions of He with $CH_2(\tilde{X})$, [18] we did not explicitly include the spin. We used j to designate the rotational angular momentum of the CH_2 molecule. Here, we prefer to use j for the total molecular angular momentum (including the spin), and n for the rotational angular momentum of CH_2. This allows us, specifically in Chap. 6, to include spin, vector-coupling $\vec{S}$ with $\vec{n}$ to form $\vec{j}$.

4.1   Introduction

Rotational energy transfer is an important collisional process in many environments and plays a key role in thermalizing non-equilibrium rotational state distributions. Molecular beam and laser techniques, [68, 69] as well as double-resonance experiments in cells, [70–75] have provided state-to-state integral and differential rotationally-inelastic cross sections, and inelastic rate constants, for a large number of diatomic molecules. Concurrently, there have been many quantum scattering calculations of these cross sections and rate constants, based on high-quality *ab initio* potential energy surfaces (PESs). [70–72, 75–78]

By contrast, there has been less study of state-to-state collision-induced rotational transitions in triatomic and larger molecules. Dagdigian [79] and Dearden *et al.* [80] studied collisional rotational energy transfer in NH_2 in its ground $\tilde{X}^2B_1$ and $\tilde{A}^2A_1$ excited electronic states, respectively. Two groups have carried out state-to-state molecular beam studies of collisions of NH_3 with Ar, [81,82] and comparison has been made with quantum scattering calculations. [83] Nesbitt and co-workers have utilized direct infrared absorption with a high-resolution laser in molecular beam studies of state-to-state rotational transitions in CH_4 and H_2O in collisions with rare gases. [84,85] They found reasonable agreement of their measured integral cross sections with the results of quantum scattering calculations on the CH_4–He and H_2O–Ar systems.

This chapter addresses rotationally inelastic collisions in singlet methylene, $CH_2(\tilde{a})$. Although it has only 6 valence electrons, methylene has a rich spectroscopy and complex collision dynamics. The ground triplet $\tilde{X}^3B_1$ and low-lying singlet $\tilde{a}^1A_1$ electronic states have dramatically different reactivities, so that these states must be considered as separate chemical species in combustion modeling. [86] Complicating an understanding of the reactivity of these states is facile collisional $\tilde{X}$–$\tilde{a}$ intersystem crossing, which proceeds through "gateway" rotational levels of mixed electronic character. [10,12,14,15] Collisional relaxation of methylene involves these intersystem gateways, as well as rapid rotational energy transfer within, separately, the $\tilde{a}$ and $\tilde{X}$ electronic states.

Sears, Hall, and their co-workers used the technique of Doppler resolved transient frequency modulation absorption spectroscopy to study the collision-induced

thermalization, intersystem crossing, and chemical reaction of $CH_2(\tilde{a})$. [12, 14] This technique has recently been extended to allow the study of state-resolved collisional rotational energy transfer from specified rotational levels by saturation recovery experiments, in particular for collisions of $CH_2(\tilde{a})$ with helium and argon. [12, 14] In these experiments the population in a particular $CH_2(\tilde{a})$ rotational level is initially depleted by electronic excitation with a pulsed laser. Using frequency modulation absorption spectroscopy, Sears, Hall, and their co-workers follow the time-dependent repopulation of this level. The rate constant for this process is identical to the rate constant for collision depletion of the level in question.

There has been significant interest in the detection of collisional changes in the orientation and alignment moments of m-state populations. In principle, these can provide additional insight into the collision dynamics beyond that provided by measurement of changes in state populations. [87–93] This chapter is organized as follows: the next section presents the details of the *ab initio* calculation of the $CH_2(\tilde{a})-$He PES and a fit of the computed points to a form suitable for quantum scattering calculations. Sec. 4.3 describes the methodology of the scattering calculations. We report in Sec. 4.4 state-to-state cross sections and rate constants and discuss propensity rules. In Sec. 4.5 we compare our calculated rate constants with the experimental results of Sears, Hall, and co-workers.

4.2 Potential Energy Surfaces

The description of the potential energy surface for the interaction of a nonlinear triatomic molecule with an atom has been presented previously. [63,94] The potential energy depends upon the orientation (θ, ϕ) and the distance R with respect to the center-of-mass of the molecule. With the molecule placed in the xz plane and the z-axis lying along the a inertial axis, the interaction can be conveniently expressed in terms of spherical harmonics as (see, also, Sec. 3.3)

$$V(R, \theta, \phi) = \sum_{\lambda,\mu} v_{\lambda\mu}(R)(1 + \delta_{\mu 0})^{-1} \left[Y_{\lambda\mu}(\theta, \phi) + (-1)^{\mu} Y_{\lambda,-\mu}(\theta, \phi) \right] \qquad (4.1)$$

This body-frame coordinate system is illustrated in Fig. 2.5.

Our choice of this frame differs from the convention of Green and co-workers, [95] who defined the z axis to lie along the C_2 symmetry axis, which corresponds to the x axis in Fig. 2.5 and which is perpendicular to the a inertial axis. In the interaction of a nonlinear symmetric AB_2-type triatomic molecule with an atom, with our choices of axes the only nonzero terms in the expansion in Eq. (4.1) have $\lambda + \mu$ even. The expansion of the potential with our choice of frame requires more terms than for the frame used by of Green and co-workers, but the expressions for the rotational wavefunctions are more diagonally dominant.

The *ab initio* calculations of the $CH_2(\tilde{a})-He$ potential energy surface were carried out with the MOLPRO 2009.1 suite of computer codes. [51] Since we are interested in rotational excitation at relatively low collision energies, we determined

the potential energy surface (PES) by means of coupled cluster calculations with inclusion of single, double, and (perturbatively) triple excitations (CCSD(T)). [53, 96] The bond length and bond angle of the $CH_2(\tilde{a})$ molecule were held fixed at $R = 2.101$ bohr and $\theta = 101.77°$. These values were computed by Petek *et al.* [32] using the A_e and B_e rotational constants obtained from analysis of infrared absorption spectra of $CH_2(\tilde{a})$ in the hydride stretch region. An atom-centered, *avqz* atomic-orbital basis was used, [58] with the addition of a set of bond functions located at the mid-point of $\vec{R}$. [59, 60]

The calculations were carried out on a grid of 19 values of the atom-molecule separation [R (in bohr) $= 3.5 - 10$ in steps of 0.5; 11, 12, 13, 15, and 20] and 190 distinct orientations [19 values of θ, evenly spaced over between $0°$ and $90°$, and 10 values of ϕ, evenly spaced between $0°$ and $180°$, for a total of 3610 points. The potential energy at other orientations can be related by symmetry to values within the calculated range of orientations. The computed potential energies as a function of R and the orientation were fitted with the expansion given in Eq. (4.1), as in our recent work on H_2O–He collisions. [97] In the angular expansion we included all terms with $\lambda \leq 6$ and $\mu \leq 2$.

The global minimum of the PES has an energy ~ 134 cm^{-1} The minimum lies at $R = 4.58$ bohr, $\theta = 90°$, $\phi = 100.8°$. Figure 4.1 presents a contour plot of the dependence of the potential energy upon the orientation at the atom-molecule separation at $R = 4.58$ bohr, corresponding to the global minimum. We see that the PES is strongly anisotropic. In the most attractive orientation, the helium atom lies above (or, by symmetry, below) the molecular plane. At this atom-molecule
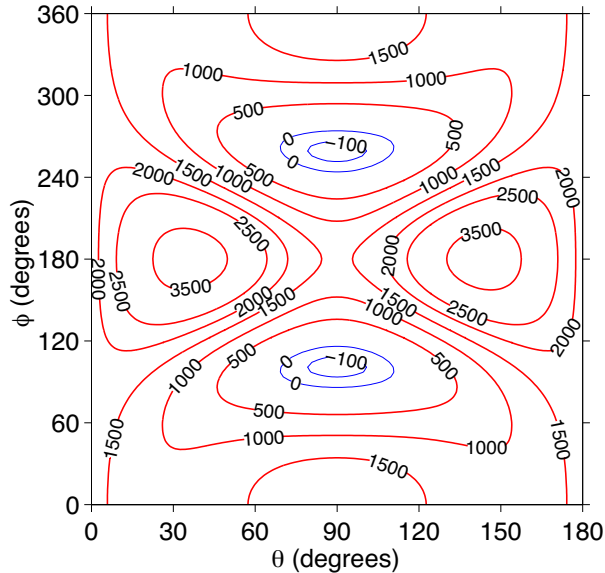
Figure 4.1: Dependence of the potential energy (in cm^{-1}) on the orientation of the helium with respect to the CH$_2(\tilde{a})$ molecule for an atom-molecule separation $R = 4.58$ bohr. Repulsive energy contours are drawn in red, attractive energy contours in blue.

separation, there is a large barrier to move the helium atom from the potential minimum on one side of the molecule to the other, keeping the angle θ fixed at 90°.

It is interesting to compare the topology of the CH$_2(\tilde{a})-$He PES with that of H$_2$O$-$He. [98] The CH$_2(\tilde{a})-$He PES is much more strongly anisotropic. Moreover, the most attractive orientation for the former system has the helium atom perpendicular to, rather than in, the molecular plane. In addition, the well depth for the CH$_2(\tilde{a})-$He PES is significantly larger than that for H$_2$O$-$He [134 *vs.* 35 cm^{-1}], and the atom-molecule separation at the minimum of the PES is significantly smaller [4.58 *vs.* 5.92 bohr].

We can understand the differences in the topology of these two PESs from considerations of electronic occupancy. In linear geometry, the lowest-energy singlet state of CH$_2$ has Δ_g symmetry, which corresponds in terms of Cartesian orbitals to

59
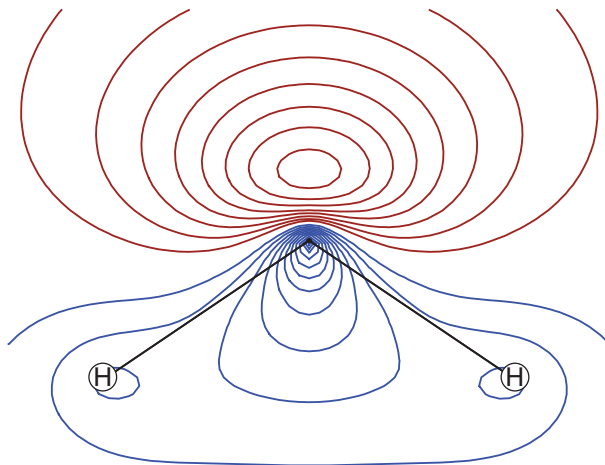
Figure 4.2: Contour plot of the highest-occupied molecular orbital ($3a_1$) of the $CH_2(\tilde{a})$ molecule. This is the higher in energy of the two bonding molecular orbitals ($1b_2$ and $3a_1$).

the electron occupancies π_{xy} and $\pi_{x^2-y^2}$. As the molecule bends, the degeneracy of this state is lifted. In the lower component of this Renner-Teller pair, designated the $^1\tilde{a}$ state, the two electrons occupy the orbital which corresponds to the in-plane distortion of the linear π orbital. This orbital is shown in Fig. 4.2. The lowest unoccupied orbital is the out-of-plane π orbital.

The strongly anisotropic, attractive nature of the PES is due to the interaction of the electrons on the helium atom with this unoccupied orbital. In chemical terms, CH_2 in the $\tilde{a}$ state behaves as a Lewis acid when He approaches in the plane of the molecule, but as a Lewis base when He approaches perpendicular to the plane of the molecule. By contrast, in H_2O, where the central atom has two more electrons, the orbital perpendicular to the molecular plane is doubly occupied, so that its interaction with helium is more isotropic and, simultaneously, less attractive than for $CH_2(\tilde{a})$.

Figure 4.3 presents plots of the largest expansion coefficients $v_{\lambda\mu}$ as a function
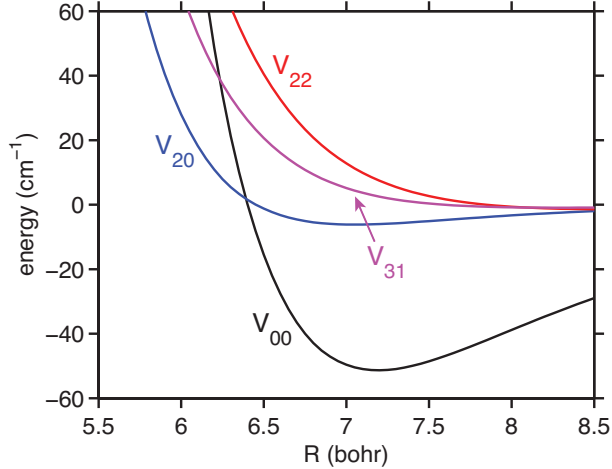
Figure 4.3: Dependence on the He−CH$_2$($\tilde{a}$) distance of the larger of the expansion coefficients $v_{\lambda\mu}$ [defined in Eq. (4.1)].

of the atom-molecule separation R for the CH$_2$($\tilde{a}$)–He PES in the region of the van der Waals well. As an indication of the strong anisotropy of this surface, the minimum in the isotropic v$_{00}$ term occurs at $R = 7.19$ bohr, whereas the global minimum occurs at $R = 4.58$ bohr. We see in Fig. 4.3 that the coefficients v$_{\lambda\mu}$ for $\mu \geq 1$ are comparable in magnitude to those for $\mu = 0$.

At smaller values of R than shown in Fig. 4.4, the v$_{22}(R)$ and the v$_{31}(R)$ terms are (as in Fig. 4.3) also the largest. The dominance of these two terms is easy to understand by reference to the contour plot shown in Fig. 4.1. The dependence on θ, ϕ of the $\lambda = \mu = 2$ term in Eq. (4.1) is

$$V_{22}(R, \theta, \phi) \sim \cos 2\phi \sin^2 \theta. \tag{4.2}$$

This term is largest for $\theta = 90°$. The variation in ϕ corresponds to the alternation in the PES along this line between the wells at $\phi = 90°$ and $270°$ and the relative
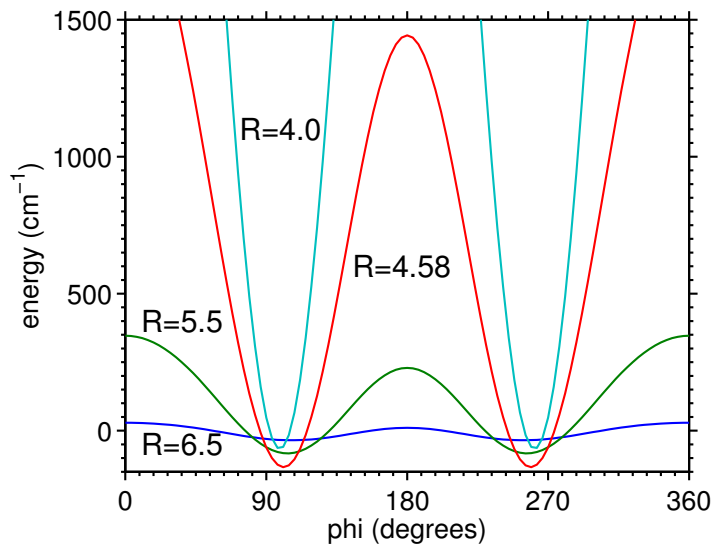
Figure 4.4: Dependence of the potential energy for the interaction of $CH_2(\tilde{a})$ with helium upon the angle ϕ for $\theta = 90°$ at several values of the atom-molecule separation R (given in bohr). The motion shown here corresponds to rotation of the He atom in the xy-plane in Fig. 2.5.

maxima at $\theta = 0°$, $180°$, and $360°$. It is this variation which is a reflection of the amphoteric Lewis acid/base behavior of CH_2 as He approaches in the plane of the molecule or perpendicular to this plane. Thus, this electronic asymmetry dominates the anisotropy of the CH_2–He interaction. Except for large atom-molecule separations ($R > 7$ bohr), the orientation of the most attractive interaction at a given value of R has $\theta = 90°$ and $\phi \approx 100°$ and $\approx 260°$. The dependence of the potential energy upon the angle ϕ for $\theta = 90°$ is plotted in Fig. 4.4 for several values of the atom-molecule separation R. We see that the value of ϕ at the most attractive Lewis-base orientation varies only slightly with R.

The θ, ϕ dependence of the $\lambda = 3, \mu = 1$ term in Eq. (4.1) is

$$V_{31}(R, \theta, \phi) \sim \cos\phi \sin 2\theta (1 - 5\cos^2 2\theta). \tag{4.3}$$

62

This term is largest for $\theta = 60°$ and $150°$ with $\phi = 180°$, which corresponds, closely, to the positions of the two H atoms. Thus, the large v_{31} term reflects the anisotropy of the $CH_2(\tilde{a})$–He PES due to the presence of the two H atoms.

The $\mu \geq 1$ coefficients couple directly rotational levels differing in values of the body-frame projection quantum number k_a. In the discussion below, we will use the relative magnitudes of the $v_{\lambda\mu}$ terms to explain the propensities for collisional change in this projection quantum number that emerge from our scattering calculations.

4.3 Scattering Calculations

Full close-coupling scattering calculations of the collision of specified rotational levels of $CH_2(\tilde{a})$ with helium were performed with the Hibridon suite of programs. [45] We have recently expanded Hibridon to include collisions of a closed-shell asymmetric top with a closed-shell atom. [97] Care was taken to include a sufficient number of both energetically closed channels and partial waves to ensure convergence of the cross sections.

Rotational energies and wave functions were computed with a rigid rotor asymmetric top Hamiltonian, using rotational constants $A = 20.118$ cm^{-1}, $B = 11.205$ cm^{-1},, and $C = 7.069$ cm^{-1}, taken from spectroscopic analysis [39] absorption spectrum [38] of CH_2.

To compute rate constants, the cross sections were computed over a grid of collision energies, up to total energies of 2400 cm^{-1}, and averaged over a room-temperature ($T = 298$ K) Maxwellian distribution of relative collision energies E_c

[see also Eq. (3.31)]. [67]

$$k_{i \to f}(T) = \left(\frac{8}{\pi \mu (k_B T)^3} \right)^{1/2} \int_0^\infty \sigma_{i \to f}(E_c) E_c \exp\left(-E_c/k_B T\right) dE_c, \qquad (4.4)$$

where k_B is the Boltzmann constant.

4.4 Results

We will attempt to correlate the magnitude of the cross sections for collision-induced rotational transitions in $CH_2(\tilde{a})$ with the quantum numbers and energies of the rotational levels. For an asymmetric top, the rotational levels are labeled by the rotational angular momentum n, which is a good quantum number, as well as by the prolate-limit body-frame projection quantum number k_a, which is an approximate quantum number that becomes exact in linear geometry. Usually, the levels of an asymmetric top are also labeled [99] by the oblate-limit quantum number k_c.

In CH_2, as in other symmetrical bent triatomic molecules, the Hamiltonian is invariant with respect to permutation of the two terminal nuclei (in this case, H nuclei). In Fig. 4.5 we show the positions of the lower rotational energy levels of $CH_2(\tilde{a})$, designating the *ortho* and *para* nuclear spin modifications by solid and dashed lines, respectively. Collisions with helium will not lead to transitions between levels of *ortho* and *para* permutation symmetry.

For $k_a = 0$, levels with even and odd values of the rotational angular momentum n correspond, distinctly, to *para* and *ortho* permutation symmetry, respectively. For higher values of k_a, each rotational level is present for both permutation sym-
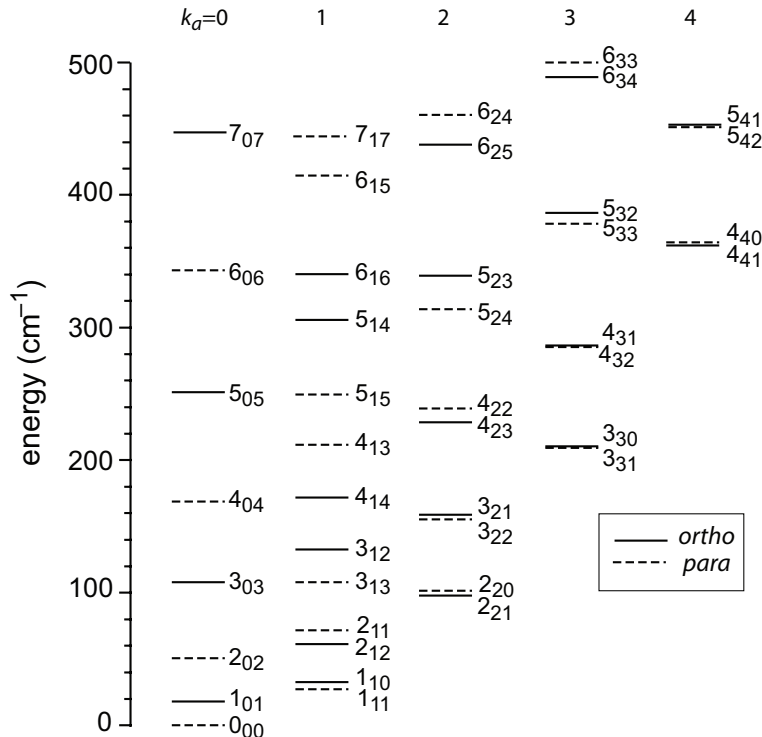
Figure 4.5: Rotational levels of *ortho–* (solid) and *para–*$CH_2(\tilde{a})$ with energies less than 500 cm^{-1}. The levels are grouped by column according to the value of the prolate-limit body-frame projection quantum number k_a. The individual rotational levels are labeled by the rotational angular momentum n and by its projections along the a and c inertial axes: k_a and k_c.

metries. For even values of n, the lower (upper) level of this pair belongs to the *ortho (para)* nuclear spin modification. The opposite labeling occurs for odd values of n. In a symmetric top (such as NH_3) the *ortho* and *para* levels are nearly degenerate. However, we see in Fig. 4.5 that even for $CH_2(\tilde{a})$, which is a near-prolate top, there is a large splitting between levels of the same n. This so-called asymmetry splitting [99] between levels of the same n is largest for $k_a = 1$ and increases with increasing n. As we will see below, these unequal energy spacings lead to interesting propensities in the cross sections for collision-induced rotational transitions.

4.4.1 State-to-State Rotationally Inelastic Collisions

Figure 4.6: Bar plot of the cross sections for rotationally inelastic scattering of *para* $CH_2(\tilde{a})$ in the $n = 4$ and 5, $k_a = 1$ levels by collision with He at a collision energy of 300 cm^{-1}. The red square denotes the initial level.

In collisions of a diatomic molecule, inelastic energy transfer can occur only by changes in the rotational angular momentum n. A number of models have been developed which relate the size of the cross section to the magnitude of either the energy gap between the initial and final rotational levels or to the absolute value of the change in rotational angular momentum $|\Delta n|$. [100] In collisions of a polyatomic top, collisions can cause a change in both n and its body-frame projection. To gain some insight into the relative ease of these two inelastic events, we compare in

Fig. 4.6 the state-to-state cross sections for transitions out of the *para* $k_a = 1$, $n = 4$ and 5 levels for a collision energy of 300 cm^{-1}, which is approximately the average collision energy at room temperature. Figure 4.7 makes the same comparison for the *ortho* $k_a = 1$, $n = 4$ and 5 levels.

Figure 4.7: Bar plot of the cross sections for rotationally inelastic scattering of *ortho* CH$_2(\tilde{a})$ in the $n = 4$ and 5, $k_a = 1$ levels by collision with He at a collision energy of 300 cm^{-1}. The red square denotes the initial level.

We see in Figs. 4.6 and 4.7 that the transitions which conserve k_a (specifically,

the $k_a = 1 \rightarrow k_a = 1$ transitions), show a dependence upon the final rotational angular momentum n' similar to that usually observed in collisions of diatomic molecules: These cross sections decrease monotonically as $|\Delta n|$ increases. Transitions into other k_a manifolds display significant cross sections for a range of n', centered roughly about the initial rotational angular momentum n. The transitions that make the dominant contribution to the larger total removal cross section for the *para* $n = 4$ and *ortho* $n = 5$ levels are the $\Delta k_a = 0$, $\Delta n = +1$ and $\Delta k_a = +2$ transitions. For the *ortho* $n = 4$ and *para* $n = 5$ levels, the largest cross section is for the $\Delta k_a = 0$, $\Delta n = -1$ transition.

In part, we can understand the dependence of the cross sections for the $\Delta k_a = 0$, $\Delta n = +1$ transition upon n by reference to the energy level diagram in Fig. 4.5 For *ortho* CH_2 the energy gap between the $k_a = 1$, $n = 5$ and 6 levels is 42 cm^{-1}, but rises to 176 cm^{-1} between the corresponding $n = 4$ and 5 levels. Similarly, the energy gaps between the n and $n+1$ levels are much smaller for odd- *vs.* even-n *ortho* $k_a = 1$ levels and for even- *vs.* odd-n *para* $k_a = 1$ levels. We note that the potential coupling matrix elements between n and $n+1$ levels in the same k_a manifold do not depend strongly upon n, and in particular do not alternate in magnitude between even and odd initial n.

We turn now to a discussion of the $\Delta k_a = +2$ transitions. We observe in Fig. 4.5 that the energy gap for the $\Delta k_a = +2$, $\Delta n = 0$ transition is nearly the same for the *ortho* $k_a = 1$, $n = 4$ and 5 levels (the $4_{14} \rightarrow 4_{31}$ and $5_{14} \rightarrow 5_{32}$ transitions). More generally, for both *ortho* and *para* $CH_2(\tilde{a})$ the energy gaps for $\Delta k_a = +2$, $n \rightarrow n'$ transitions do not vary significantly when textit$n$ changes from even to odd. Thus,

the explanation for the even-odd alternation in the magnitude of the cross sections for the $\Delta k_a = +2$ transitions seen in Figs. 4.6 and 4.7 lies not in a variation in the energy gaps but rather in the magnitude of the coupling matrix elements between initial and final levels.

The $\mu = 2$ terms in the angular expansion of the PES [Eq. (4.1)] are the lowest-order terms which can directly couple the $k_a = 1$ and 3 levels. As discussed earlier, and as seen in Fig. 4.3, the largest of these terms is v_{22}. In a body-frame expansion of the potential, the matrix of the coupling potential is block-diagonal in k, the body-frame projection of the total angular momentum J. [63] Evaluation of the matrix elements of these terms shows that for $k_a = 1 \rightarrow 3$, $n \rightarrow n'$ transitions between *ortho* states, the matrix elements of the v_{22} term are largest for n odd. For comparable transitions between *para* states, the matrix elements of the v_{22} term are largest for n even. This is consistent with the variation in the $\Delta k_a = +2$, $\Delta n = 0$ cross sections shown in Figs. 4.6 and 4.7.

Thus, the most apparent propensities in the inelastic scattering of $CH_2(\tilde{a})$ by He are the result of both the large asymmetry splitting in the rotational levels in the $k_a = 1$ stack, and the dominance of the v_{22} term in causing k_a changing transitions. This latter is due to the marked electronic anisotropy of CH_2 in the $\tilde{a}$ state.

As mentioned earlier, there have been a number of papers in the literature in which the relative magnitude of cross sections for rotationally-inelastic collisions of a diatomic molecule have been modeled entirely by a (negative) exponential or inverse power-law dependence on the magnitude of the energy gap. To investigate the applicability of this model here, we display in Fig. 4.8 the same inelastic cross
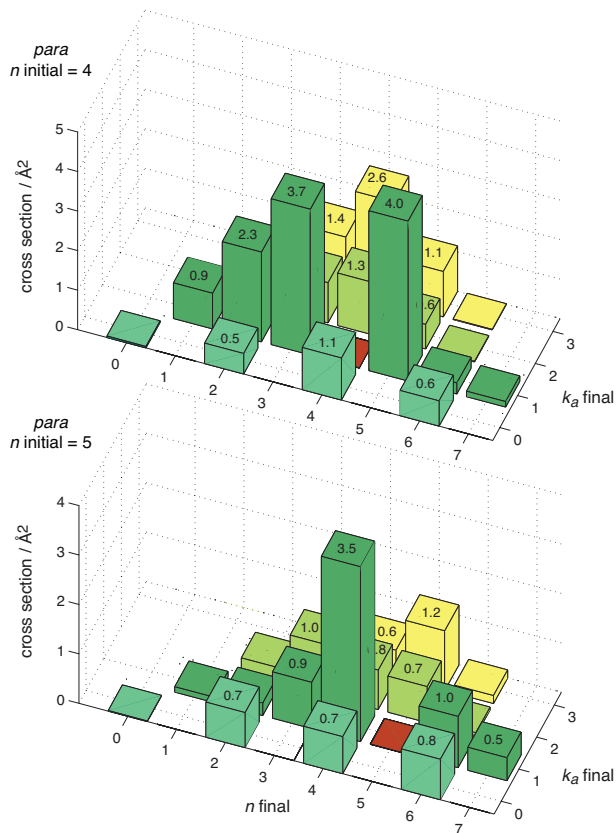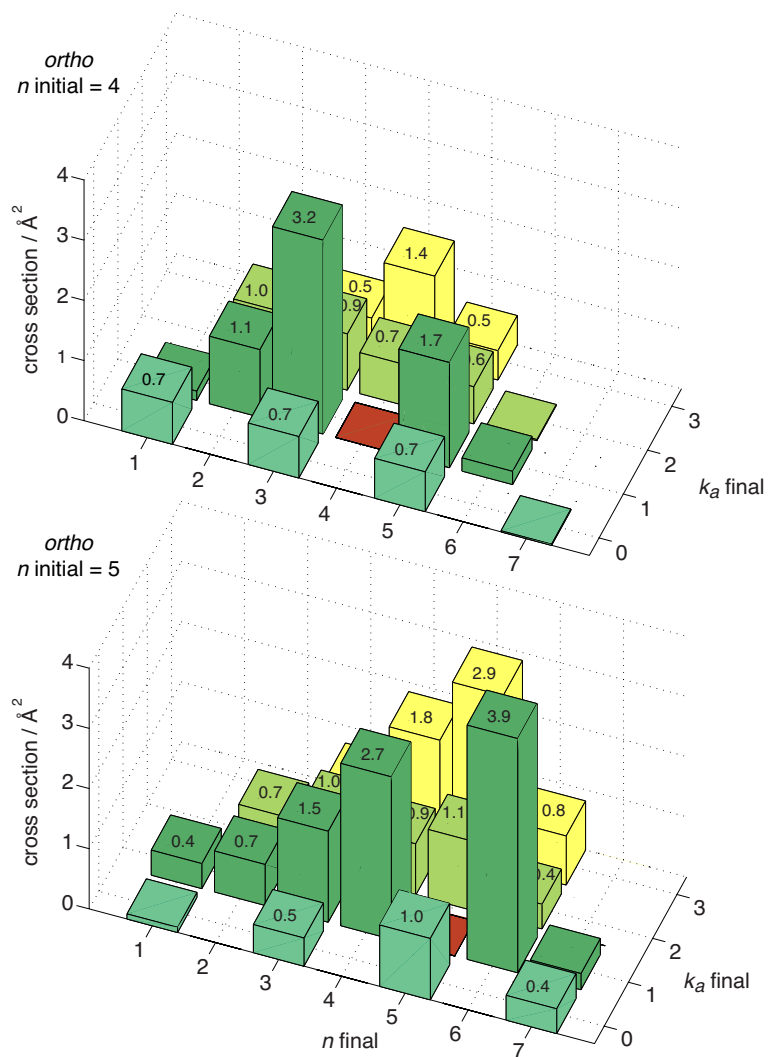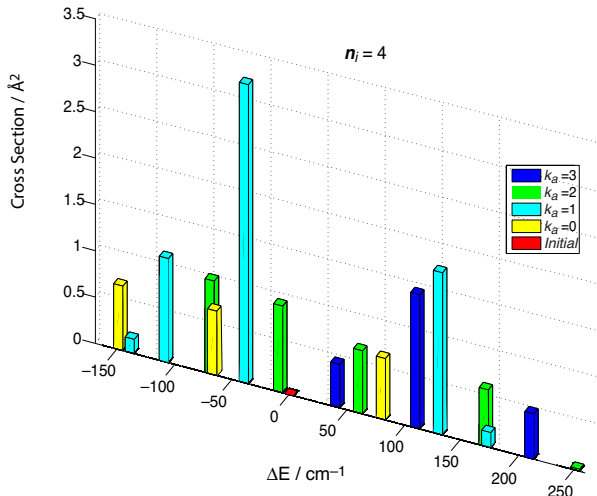
Figure 4.8: Bar plot of the cross sections for rotationally inelastic scattering of *ortho* $CH_2(\tilde{a})$ in the $n = 4$, $k_a = 1$ level by collision with He at a collision energy of 300 cm^{-1}, plotted here against the energy gap, with $\Delta E = E(n'k_a') - E(nk_a)$. The red square denotes the initial level.

sections as shown in the upper panel of Fig. 4.7 [cross sections out of the $n = 4$, $k_a = 1$ level of *ortho* $CH_2(\tilde{a})$], but here plotted against the energy gap. Even though the strong even-odd, *ortho-para* propensities seen in Figs. 4.6 and 4.7 correlate, at least partially, with the energy gaps within the $k_a = 1$ ladder, overall, rotationally-inelastic collisions in a bent triatomic, at least in the case of $CH_2(\tilde{a})$–He collisions, cannot be fit by either an exponential or power-law dependence on the energy gap. This conclusion is entirely similar to that of Green, in an earlier examination of inelastic scattering in linear and bent rotors. [101]

In Table 4.1 we list the total cross section for inelastic removal of the initial state, [defined in Eq. (4.7) below], as well as the average values of $|\Delta n|$ and $|\Delta k_a|$, weighted by the magnitude of the state-to-state cross sections, for transitions out of

Table 4.1: Overall inelasticity of $n = 4$ and 5, $k_a = 1$ rotational levels of *para* and *ortho* $CH_2(\tilde{a})$ in collision with He at a collision energy of 300 cm^{-1}.

	ortho		*para*	
Quantity	$n = 4$	$n = 5$	$n = 4$	$n = 5$
$\sigma^{(R)}/$ Å^2	14.2	21.8	22.9	13.7
$< \|\Delta n\| >$	1.1	1.2	1.1	1.3
$< \|\Delta k_a\| >$	0.71	0.85	0.73	0.69

the $n = 4$ and 5, $k_a = 1$ levels. These averages are defined by

$$< |\Delta n| >= \sum_{n'k'_a} |n' - n|\sigma_{nk_a \to n'k'_a}/\sum_{n'k'_a} \sigma_{nk_a \to n'k'_a} \tag{4.5}$$

and similarly for $< |\Delta k_a| >$. We observe a dramatic variation in the total removal cross sections going from $n = 4$ to $n = 5$. This is the cumulative effect of both the asymmetry splitting of the rotational energy levels and the dominance of the v_{22} term in the potential, both discussed in the previous section.

In contrast, perhaps, the average changes in both the rotational quantum number and its projection vary little between the two nuclear spin modifications and with the parity of n. On the average, each collision results in a change in n of roughly $\hbar$ and a change in k_a of roughly $\frac{3}{4}\hbar$. As can be seen in Fig. 4.9(a), the alternation in n of the relative magnitudes of the total removal cross sections, which is reversed between the two nuclear spin modifications, persists over a wide range of initial states.

71

4.4.2 Overall Rotational Relaxation

In their study of rotational energy transfer in collisions of with helium, Sears, Hall, and their co-workers [12,14] have concentrated on an investigation of the *ortho* levels in the $k_a = 1$ manifold. As discussed in the Introduction, in one type of measurement, they determined bimolecular rate constants for the refilling of a hole in the population of a specified rotational level, prepared by pulsed laser electronic excitation. This type of rate constant may readily be shown to be equivalent to the rate constant for total rotationally inelastic removal. [48]

In this latter type of experiment a single rotational level in a vibrational manifold is initially populated and its population is monitored as a function of time. If backfilling into this initial level is neglected, as would be the case when the population of the initial level is much greater than the populations of other levels, then the time rate of change of the population in the initially populated level is

$$\frac{dN_i}{dt} = -\rho N_i \sum_{f \neq i} k_{i \to f} = -\rho N_i k_i^{(R)} \tag{4.6}$$

where $k_i^{(R)}$ is the bimolecular rate constant for removal of population out of this initial level and ρ is the density of the collision partner. This rate is the Maxwellian average [Eq. (3.31)] of the overall collisional removal cross section

$$\sigma^{(R)}(nk_a; E_c) = \sum_{n', k_a' \neq n, k_a} \sigma(nk_a \to n'k_a'; E_c) \tag{4.7}$$

In the depletion experiments of Sears, Hall, and their co-workers, [12, 14] we assume that all rotational levels are in thermal equilibrium and that level i is initially depleted. The time rate of change of population of this level in then governed by the master equation (3.4).

$$\frac{dN_i}{dt} = \rho \sum_{f \neq i} N_f k_{f \rightarrow i},\tag{4.8}$$

We have assumed that we can initially ignore collisional transitions out of the depleted level since the population of level i is very low at early times. If the rotational levels are in thermal equilibrium at temperature T, then

$$N_f = p_f N,\tag{4.9}$$

where N is the total population of the vibrational manifold under consideration and p_f is the Boltzmann probability for the population of level f. Substituting Eq. (4.9) into (4.8) and invoking detailed balance, [67] we obtain

$$\frac{dN_i}{dt} = \rho N \sum_{f \neq i} p_f k_{f \rightarrow i} = \rho N \sum_{f \neq i} p_i k_{i \rightarrow f} = \rho N_i k_i^{(R)}\tag{4.10}$$

Thus, the refilling rate constant is equal in magnitude to the removal rate constant one would measure when a single level is initially populated. In a complete analysis of the master equation for collisional rotational relaxation, it can in fact be shown, [48] without making any assumptions, that the removal and refilling rates defined in Eqs. (4.6) and (4.10) are equal. [48]

We have computed total removal cross sections for the $k_a = 1$ levels of $CH_2(\tilde{a})$
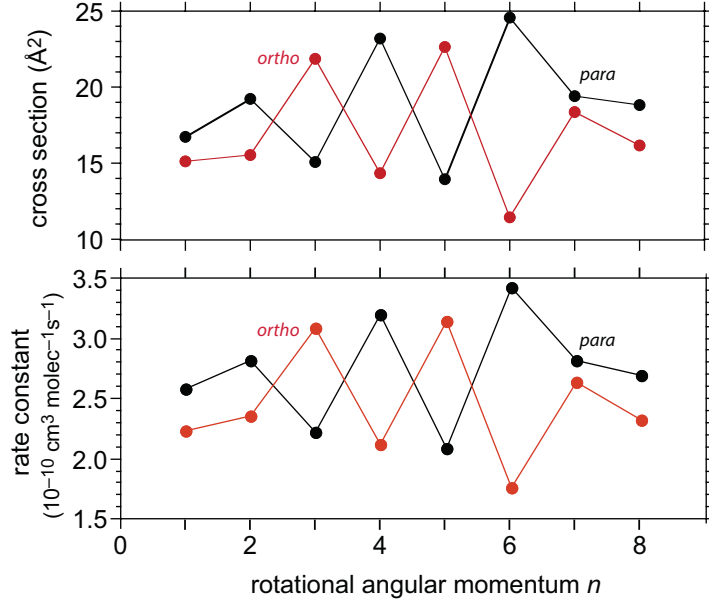
Figure 4.9: a) Rotationally inelastic total removal cross section for the lower $k_a = 1$ *ortho* and *para* rotational levels of $CH_2(\tilde{a})$ in collisions with He at a collision energy of 300 cm^{-1}. (b) Similar plot but for the rotationally inelastic total removal rates constants at 298 K.

in collisions with helium. With the computed energy-dependent total removal cross sections we determined, from Eq. (3.31), thermal rate constants at $T = 298$ K for loss of population of the $k_a = 1$ levels of $CH_2(\tilde{a})$ due to rotationally inelastic collisions with helium. These rate constants are presented in Fig. 4.9(b). The pronounced even-odd alternation is preserved, with the modulation depth almost unchanged from that of the cross sections at $E_c = 300$ cm^{-1}, which appear in Fig. 4.9(a).

4.5   Discussion

For $CH_2(\tilde{a})-$He collisions involving the $k_a = 1$ levels, Fig. 4.10 compares our computed rate constants for population removal by collision-induced rotational transitions with those measured experimentally by Hall, Sears, and their co-workers. [12, 14] We see that the computed rate constants for removal of population by rota-

tional transitions in collisions with helium are slightly larger than the experimental values, by $\sim 20\%$ for the $n \leq 6$ levels. However, the variation of the rate constants with n, in particular the enhanced rate constants for even n, is well reproduced in the calculations.
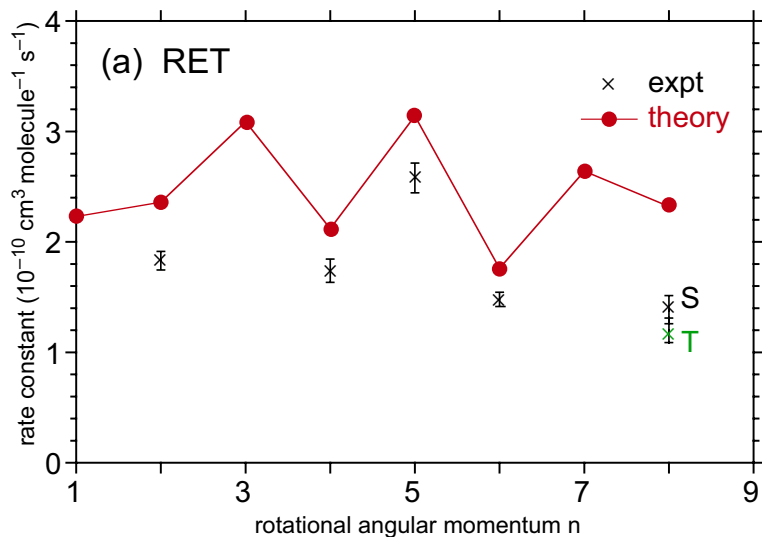
Figure 4.10: Rate constants for collisional removal by rotational transitions for $CH_2(\tilde{a})$ *ortho* $k_a = 1$ levels in collisions with helium. The theoretical values were computed in the present study, while the experimental values were taken from the investigation by Hall, Sears, and their co-workers [12, 14]. The $n = 8$ level of this manifold is known to be strongly perturbed by a vibration-rotation level of the $\tilde{X}$ state [10]. The labels S and T denote the experimentally observed rate constants for the two perturbed levels of predominantly singlet and triplet character, respectively (see, also, Chap. 6).

The $n = 8$ ($j = 8$ as well for the $\tilde{a}$ state) level is a special case, since it is strongly perturbed by a level in the $CH_2(\tilde{X}^3B_1)$ state. The triplet character of this state has been estimated [10, 39, 102] in several studies; on the basis of the hyperfine splitting, this state is estimated [102] to have $\sim 31\%$ triplet character, with a corresponding fraction of singlet character in the perturbing level [the $j = 8$ fine-structure component of the 9_{37} level in the $\tilde{X}^3B_1$ (020) vibrational level]. Hall, Sears, and their co-workers were able to measure total removal rate constants for

both of these levels. These are plotted in the same figure. It can be seen that these rate constants are approximately equal to each other and considerably smaller in magnitude than the computed rate constant for the $n = 8$ level.

Gelbart and Freed postulated that the presence of accidentally degenerate state can provide a "gateway" between two rotational manifolds of differing multiplicity. In previous work, Komissarov [12, 14] showed that in CH_2 a pair of mixed $\tilde{a}/\tilde{X}$ levels rapidly collisionally equilibrate their populations well before overall thermal relaxation. We are now involved in the theoretical study of collision-induced $\tilde{a} \rightarrow \tilde{X}$ transitions in CH_2, in particular in the study of how the presence of a spin-orbit induced electronic mixing effects rotational relaxation.

In this study, we have investigated rotationally inelastic collisions of $CH_2(\tilde{a})$ with the helium atom. We attribute the origin of the pronounced even-odd alternation in the magnitude of the total removal rate constants to an enhanced propensity for rotational energy transfer out of the odd-n *ortho*, and even-n *para,* levels. This is a direct consequence of the strong electronic anisotropy of the $CH_2(\tilde{a})$–He interaction, which arises because of the absence of electrons in the out-of-place non-bonding orbital on the C atom, of b_1 symmetry.

There remain small discrepancies between the magnitudes of the calculated and experimentally-measured rate constants. It is possible that these reflect the approximation, made in the determination of the potential energy surface, that the CH_2 in the $\tilde{a}$ state could be treated as a rigid molecule, with a fixed bond angle. In a more realistic description, we would calculate the interaction potential at several values of the CH_2 bending angle, and then average these values over the wavefunction

for the lowest bending vibration. This should be done. Also, as evidenced by the differences in the measured rate constants for the perturbed $n = 8$ levels, further investigation should be made of the effect of the $\tilde{X} \sim \tilde{a}$ perturbations on rotational relaxation.

Chapter 5: Rotationally and Vibrationally Inelastic Collisions of $CH_2(\tilde{X})$

in Collisions with Helium

This chapter describes an investigation of rotational and vibrational relaxation of CH_2 in its ground $\tilde{X}^3B_1$ electronic state, in collisions with the helium atom. We carried out *ab initio* calculations of the He–$CH_2(\tilde{X})$ PES, by treating the $CH_2(\tilde{X})$ molecule as semi-rigid, with a fixed bond length and a variable bending angle. We then average over the bending vibrational wave functions, as in Eq. (3.18), to obtain potential energy surfaces both for scattering within a particular vibrational manifold $(v' = v)$, or for collision induced transitions between rotational levels in different vibrational manifolds $(v' \neq v)$.

Since the $3a_1$ and $1b_1$ orbitals are both singly occupied in the $\tilde{X}$ state of CH_2, the electron density, and consequently, the He–CH_2 PES, is less anisotropic than in the $\tilde{a}$ state. As a result inelastic collisions will be less efficient in the $\tilde{X}$ state.

We report the state-to-state and total removal cross sections for rotationally inelastic transitions of $CH_2(\tilde{X})$ in a given bending vibrational mode, at a collision energy of 300 cm^{-1}. We have also studied the variation in cross sections with the degree of bending excitation. In particular we have compared the computed rate constant for the 9_{37} $(j = 8)$ rotational level in the (0,2,0) vibrational manifold of

the $\tilde{X}$ state, which is considered as the triplet component of a "gateway" pair (see Sec. 2.2.4) with experimental results from Komissarov, Hall and Sears. [12] Both the cross sections and the rate constants are smaller than those of the $\tilde{a}$ state.

In calculations in which several vibrational manifolds are included simultaneously, we show that probability of vibrational relaxation is less than 1% of that for rotational relaxation in a single vibrational level.

Part of this chapter, the investigation on the rotational relaxation of $CH_2(\tilde{X})$ in a single bending manifold, is reproduced from a published paper: L. Ma, P. J. Dagdigian and M. H. Alexander, *Theoretical investigation of rotationally inelastic collisions of* $CH_2(\tilde{X})$ *with helium*, J. Chem. Phys. **136**, 224306 (2012). [18] Here, we have modified the presentation of this article to include results on ro-vibrational relaxation between different bending manifolds.

In this, as well as in our first published paper on collisions of He with $CH_2(\tilde{a})$, [17] we did not explicitly include the spin. We used j to designate the rotational angular momentum of the CH_2 molecule. Here, we prefer to use j for the total molecular angular momentum (including the spin), and n for the rotational angular momentum of CH_2. This allows us, specifically in Chap. 6, to include spin, vector-coupling $\vec{S}$ with $\vec{n}$ to form $\vec{j}$.

5.1 Introduction and General Considerations

In last chapter we discussed rotationally inelastic collisions of He with the methylene radical, CH_2, in its first excited $\tilde{a}\,^1A_1$ state. [17] Here we extend this

work to collisions of CH_2 in its ground $\tilde{X}\,^3B_1$ state with He. The inelasticity of the ground state will be shown to be noticeably less than that of the excited state. We attribute this marked difference to a differing electron occupancy in the two states. The methylene radical is an important combustion intermediate. The reactivity of the $\tilde{a}$ state is known to be much higher than that of the ground $\tilde{X}$ state, [9,86] likely also a consequence of the same difference in electron occupancy.

We use the coordinates defined in Fig. 2.5. The CH_2 molecule lies in the xz-plane with the origin defined by the CH_2 center of mass. The body-frame z axis lies along the a inertial axis of the molecule. Thus, in collinear HCH the three atoms lie along the z axis. In this case the $2p_x$ and $2p_y$ orbitals on the C atom are degenerate. In analogy with the isoelectronic NH molecule, the ground state is $^3\Sigma^-$, with both of these orbitals singly occupied. The next state is the degenerate $^1\Delta$ state, with electron occupancies $2p_x^2$–$2p_y^2$ and singlet-coupled $2p_x2p_y$. The third valence state is $^1\Sigma^+$ which corresponds to a $2p_x^2+2p_y^2$ electron occupancy. When the molecule bends in the xz plane, (see Fig. 2.5), the $2p_x$ and $2p_y$ orbitals belong, respectively, to the a_1 and b_1 characters in C_{2v} symmetry. The first can combine with the positive linear combination of the two $1s$ orbitals on the H atoms to form the bonding $3a_1$ molecular orbital. The $2p_y$ orbital remains non-bonding, and is the lowest orbital of b_1 character. The lowest electronic state of bent CH_2 remains a triplet, with the $3a_1$ and $1b_1$ orbitals singly occupied.

Bending in the xz plane leads to a Renner-Teller [103] lifting of the degeneracy of the $^1\Delta$ state of the linear molecule. In the lower of these singlet states the $3a_1$ bonding orbital is doubly occupied, while the $1b_1$ orbital is empty. Because of this

hole in the $1b_1$ orbital, there is less electron density perpendicular to, as compared with in, the molecular plane. This is seen in Fig. 5.1, which compares electron-density contours for the two states of CH_2. An approaching atom will be sensitive to the Lewis amphoterism in the $\tilde{a}$ state with the result that the anisotropy of the interaction potential will be substantially greater for interaction of the atom with CH_2 in the $\tilde{a}^1A_1$ state as compared with interaction with the ground $\tilde{X}^3B_1$ state
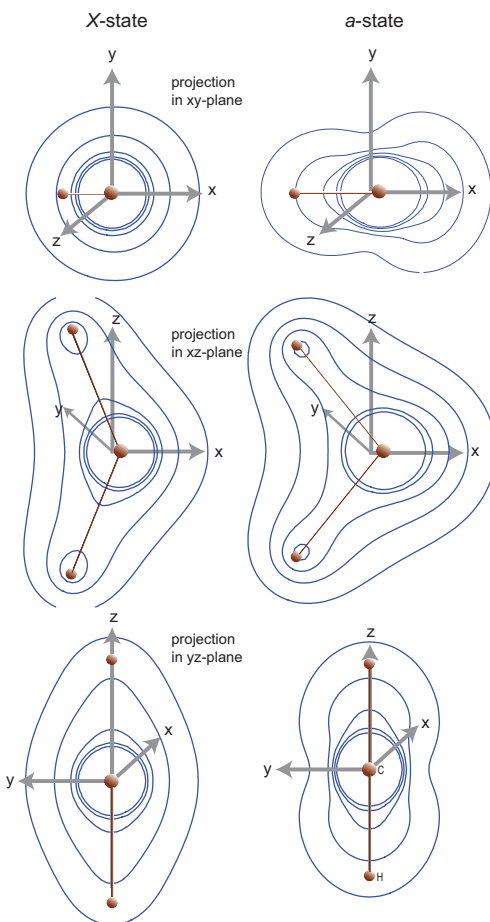
Figure 5.1: Electron-density contours projected onto the xy, xz, and yz planes for the CH_2 molecule in its ground $\tilde{X}^3B_1$ electronic state (left contours) and in its excited $\tilde{a}^1A_1$ electronic state (right contours). The geometry is defined in Fig. 2.5.

In linear geometry the $3a_1$ orbital is non-bonding ($2p_x$ on the C atom), but becomes strongly bonding in bent geometry. Consequently, by Walsh's rules [104]

the $\tilde{a}$ state, in which the $3a_1$ orbital is doubly occupied, is dramatically bent. By contrast, in the $\tilde{X}$ state the $3a_1$ orbital is only singly occupied, so that the barrier to linearity is much smaller. This is illustrated in the left-hand panel of Fig. 5.2, which compares the dependence on the HCH angle of the energy of these two states.

As can also be seen in Fig. 5.2, several of the lower vibrational levels of the $\tilde{X}$ state lie quite close in energy to the ground (0,0,0) vibrational level of the $\tilde{a}$ state. Experimental work has shown that accidental near degeneracies between rotational levels of these vibrational manifolds facilitate $\tilde{a} \rightarrow \tilde{X}$ collisional transfer. [10, 12, 15, 102]

In this chapter we report a theoretical investigation of collisional rotational relaxation within the $\tilde{X}$ state, a process which to date has not been studied experimentally. Our work is based on a new *ab initio* determination of the $CH_2(\tilde{X})$– He potential energy surface (PES), followed by quantum scattering calculations of inelastic cross sections and rate constants. We shall show that the much less anisotropic electron distribution in the $\tilde{X}$ state (Fig. 5.1) results in a much smaller degree of rotational inelasticity in collisions of CH_2 in this state.

In rotationally inelastic collisions of a polyatomic molecule, changes can occur both in the total rotational angular momentum, as well as its projection along the principal axis of the molecule. As we will show, the small barrier to linearity in the $\tilde{X}$ state affects significantly the collisional propensity toward changes in the projection quantum number.

Along with rotational relaxation we need, to be complete, to consider vibrational relaxation. In this chapter, we investigate the latter process by including the

interaction between rotational levels in different bending vibrational manifolds.

In Sec. 5.2, we summarize the *ab initio* determination of, and the subsequent fit to, the $CH_2(\tilde{X})$–He potential energy surface (PES). The inelastic scattering calculations based on this fitted PES are described in Sec. 5.3. State-to-state and total removal cross sections, as well as removal rate constants, are presented and compared in Sec. 5.4. Finally, in Sec. 5.5 we compare the predicted rotational inelasticity of CH_2 in the $\tilde{X}$ state with our earlier calculations on the CH_2–He systems and also with available experimental data from Sears, Hall, and co-workers [12, 14, 102].

5.2   Potential Energy Surface

The coordinate system used to describe the CH_2–He system is identical to that used in our earlier study of the $CH_2(\tilde{a})$–He system. [17] For a CH bond length fixed at its equilibrium value in the $\tilde{X}$ state [2.031 bohr (Ref. [31])], the dependence of the CH_2 energy on the HCH bond angle is shown in Fig. 5.2 for both the $\tilde{X}$ and $\tilde{a}$ states

The most significant difference between the $\tilde{a}$ and $\tilde{X}$ states of CH_2 is the dependence of the energy on the bending angle. The barrier to linearity in the $\tilde{a}$ state is so large ($> 10{,}000$ cm^{-1}) that the molecule can be treated as rigid with a fixed HCH angle of $\gamma = 101.77^o$ [32]. By contrast, the barrier to linearity in the $\tilde{X}$ state of CH_2 is dramatically smaller (~ 2000 cm^{-1}). Indeed, as seen in Fig. 5.2, even moderately excited vibrational levels in the $\tilde{X}$ state lie higher than the barrier. Consequently, to take into account the floppy nature of the CH_2 molecule in the
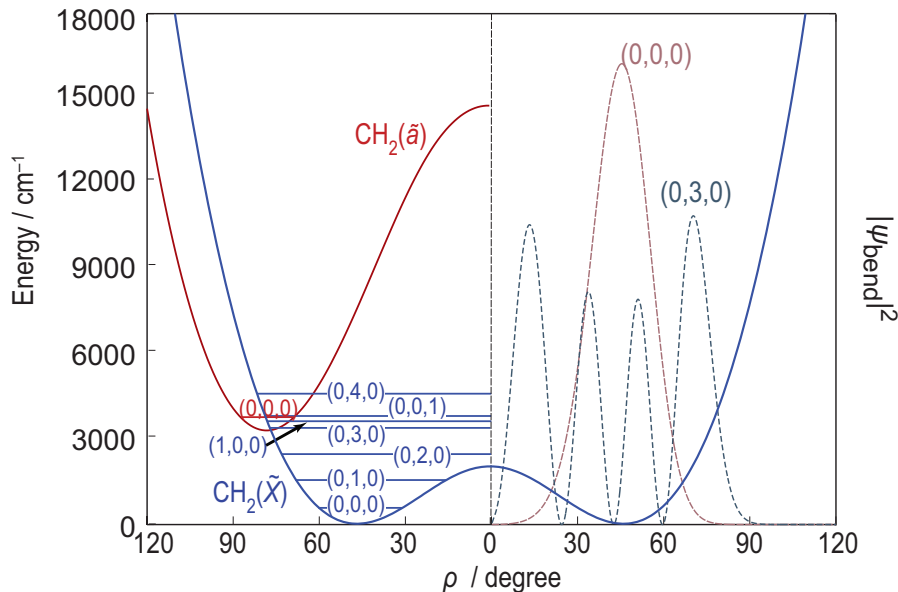
Figure 5.2: (Left-hand panel) The dependence on the bending angle of the energies of the $\tilde{a}\,^1A_1$ (red curve) and the $\tilde{X}\,^3B_1$ (blue curve) states of CH$_2$. In both cases the CH$_2$ bond lengths are frozen at their equilibrium values [2.031 bohr (Ref. [31])] for the $\tilde{X}$ state and [2.101 bohr (Ref. [32])] for the $\tilde{a}$ state. The horizontal lines indicate the positions of the vibrational levels, designated (v_a, v_b, v_s) where the subscripts a, b, and a denote the antisymmetric stretch, the bend, and the symmetric stretch modes, respectively. (Right-hand panel). The dependence of the bending probability (the square of the bending wavefunction) on the bending angle ρ is displayed for CH$_2(\tilde{X})$ vibrational states $(0,0,0)$ (red) and $(0,3,0)$ (blue). For consistency with the earlier work of Bunker, Hougen, and Johns [105] the abscissa ρ is the supplement of the bending angle γ.

$\tilde{X}$ state, we determined (as described below) the CH$_2(\tilde{X})-$He PES over a range of

bending angles and then averaged the PES over this angle, weighted by the square

of the wave function for this bending motion.

To determine the bending vibrational wave function for a bending triatomic

with fixed bond lengths, we adopted the method developed by Hougen, Bunker,

and Johns, [105] as implemented for symmetric triatomics by Bunker and Lands-

berg. [106] The expression for the wave function they derive is

$$\psi_b(\rho) = [I^0_{\rho\rho}]^{1/2}\phi_b(\rho) \tag{5.1}$$

where the function $\phi_b(\rho)$ satisfies the one-dimensional Schrodinger equation

$$-\frac{\hbar^2}{2I^0_{\rho\rho}}\frac{\partial^2}{\partial\rho^2}\phi_b(\rho) = \left\{\frac{\hbar^2}{2I^0_{\rho\rho}}f_1(\rho) + V_0(\rho) - E_b\right\}\phi_b(\rho) \tag{5.2}$$

The moment of inertia $I^0_{\rho\rho}$ is a function of ρ, the supplement of the bending angle $\rho = \pi - \gamma$, namely

$$I^0_{\rho\rho} = m_H r^2 \left[m_C + 2m_H \sin(\rho/2)\right]/2M \tag{5.3}$$

where r is the CH bond length, m_H and m_C are the H and C masses, respectively, and $M = m_C + 2m_H$. The function $f_1(\rho)$ in Eq. (5.2) depends on both $I^0_{\rho\rho}$ as well as the other moments of inertia. [105, 106]

We utilized a coupled-cluster *ab initio* calculation (described in the next paragraph) to determine the $CH_2(\tilde{X})$ bending potential $V_0(\rho)$. We then used Numerov integration to solve Eq. (5.2), matching the log-derivative of the inward and outward solutions. At small ρ (linear geometry) an explicit power-series solution of Eq. (5.2) was used to initiate the Numerov propagation, as described by Bunker and Landsberg. [106] The square of the bending wave functions for $v_b = 0$ and $v_b = 3$ are shown in the right-hand panel in Fig. 5.2. We see that for $\rho > 100°$ ($\gamma < 80°$), the probability densities approach zero very quickly.

The *ab initio* bending potentials of the $\tilde{a}$ and $\tilde{X}$ states of CH_2 shown in Fig. 5.2,

as well as the full $CH_2(\tilde{X})$–He PES, were determined by spin-restricted coupled cluster calculations with inclusion of single, double and (perturbatively) triple excitations [RCCSD(T)] [107, 108], carried out with the MOLPRO 2010.1 program suite. [51]. We use a correlation-consistent *avqz* basis [58] with the addition of a set of bond functions [59, 60] at the mid-point of the Jacobi vector $\vec{R}$ connecting the He atom with the center of mass of the CH_2 molecule. The CH bond length was fixed at 2.031 bohr [31]. To determine the dependence on γ of both the CH_2 bending potential energy curve and the CH_2–He PES, we performed calculations at bond angles γ ranging from 80° to 180° with a step size of 10°, as well as a few more points near linearity (179° and 179.9°). Since we assume fixed bond lengths, the present *ab initio* calculations provide no information on the dependence of the CH_2–He PES on the stretching modes.

Due to the dramatically increased expense engendered by the substantial grid in bending angles, we used *ab initio* grids in R and the two CH_2–He orientation angles that were coarser than in our previous study of the $CH_2(\tilde{a})$–He PES. [17] The complete grid was delineated by 19 values of R (3.5 to 10 in steps of 0.5, 11, 12, 13, 15, and 20 bohr), 4 values of the He–CH_2 polar angle θ (0, 30, 60, and 90°), and 13 values of the He–CH_2 azimuthal angle ϕ (0 to 180 in steps of 15°), and, as mentioned above, 13 values of the CH_2 bond angle γ. The total number of *ab initio* points was 12,844.

At each Jacobi distance R and CH_2 bond angle, the *ab initio* grid included $4 \times 13 = 52$ distinct points. The energies at these points were fitted by an expansion in spherical harmonics. Following our earlier work (see also Sec. 3.3 of this disserta-

tion), we expand around the principal axis of rotation [97], rather than around the C_2 symmetry axis. [63] We have [see also Eq. (4.1)]

$$V(R, \theta, \phi) = \sum_{\lambda,\mu} v_{\lambda\mu}(R)(1 + \delta_{\mu 0})^{-1} \left[Y_{\lambda\mu}(\theta, \phi) + (-1)^{\mu} Y_{\lambda,-\mu}(\theta, \phi) \right] . \qquad (5.4)$$

In last chapter for the $CH_2(\tilde{a})$–He PES we used 12 terms in the comparable expansion. For the $CH_2(\tilde{X})$, we increased this to 20 terms, making sure to eliminate all linear dependencies. [109]

The global minimum of the $CH_2(\tilde{X})$–He PES [averaged over the (0,3,0) bending vibrational wave function] occurs in a coplanar arrangement ($\phi = 0$) with the He atom located at $\theta = 16.3°$ and $R = 6.95$ bohr. The binding energy is 20.07 cm^{-1}, much less than the $CH_2(\tilde{a})$–He binding energy of 134 cm^{-1}. [17] Figure 5.3 compares the dependence on the orientation of the He atom for the $CH_2(\tilde{X})$–He and $CH_2(\tilde{a})$–He PES's, with the He–CH_2 distance held at the value corresponding to the global minima on the two PES's. The lower contour plot has been presented in last chapter (see Fig. 4.1). Additional slices of the $CH_2(\tilde{X})-$He PES are shown in Ref. [110].

As anticipated in the Introduction to this Chapter (5.1), when the He atom is displaced around the CH_2 molecule in a plane perpendicular to the symmetry axis ($\theta = 90°$, $\phi = 0 \rightarrow 180°$) the anisotropy of the CH_2–He PES is substantially greater for the $\tilde{a}$ state, where the out-of-plane $2p$ orbital on the C atom is unoccupied and the in-plane $2p$ orbital doubly occupied, as compared to that for the $\tilde{X}$ state, where these two orbitals are each singly occupied. This is seen in Fig. 5.4. Here, the two
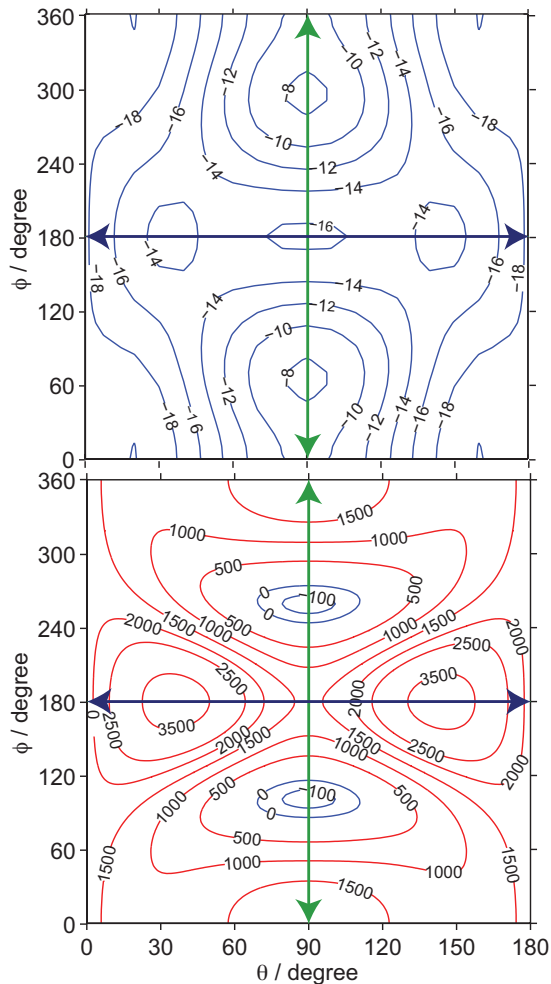
Figure 5.3: Contour plot (cm^{-1}) of the dependence on the orientation of the He atom of the $CH_2(\tilde{X})$–He (upper panel) and $CH_2(\tilde{a})$–He (lower panel) PES's. In both cases the CH_2–He distance is frozen at the value corresponding to the global minimum: $R = 6.95$ bohr for the $\tilde{X}$ state and $R = 4.58$ bohr for the $\tilde{a}$ state. Negative contours are indicated in blue, positive in red. The lower panel is reproduced from Fig. 4.1.

panels compare, for three different values of R, the variation in potential energy as the He atom moves in the xy plane $(\theta = 90°)$.

Figure 5.5 presents the dependence of the largest $v_{\lambda\mu}$ expansion coefficients on the He–$CH_2(\tilde{X})$ distance. At short distance, the largest anisotropic terms are $v_{31}(R)$ and $v_{20}(R)$. At very small R $(< 5$ bohr$)$, the $v_{20}(R)$ term dominates (not
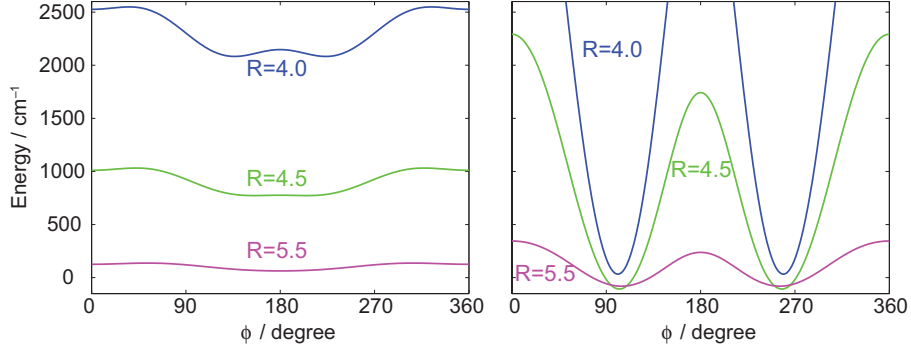
Figure 5.4: Dependence of potential energies on ϕ when $\theta = 90°$ (motion in xy plane) for the $CH_2(\tilde{X})$–He (left panel) and $CH_2(\tilde{a})$–He (right panel) systems.

shown). The $\lambda = 2$, $\mu = 0$ term in Eq. (5.4) depends on the angle θ only:

$$v_{20}(R, \theta, \phi) \sim 3\cos^2\theta - 1. \tag{5.5}$$

Since this term has no dependence on ϕ (because $\mu = 0$), we would expect the repulsive wall of the $CH_2(\tilde{X})$ PES to show little dependence on the motion of the He atom around the CH_2 molecule in the bisector plane (the xy plane in Fig. 4.1).

Figure 5.4 compares the angular dependence of the $CH_2(\tilde{X})$–He and the $CH_2(\tilde{a})$–He PES's for a He distance corresponding to the global minimum. In the former case, this occurs at rather large He distances, where the PES is globally attractive. As seen, for example, in Fig. 5.4, at shorter He distances the potential becomes repulsive. [111] The most repulsive regions on the $CH_2(\tilde{X})$–He PES occur for $\theta = 30°$ or $150°$ and $\phi = 180°$. These coordinates correspond to the location of the two hydrogen atoms. As stated in Eq. (4.3), the angular dependence of the $\lambda = 3$, $\mu = 1$ term has a maximum at these two sets of angular coordinates. Hence, the $v_{20}(R)$ term is responsible for the overall repulsion of the $CH_2(\tilde{X})$–He interaction while

the $v_{31}(R)$ term is responsible for the corrugation in the repulsive wall due to the presence of the two H atoms. In contrast with the $CH_2(\tilde{a})$–He PES, [17] the $v_{22}(R)$ term is quite small here.
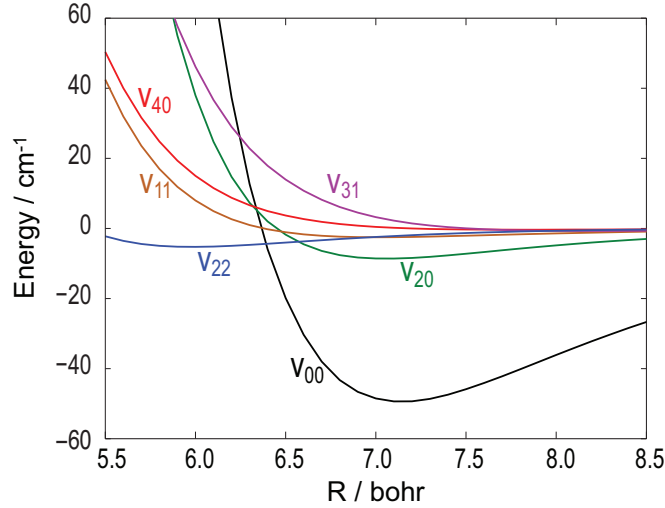
Figure 5.5: Dependence of the largest expansion coefficients $v_{\lambda\mu}$ on the atom-molecule distance R. Over this range the dominant anisotropic terms are $v_{31}(R)$ and $v_{20}(R)$.

The rotational wave functions for levels in different k_a manifolds differ in their dependence on the azimuthal angle ϕ (the rotation around the principal axis, see Fig. 4.1). Consequently, the important $v_{20}(R)$ term, which is independent of ϕ, will couple only levels within the same k_a manifold. Thus we might anticipate that the inelastic scattering will be dominated by $\Delta k_a = 0$ transitions. The second most important term, $v_{31}(R)$, will couple rotational levels in which the body-frame projection quantum number changes by ± 1. Since $\Delta k_a = +1$ corresponds to an endoergic transition, while $\Delta k_a = -1$ corresponds to an exoergic transition, we anticipate that the second most important inelastic transitions will correspond to those for which $\Delta k_a = -1$. [112]

To calculate the potential energy surfaces appropriate to the coupling between

rotational levels in two vibrational levels, we need the off-diagonal terms between the two bending wave functions [see Eq. (3.18)]

$$V_{v'_b, v_b}(R, \theta, \phi) = \langle v'_b(\gamma) | V(R, \theta, \phi, \gamma) | v_b(\gamma) \rangle, \tag{5.6}$$

where $|v_b(\gamma)\rangle$ is the bending wave function for the $(0,v_b,0)$ level. Again, we expand the interaction in 20 spherical harmonics terms, as shown in Eq. (5.4).
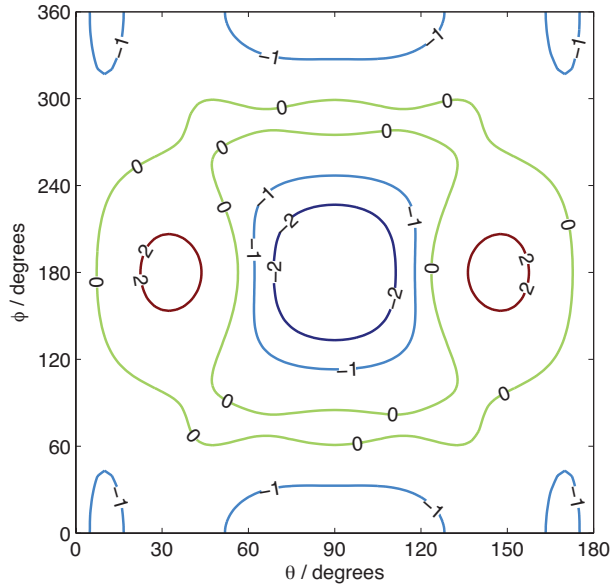
Figure 5.6: Contour plot of the interaction potential between the bending vibrational levels $(0,0,0)$ and $(0,1,0)$ of $CH_2(\tilde{X})$ with He at a $He-CH_2$ distance of 6.5 bohr.

Figure 5.6 shows the contour plot of the $\langle v'_b = 0 | v_b = 1 \rangle$ interaction potential at $R = 6.5$ bohr. Compared to the upper panel of Fig. 5.3, the vibrational coupling potential is considerably weaker and less anisotropic. Therefore, we expect much smaller cross sections for transitions between different $(v' \neq v)$ bending vibrational levels. The potential maximizes at $\phi = 180°$ and $\theta = 30°/150°$, corresponding to the locations of two hydrogens in the molecular plane. The minimum of the potential

91

is near $\phi = 90°$, also in the molecular plane. This corresponds to He approaching from the carbon side (see the middle right panel in Fig. 5.1).

In our studies (Chapter 4 and the earlier sections of the present Chapter) of purely rotational relaxation of CH_2 in the $\tilde{a}$ and $\tilde{X}$ states, we attempted to correlate the size of the inelastic cross sections to the relative magnitude of individual terms in the expansion of $V_{v'v}(R, \theta, \phi)$ PES [Eq. (5.6)]. For ro-vibrationally inelastic transitions, which are much smaller in magnitude, the direct coupling between different v, j levels will be masked by the much stronger couplings within the initial and final vibrational manifolds.

5.3 Scattering Calculations

Using the fitted $CH_2(\tilde{X})$–He PES, we carried out full close-coupling scattering calculations of inelastic cross sections for collisions of selected rotational levels of $CH_2(\tilde{X})$ in the $(0,v_b,0)$ bending vibrational manifolds ($v_b = 0 - 3$) with He. The HIBRIDON [45] suite of programs was utilized. In these calculations, only one bending level was included at a time, so that we obtain no information on transitions which are inelastic in the bending vibration. Collisions of rotational levels in the $(0,2,0)$ and $(0,3,0)$ manifolds were studied for a number of collision energies, but were limited to a single collision energy of 300 cm^{-1} for the $(0,0,0)$ and $(0,1,0)$ manifolds.

The $CH_2(\tilde{X})$ rotational energies are not at all well described by the standard rotational energy formulas because of the low barrier to linearity. Bunker and Jensen have developed a Morse oscillator-rotational bender internal dynamics Hamiltonian

(MORBID) to describe such semirigid molecules and have fit the parameters in this model to experimental measurements in order to compute $CH_2(\tilde{X})$ rovibrational energies. [19,113] We have used the energies determined by the MORBID code [114] for the asymptotic energies of the various channels in our scattering calculations. Jensen [115] has kindly provided us with these energies for rotational angular momenta [116] n up to 14. We extrapolated these energies to estimate energies of higher rotational levels.

The rotational basis in the scattering calculations included levels with energies as high as 2800 cm^{-1} and CH_2 rotational angular momentum n up to 30. Up to 300 values of the total CH_2He total angular momentum J were included at the higher collision energies. Because the effective A rotational constant is very large, especially for the (0,2,0) and (0,3,0) vibrational manifolds, [19, 113] the rotational wave functions are well approximated by symmetric top wave functions, and this was assumed for the calculation of the potential coupling of the rotational levels. Finally, since the spin and hyperfine splittings are small in CH_2, [37] the scattering calculations were carried out with a spin-free method.

5.4   Results

5.4.1   Rotational Energy Transfer

In discussing the results of the scattering calculations, we will probe how the magnitudes of the individual state-to-state cross sections are reflective of the features of the underlying PES and the relative positions of the individual vibration-rotation

93

levels of the CH_2 molecule. Figure 5.7 illustrates the energies of the rotational levels in the (0,0,0) and (0,3,0) vibrational manifolds.
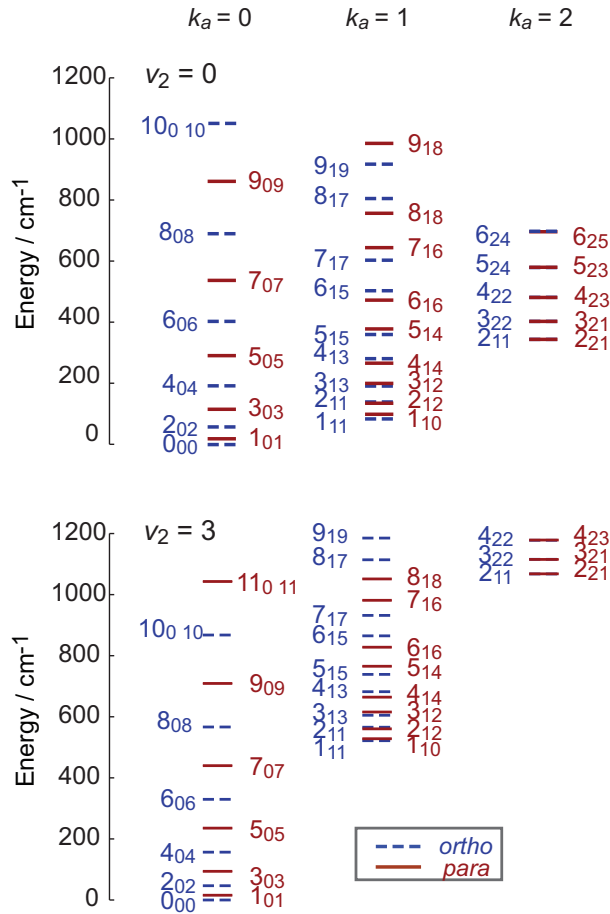
Figure 5.7: Lower rotational levels of the *ortho* (dashed blue) and *para* (solid red) nuclear spin modifications of $CH_2(\tilde{X})$ in the (0,0,0) and (0,3,0) vibrational manifolds. Each individual level is labelled $n_{k_a k_c}$, where n is the rotational angular momentum with k_a its (nominal) projection along the principal axis and k_c, its (nominal) projection along the prolate axis.

The *para* and *ortho* nuclear spin modifications differ in their nuclear permutation symmetries and will not be coupled by the interaction with ^{4}He, which has zero nuclear and electronic spin. For the $k_a = 0$ stack, the levels with even (odd) values of n are *ortho* (*para*). For the other k_a stacks, two levels exist for each n. For odd n the *ortho* level is lower, which reverses for even n. Compared to CH_2 in

the $\tilde{a}$ state (see Fig. 4.5), the energy splitting between the k_a stacks is considerably larger. This is a consequence of the more linear character of CH_2 in the $\tilde{X}$ state (see Fig. 5.2). Because the k_a stacks are farther apart in the (0,3,0) manifold, we would expect smaller cross sections for k_a changing transitions than was observed for collisions of $CH_2(\tilde{a})$ with He.

5.4.1.1 State-to-State Rotationally Inelastic Collision In The (0,2,0) and (0,3,0) Vibrational Manifolds

Bley and Temps [10] found that rotational levels associated with these two vibrational levels of the $\tilde{X}$ state play a significant role in relaxation of $CH_2(\tilde{a})$. Experimental work on relaxation of the CH_2 radical has been restricted so far to studies of the excited $\tilde{a}$ state in its lowest vibrational level (0,0,0). For these two reasons, we focus our attention here on the collisional relaxation of the 3rd and 4th bending vibrational levels ($v_b = 2$ and 3).

Figure 5.8 presents bar plots of the state-to-state inelastic cross sections for transitions from the $n = 4$ and 5 levels of the $k_a = 1$ stack for *ortho* and *para* $CH_2(\tilde{X})(0,3,0)$ at a collision energy of 300 cm^{-1}. [117] For transitions from both initial levels [$n = 4$ and 5, $k_a = 1$], the most probable transition is $\Delta k_a = 0, \Delta n = -2$ for both *ortho* and *para* CH_2. This is easily understood. As seen in Fig. 5.5 and in our discussion in Sec. 5.2, the $v_{20}(R)$ term is the largest anisotropic term at short range and the second largest term at large range. This term will couple directly transitions for which $\Delta k_a = 0$ and $\Delta n = \pm 2$. The transitions for which $\Delta n = +2$
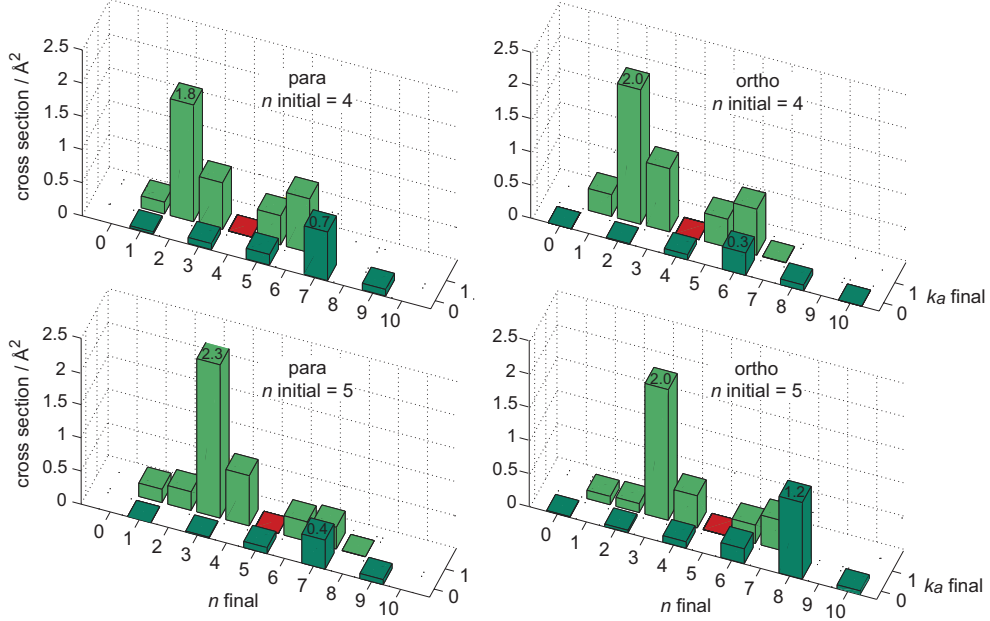
Figure 5.8: Bar plot of the cross sections for rotationally inelastic scattering of the $n = 4$ and 5, $k_a{=}1$ levels in the $(0,3,0)$ vibrational manifold of *para* (left figures) and *ortho* (right figures) $CH_2(\tilde{X})$ by collision with He at a collision energy of 300 cm^{-1}. Red marks the initial state.

are unfavored, relative to those for which $\Delta n = -2$, because of the larger density of translational phase space points for the exoergic ($\Delta n = -2$) process.

In collisions of He with CH_2 in the $\tilde{a}$ state, [17] we found that for k_a conserving transitions with $k_a = 1$, the cross sections showed a monotonic decrease as Δn increased, for all initial states investigated. In contrast, in collisions of the $\tilde{X}$ state we do not observe a similar monotonic decrease.

Transitions in which the projection quantum number k_a changes can be directly coupled only by terms in the expansion of the CH_2–He PES for which $\mu \neq 0$. Of these, the largest is the $v_{31}(R)$ term (see Fig. 5.5). The only nuclear permutation allowed transitions that can be directly coupled by this term are those with $\Delta n = \pm 1$ or ± 3. For the $k_a = 1 \rightarrow k_a = 0$ transitions with $n = 4$ or 5 ($\Delta k_a = -1$), all

the computed cross sections are small with the exception of those for the $\Delta n = +3$ transitions from the $n = 4$ level of the *para* and the $n = 5$ level of the *ortho* isotopomers. The $\Delta n = \pm 3$ selection rule for direct coupling through the $v_{31}(R)$ term would allow transitions from $n = 4, k_a = 1$ to $n = 7, k_a = 0$ and $n = 5, k_a = 1$ to $n = 8, k_a = 0$. Since the $n = 7$ level in the $k_a = 0$ manifold exists only for *para*-CH$_2$ and the $n = 8$ level, only for *ortho* CH$_2$, we conclude that the $v_{31}(R)$ term will couple directly the $4 \to 7, \Delta k_a = -1$ transition in *para* CH$_2$ and the $5 \to 8, \Delta k_a = -1$ transition in *ortho* CH$_2$. These are exactly the strong $\Delta k_a = -1$ transitions which appear in Fig. 5.8.

5.4.1.2 Total Cross Sections and Rate Constants

A more averaged measure of the degree of inelasticity is the total removal cross section, which is the sum, over all energetically accessible final states, of the rotational-state resolved cross sections, namely

$$\sigma_{nk_a}^{(R)}(E_c) = \sum_{n',k_a'} \sigma_{nk_a,n'k_a'}(E_c)$$

Total removal cross sections are listed in Table 5.1 for collisions with CH$_2(\tilde{X})$ in the $n = 4$ and 5, $k_a = 1$ rotational levels of the (0,3,0) vibrational manifold. We also list the average change in the rotational quantum number n and its projection k_a, weighted by the state-to-state cross sections [see Eq. (4.5)].

When we compare these with the identical quantities for relaxation of CH$_2$ in the $\tilde{a}$ state (see Table 4.1), we observe that all three measures of the inelasticity

97

Table 5.1: Total removal cross sections out of the $n = 4$ and 5, $k_a = 1$ levels in the (0,3,0) vibrational state of *para* and *ortho* $CH_2(\tilde{X})$ by collision with He at a collision energy of 300 cm^{-1}.

| | ortho | | para | |
Quantity	$n = 4$	$n = 5$	$n = 4$	$n = 5$
$\sigma^{(R)}/\text{Å}^2$	4.9	5.0	5.0	4.8
$< \|\Delta n\| >$	1.79	2.14	1.97	1.92
$< \|\Delta k_a\| >$	0.10	0.31	0.22	0.13

are substantially smaller for collisions of He with CH_2 in its ground ($\tilde{X}$) state. Because of the differing electron occupancy, the electronic anisotropy of the $\tilde{a}$ state is greater (see Fig. 5.1). Consequently, as suggested in the Introduction, the rotational inelasticity is smaller.

The total removal cross sections are ~ 5 Å^2, roughly 3 times smaller than the total removal cross sections for collisions of He with $CH_2(\tilde{a})$. Again, this is a manifestation of the smaller electronic anisotropy in the $\tilde{X}$ state of CH_2. The average changes in n and k_a are also small. The change in n is slightly larger than observed for collisions of He with CH_2 in the excited $\tilde{a}$ state, while the change in k_a is slightly smaller. The latter effect is probably a result of the larger energy splitting between the $k_a = 0$ and $k_a = 1$ stacks in the $\tilde{X}$ state, due to the more linear character of this state.

There is very little (if any) variation with n of these total removal cross sections, contrary to what we observed earlier in collisions of He with $CH_2(\tilde{a})$. There is
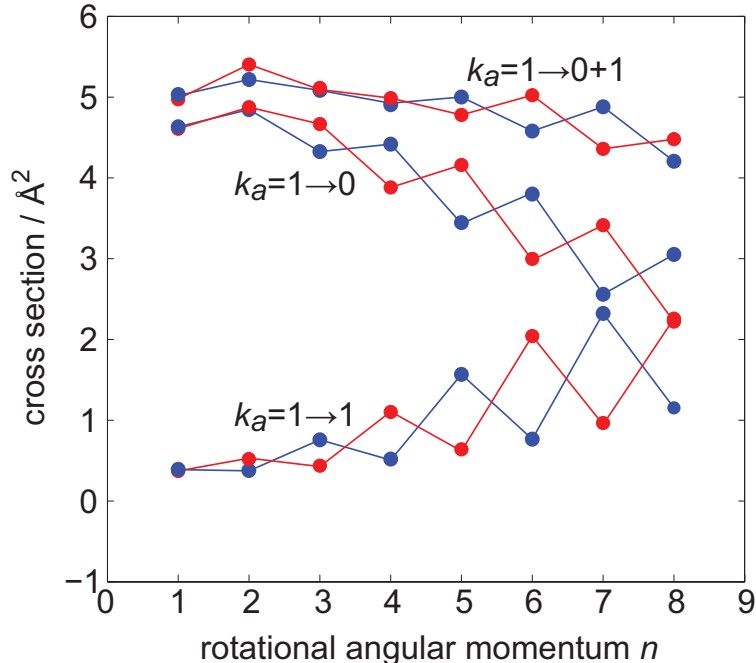
Figure 5.9: Total removal cross sections for $CH_2(\tilde{X})$–He collisions at $300\ cm^{-1}$ for molecules in different $k_a = 1$ states (*para* in red and *ortho* in blue) in the $(0,3,0)$ vibrational manifold. The highest group is for transitions from $k_a = 1$ stack to both $k_a = 0$ and 1 levels. The upper set of curves represents the total removal cross section for transitions into both the $k_a = 0$ and $k_a = 1$ stacks.

a much more pronounced variation with n of the removal cross sections resolved by final k_a [but still less than the variation observed for collisions of He with $CH_2(\tilde{a})$]. Note that the modulation depth of these alternations is significantly reduced compared to what we observed for collisions of He with $CH_2(\tilde{a})$. Finally, we observe that the alternation in the $k_a = 1 \rightarrow 0$ cross sections is canceled by the alternation in the $k_a = 1 \rightarrow 1$ cross sections.

5.4.1.3   Variation with Bending Level

Figure 5.2 reveals that with a smaller degree of vibrational excitation in the bending mode, the CH_2 molecule in the $\tilde{X}$ state becomes more confined to bent

Table 5.2: Energy gaps for $\Delta n = -1$ and -2 transitions out of the *ortho*-CH$_2(\tilde{X})$ n = 4, $k_a = 1$ (4_{13}) level in the (v$_s$, v$_b$, v$_a$=0,0,0), (0,1,0), (0,2,0) and (0,3,0) vibrational manifolds.[a]

	transitions	final level	(0,0,0)	(0,1,0)	(0,2,0)	(0,3,0)
$\Delta k_a = 0$	$\Delta n = -2$	2_{11}	−113.7	−113.5	−114.4	−116.5
	$\Delta n = -1$	3_{13}	−72.1	−72.4	−74.1	−77.3
$\Delta k_a = -1$	$\Delta n = 0$	4_{04}	−69.8	−162.1	−361.2	−525.5
	$\Delta n = 2$	6_{06}	−100.8	7.3	191.6	352.6

[a] A negative value for the energy gap indicates that the final level lies lower in energy than the 4_{13} level.

geometry. In this case, the effective A rotational constant becomes smaller, and the k_a stacks become closer in energy as the bending quantum number decreases. This is revealed clearly in Table 5.2, which lists the values of the energy gaps for $\Delta n = -1(-2)$ transitions for the CH$_2(\tilde{X})$ molecule initially in the 4_{13} level (see Fig. 5.7). The energy gaps for $k_a = 1 \rightarrow 0$ transitions decrease dramatically, while the energy gaps within the $k_a = 1$ manifold are little changed.

In Fig. 5.10, we compare the state-to-state inelastic cross sections out of $n = 4$, $k_a = 1$ (4_{13}) level of *ortho* CH$_2(\tilde{X})$ in the (0,0,0), (0,1,0), and (0,2,0) vibrational manifolds at a collision energy of 300 cm^{-1}. These plots should be juxtaposed with the similar plot for the (0,3,0) vibrational manifold, which is the upper right panel of Fig. 5.8.

We observe in Figs. 5.8 and 5.10 that for the transitions within the $k_a = 1$ manifold ($\Delta k_a = 0$) the overall magnitude increases as v_b increases, although the
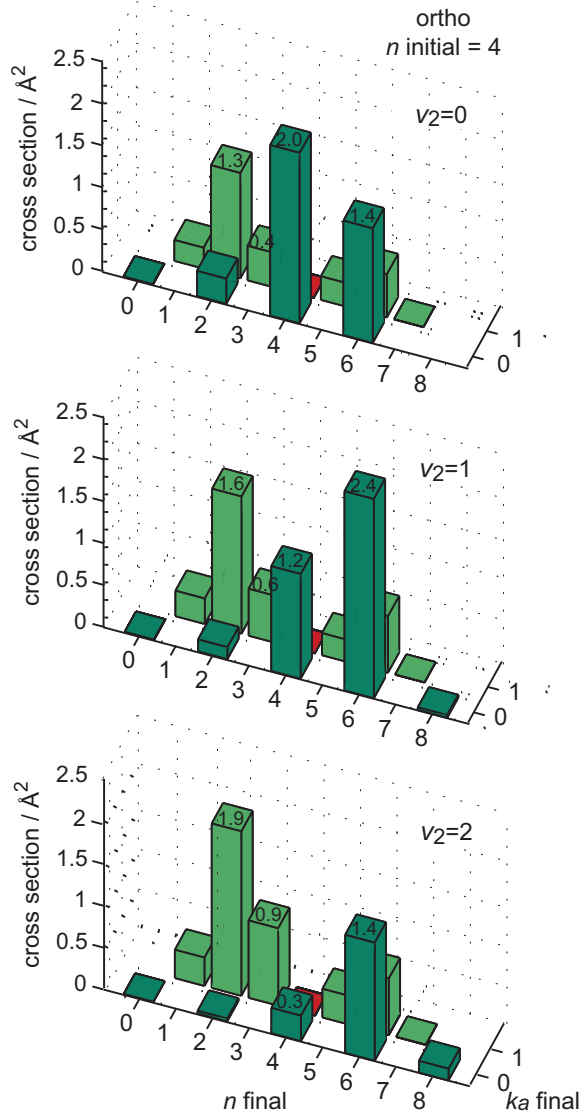
Figure 5.10: Bar plot of cross sections for rotationally inelastic scattering from $n = 4$, $k_a = 1$ levels of the *ortho* $CH_2(\tilde{X})$ to final levels with n up to 8 in $(0,0,0)$, $(0,1,0)$, and $(0,2,0)$ vibrational manifolds (from top to bottom) by collision with He at a collision energy of 300 cm^{-1}. Red marks the initial level.

relative dependence on the final rotational quantum number is little changed. By contrast, overall the $k_a = 1 \to 0$ cross sections decrease as as v_b increases. This behavior is a reflection of the changing $k_a = 0 \to 1$ energy gap, whose magnitude increases dramatically as v_b increases (see Table 5.2).

As shown in Table 5.3, overall, the total removal cross sections for collisions

of He with $CH_2(\tilde{X})$ in the $n = 4, k_a = 1$ rotational level of the $(0, v_b, 0)$ vibrational manifold gradually decrease as v_b increases for the *ortho* states but increase for the *para* states. This differing dependence on v_b is likely a subtle consequence of energy gaps between the $k_a = 1$ and $k_a = 0$ rotational levels for these two nuclear spin modifications. Most noticeably, the average collisional change in the projection quantum number decreases dramatically as the vibrational quantum number increases. This is a direct consequence of the increasing energy gap between the $k_a = 0$ and $k_a = 1$ rotational manifolds. In particular, we see in Table 5.2 that the energy gap for the $n_a = 4, k_a = 1 \rightarrow 6, 0$ transition is accidentally very small in the (0,1,0) vibrational manifold. The corresponding cross section is much larger than for the identical transition in the other bending vibrational manifolds.

We also see in Fig. 5.14 that the total removal cross sections for the $\tilde{a}$ state are much larger than those for the $\tilde{X}$ state. This is consistent with the more pronounced electronic anisotropy in the $\tilde{a}$ state (see Fig. 5.1) and the resulting larger anisotropy in the $CH_2(\tilde{a})$–He PES.

Table 5.3: Overall inelastic cross sections for transitions out of the $n = 4$, $k_a = 1$ level of *ortho* and *para* $CH_2(\tilde{X})$, and out of the $j = 4$, $k_a = 1$ level of the (0,0,0) manifold of $CH_2(\tilde{a})$ by collision with He at a collision energy of 300 cm^{-1}.[a]

Quantity	$\tilde{a}(0,0,0)$[a]	$\tilde{X}$			
		(0,0,0)	(0,1,0)	(0,2,0)	(0,3,0)
		ortho $n=4$			
$\sigma^R/\text{Å}^2$	14.2	7.7	7.5	6.1	4.9
$<\|\Delta n\|>$	1.1	1.32	1.59	1.80	1.79
$<\|\Delta k_a\|>$	0.71	0.65	0.54	0.31	0.10
		para $n=4$			
$\sigma^R/\text{Å}^2$	22.9	3.5	2.8	5.9	5.0
$<\|\Delta n\|>$	1.1	1.62	1.81	2.07	1.97
$<\|\Delta k_a\|>$	0.73	0.80	0.75	0.39	0.22

[a] In the singlet $\tilde{a}$ state, the total molecular rotational angular momentum j is equal to the rotational angular momentum of the nuclei n. The comparison here is with relaxation out of the $j = 4$, $k_a = 1$ rotational level of CH_2 in the (0,0,0) vibrational manifold of the $\tilde{a}$ state.

5.4.2 Vibrational Energy Transfer

5.4.2.1 State-to-State Ro-vibrational Transitions

In principle, one can expand the dependence on the bending coordinate of the interaction potential [Eq. (3.8)] as a power series

$$
\begin{aligned}
V(\mathbf{Q}) \equiv V(R, \theta, \phi, q_b) \approx{}& V(R, \theta, \phi, q_b^{(e)}) + \left.\frac{\partial V(R, \theta, \phi, q_b)}{\partial q_b}\right|_{q_b^{(e)}} (q_b - q_b^{(e)}) \\
& + \left.\frac{\partial^2 V(R, \theta, \phi, q_b)}{\partial q_b^2}\right|_{q_b^{(e)}} (q_b - q_b^{(e)})^2 + \cdots
\end{aligned}
\tag{5.7}
$$

where q_b is the bending coordinate and $q_b^{(e)}$ its value at equilibrium. Thus

$$
\langle v'| V(\mathbf{Q}) |v\rangle \approx V(R, \theta, \phi, q_b^{(e)})\langle v'|v\rangle + \partial V_{q_b^{(e)}} \langle v'| (q_b - q_b^{(e)}) |v\rangle + \partial^2 V_{q_b^{(e)}} \langle v'| (q_b - q_b^{(e)})^2 |v\rangle
\tag{5.8}
$$

Here we have used a obvious notational simplification for the derivatives evaluated at $q_b^{(e)}$.

Because of the vibrational wave functions are orthogonal, the first term vanishes. In the harmonic limit, the second term also vanishes when $v' \neq v \pm 1$. Further, we expect the second derivative term to be smaller than the first derivative term, since the dependence on q_b will probably be slowly varying. Thus, we anticipate that the $v \rightarrow v \pm 1$ coupling will be stronger than that for $v \rightarrow v \pm 2$. In other words, we anticipate the strongest transitions will occur for $\Delta v = \pm 1$. Also, again in the harmonic limit, the $\langle v|(r - r_e)|v + 1\rangle$ matrix element scales linearly with v, so that we anticipate the $v_b = 2 \rightarrow 1$ cross sections will be larger than those for

$v_b = 1 \rightarrow 0$.

Figure 5.11 presents a confirmation of these qualitative predictions. Here we show bar plots of state-to-state cross sections for transitions from the 5_{15} ($n = 5, k_a = 1$) rotational level in various bending vibrational manifolds to rotational levels in a nearby bending vibrational manifold, at a collisional energy of 300 cm^{-1}. The $v_b = 2 \rightarrow 0$ state-to-state cross sections (top panel) are extremely small ($< 1 \times 10^{-4}$Å^2). The two lower panels show rotationally-resolved $v_b = 1 \rightarrow 0$ and $v_b = 2 \rightarrow 1$ cross sections, again out of the 5_{15} level in both cases. These $\Delta v = -1$ cross sections are roughly two orders of magnitude larger than the $\Delta v = -2$ cross sections shown in the top panel, but still of more than two orders of magnitude smaller than the rotational inelastic cross sections within a vibrational manifold as shown in Fig. 5.8. Finally, we see that the $v_b = 2 \rightarrow 1$ cross sections are roughly twice as large as those for the $v_b = 1 \rightarrow 0$ transition.

The strongest transitions out of the 5_{15} level for both $v_b = 1 \rightarrow 0$ and for $v_b = 2 \rightarrow 1$ are those with $\Delta n = 4$ and $\Delta k_a = 2$, as shown in the middle and bottom panels of Fig. 5.11. However, as we mentioned earlier, since the interaction between the vibrational levels is very weak, compared to the much larger pure rotational couplings, it is impossible to attribute the strength of this transition to a particular term in the expansion of the $v_{\lambda\mu}$ expansion term.

In Fig. 5.12 we plot the dependence of the $v_b = 1 \rightarrow 0$ cross sections on the energy gap. Although, overall, the largest cross sections have relatively small energy gaps, this is clearly not the only determinant factor. The propensity for ro-vibrational transitions must be a subtle function of the energy gap, the strength of
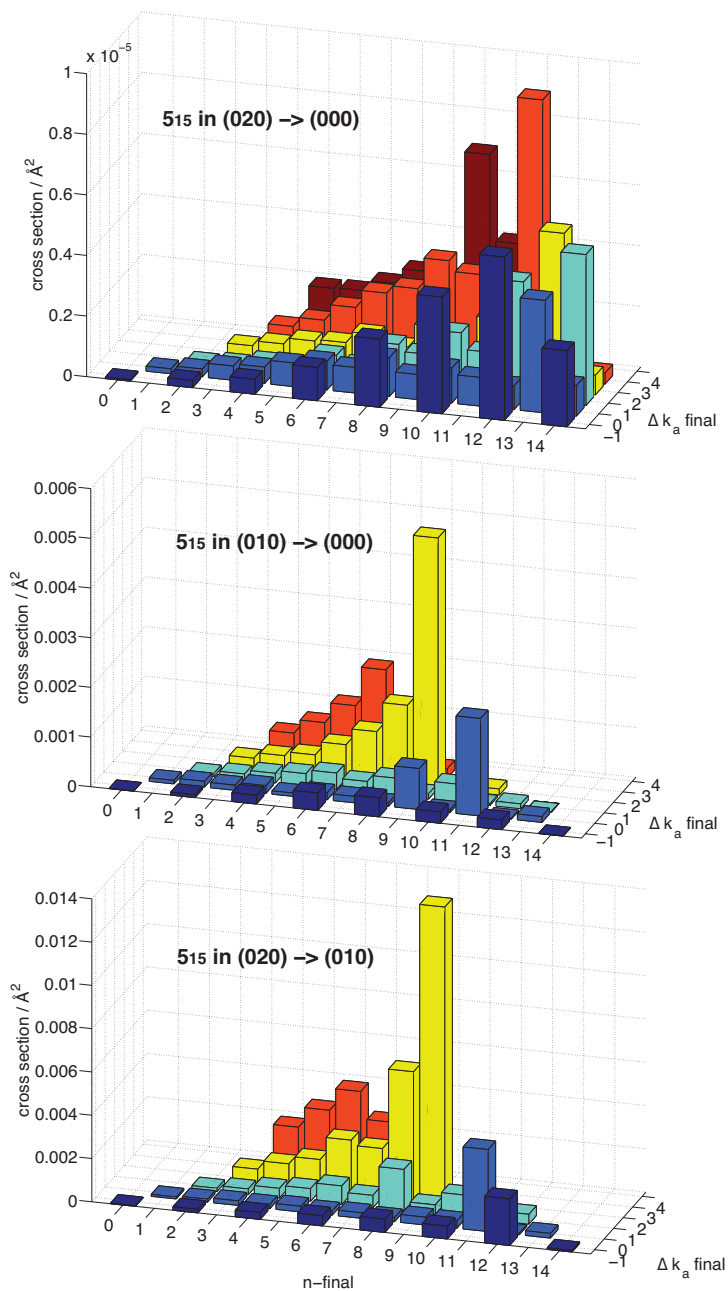
Figure 5.11: Bar plot of cross sections for vibrationally-inelastic collisions of He with o-CH$_2(\tilde{X})$ in the 5_{15} rotational level at E_{col}=300 cm^{-1}. (Top Panel) $5_{15}(0,2,0)$ to levels in $(0,0,0)$; (Middle Panel) $5_{15}(0,1,0)$ to levels in $(0,0,0)$; (Bottom Panel) $5_{15}(0,2,0)$ to levels in $(0,1,0)$.

the coupling, and the unseen influence of the much larger propensities for transitions

within both the initial and the final rotational levels.
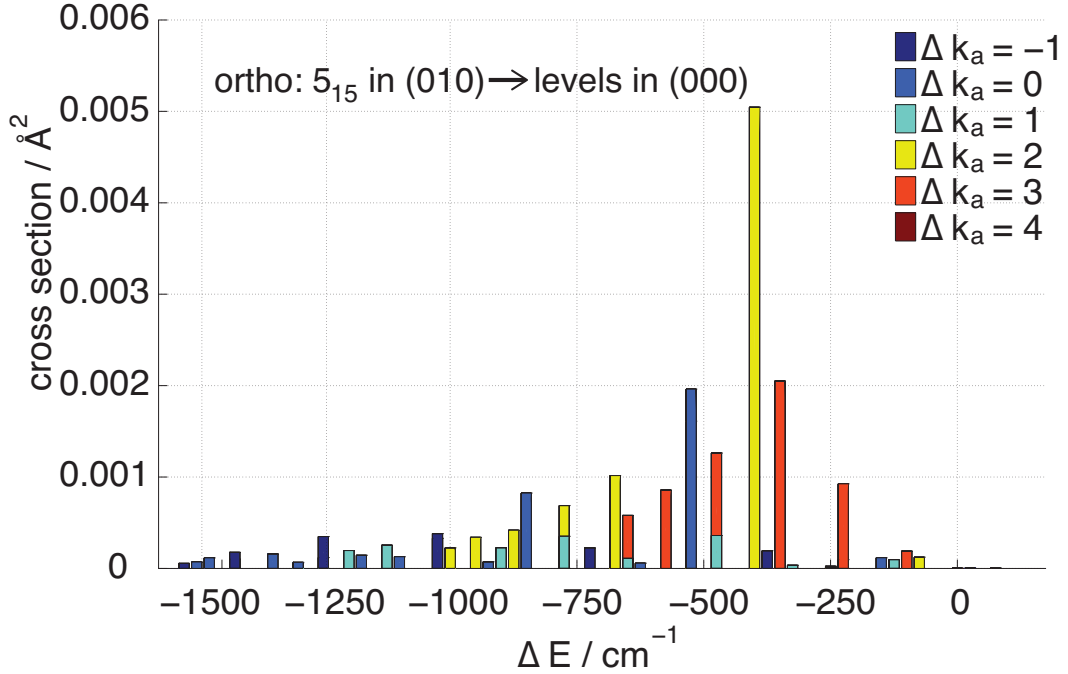
Figure 5.12: Bar plot of cross sections against the energy gap, for transitions from 5_{15} in (0,1,0) vibrational level to rotational levels in (0,0,0) vibrational level of $CH_2(\tilde{X})$, by collision with He at a collision energy of 300 cm^{-1}.

5.4.2.2   Overall Vibrational Relaxation

In addition, we computed the total vibrational relaxation cross sections out of the 5_{15} level in various vibrational levels to nearby vibrational levels, namely

$$\sigma_{vib}(5_{15}, v_b \to v_b') = \sum_{n',k_a'} \sigma_{5_{15}(0,v_b,0) \to n'k_a'(0,v_b',0)}, \qquad (5.9)$$

as well as the average values of $|\Delta n|$ and $|\Delta k_a|$, defined earlier in Eq. (4.5). The results are listed in Table 5.4. The first column of data, which was already included in Table 5.1, refers to pure rotational relaxation and is included here from comparison with the data for ro-vibrational transitions in columns 3, 4, and 5. The largest σ_{vib}, for (0,2,0)→(0,1,0) relaxation, is about 1% in magnitude of the total removal cross

Table 5.4: Total vibrational relaxation cross sections out of the 5_{15} level in various bending vibrational levels to a nearby vibrational level of *ortho* $CH_2(\tilde{X})$ by collision with He at a collision energy of 300 cm^{-1}.

Initial Level /	(0,3,0)	(0,2,0)	(0,1,0)	(0,2,0)
Final Level	(0,3,0)	(0,1,0)	(0,0,0)	(0,0,0)
$\sigma_{vib}/\text{Å}^2$	5.0	5.9×10^{-2}	2.3×10^{-2}	1.2×10^{-4}
$< |\Delta n| >$	2.14	2.92	2.93	5.09
$< |\Delta k_a| >$	0.31	1.80	1.78	2.17

section within the (0,3,0) vibrational level. Both $|\Delta n|$ and $|\Delta k_a|$ are larger due to the large number of available final states in a lower vibrational level.

In Fig. 5.13 we plot the total cross sections for other initial rotational levels:

$$\sigma_{vib}(n_{k_a k_c}, v_b \to v_b') = \sum_{n',k_a'} \sigma_{n_{k_a k_c}(0,v_b,0) \to n'k_a'(0,v_b',0)}. \tag{5.10}$$

The magnitudes of the vibrational relaxation cross sections are all comparable in magnitude to those shown in Fig. 5.11, namely $\sim 10^{-4}$, 10^{-2} and 10^{-2} Å^2 for, respectively, the $v_b = 2 \to 0$, $1 \to 0$ and $2 \to 1$ transitions. In general, the cross sections out of the $k_a = 0$ levels are slightly larger than those out of levels with $k_a > 0$.

5.5 Discussion

In last chapter, we compared the calculated total removal rate constants out of the $k_a = 1$ levels of *ortho* $CH_2(\tilde{a})$ with the corresponding values measured by
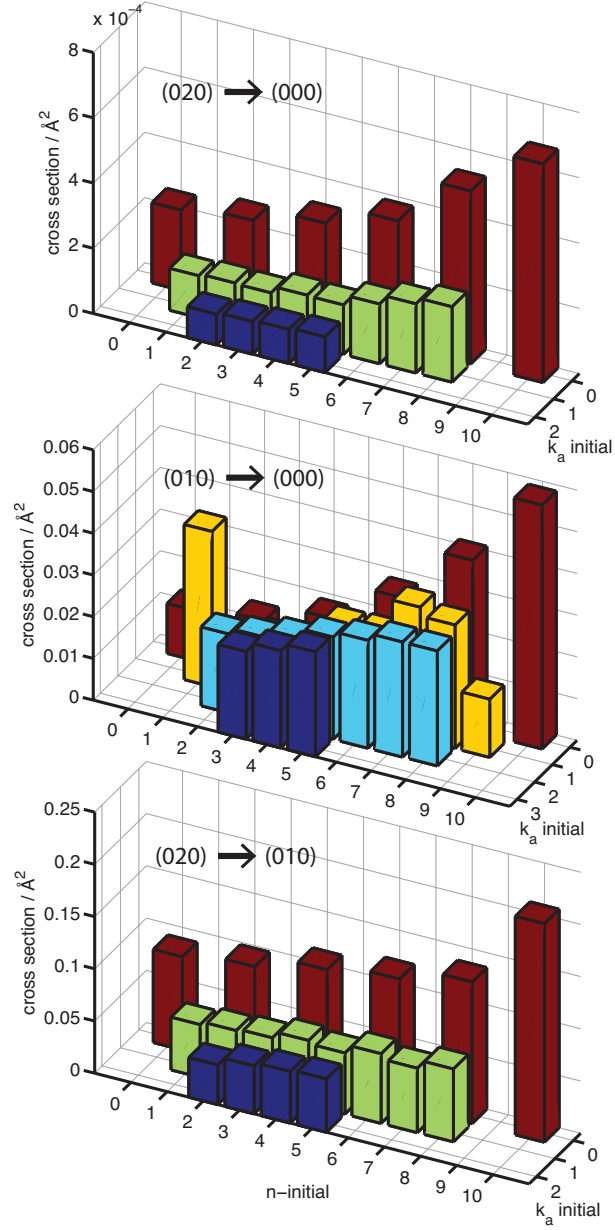
Figure 5.13: Bar plot of total vibrational relaxation cross sections for transitions out of various initial rotational levels of *ortho* $CH_2(\tilde{X})$, by collision with He at a collision energy of 300 cm^{-1}.

Hall, Sears, and co-workers. This comparison is reproduced here in Fig. 5.14. The calculated rate constants are about 20% higher than experiment, except for the $n = 8$ level, [118] where the experimental values are reduced by ∼70%.

We plot in blue the relaxation rate constants out of the $n = 1-8$, $k_a = 1$ *ortho*
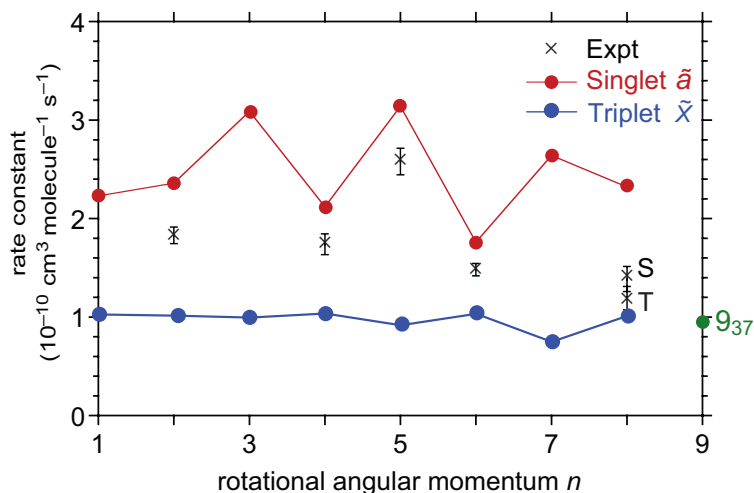
Figure 5.14: Theoretical and experimental (Ref. [14]) total removal rate constants for the $k_a = 1$ levels of *ortho* CH_2 by collision with He at room temperature. (Note that experimental results are not available for all the initial rotational levels). The red points, corresponding to relaxation of the $\tilde{a}$ state, are from calculations reported in Chap.4, while the blue points, corresponding to relaxation of the $\tilde{X}$ state, are from the calculations reported here. Also shown is the calculated relaxation rate of the $n = 9$, $k_a = 3$ level of the (0,2,0) manifold. One spin component of this $\tilde{X}$ level is mixed with the $j = 8, k_a = 1$ level of the (0,0,0) manifold of the $\tilde{a}$ state. The experimentally observed (Ref. [14]) relaxation rates of the two mixed levels are shown by the points marked "S" (nominally singlet) and "T" (nominally triplet).

rotational levels in the $CH_2(\tilde{X})$ (0,3,0) vibrational manifold. One spin component of the $n = 9$, $k_a = 3$ level of the $CH_2(\tilde{X})$ (0,2,0) vibrational manifold is mixed strongly with the $n = 8$, $k_a = 1$ level of the $CH_2(\tilde{a})$ (0,0,0) manifold. [10] The experimentally determined relaxation rate of the two mixed states are labelled in the figure "S" (primarily singlet but with $\sim 25\%$ triplet character) and "T" (primarily triplet, but with $\sim 25\%$ singlet character). Because the $\tilde{X}$-state component in both mixed states has a much smaller relaxation rate, the overall relaxation of both mixed states will be substantially slower than that of levels of pure $\tilde{a}$ electronic character.

In the present chapter we have not considered any mixing between the $\tilde{X}$ and $\tilde{a}$ states. This will be explored later in Chap. 6. However, to give some credence to this discussion and comparison with experiment, we also plot in Fig. 5.14 the calculated rate constant for the overall relaxation of the pure $\tilde{X}$-state 9_{37} rotational level of the (0,2,0) bending manifold. As we might anticipate, this relaxation rate lies slightly below (but close to) the experimentally measured rate for the $n = 8$ levels of the $\tilde{a}$ state.

We have also investigated the dependence on final rotational level of cross sections for rotationally inelastic collisions of $CH_2(\tilde{X})$, in particular in the (0,2,0) and (0,3,0) bending vibrational manifolds. We observe an alternation of the cross sections with the parity of the initial rotational quantum number, but much less pronounced than observed earlier in relaxation of the $\tilde{a}$ state (see Chap. 4). This reduction in the degree of alternation, as well as in the magnitude of the inelastic cross sections, is due to the reduced degree of electronic anisotropy in the $\tilde{X}$ state, where both the $3a_1$ and $1b_1$ orbitals are singly occupied, as compared to the $\tilde{a}$ state, in which the $1b_1$ orbital is unoccupied.

The barrier to linearity in the $\tilde{X}$ state of CH_2 is not as large as that in the $\tilde{a}$ state, so that with a modest degree of bending excitation the molecule significantly explores near-linear geometries. To take this into account when determining the potential energy surface, we performed *ab initio* calculations for a range of HCH bond angles γ, and then averaged over these, weighted by the bending vibrational wave function determined under the assumption that the CH distance remained fixed. [31] In principle, a next step would be the investigation of how this approximation of a

rigid bond affects the $CH_2(\tilde{X})$–He PES.

We also showed that the variation in state-to-state cross sections for the four lowest bending vibrational levels in the $CH_2(\tilde{X})$ state is due to differences in the energy gaps between the k_a stacks. The increasing degree of linearity with increasing vibrational excitation implies that the inter k_a stack energy gaps increase with bending vibration. Consequently, the cross sections for transitions inelastic in k_a decrease in magnitude as v_b increases.

In this chapter we also examined vibrationally inelastic scattering of $CH_2(\tilde{X})$, in a manner similar to that being used by Ma and Dagdigian [119,120] for collisions of the methyl radical (CH_3) with He. Investigation of the efficiency of vibrationally inelastic, as compared to purely rotationally inelastic, relaxation of CH_2, is of considerable importance in the complete modeling of the collisional relaxation of this important radical in non-equilibrium environments.

We have found that the ro-vibrational relaxation is about two orders of magnitude less efficient than rotational relaxation within a particular bending vibrational level. Thus, in the study, contained in Chap. 6 on collision-induced electronic energy transfer between the $\tilde{a}$ and the $\tilde{X}$ states of CH_2, we can reasonably ignore the vibrational relaxation within the $\tilde{X}$ state and assume that the CH_2 molecule remains in a particular bending vibrational level, in which the singlet-triplet gateway (see Sec. 2.2.4) occurs.

The present chapter, taken together with our previous study of CH_2 in Chap. 4, demonstrates that the overall efficiency and the detailed state-to-state pathways of rotational relaxation are very dependent on the electronic state. The extent of this

difference is larger than one might anticipate from a consideration of the relaxation of a diatomic molecule, where the anisotropy of the electronic charge distribution in the allowable valence states is very similar. In the case of CH_2, the difference is due to a remarkable, but easily understandable, variation in the anisotropy of the charge distribution. More generally, one should expect similar variations in other open-shell triatomic (and polyatomic) molecules. Thus, in modeling the kinetics of different excited states of these molecules, one should not uncritically adopt a single set of parameters which are independent of electronic state.

Chapter 6: Collision-Induced Intersystem Crossing between $CH_2(\tilde{a})$ and $CH_2(\tilde{X})$

6.1 Brief Introduction

As discussed in Sec. 2.2.4, the reactivity of the ground triplet and first excited singlet states of CH_2 are dramatically different. Collisions with other molecules (H_2, N_2, H_2O, CO_2, CH_4) or atoms (He, Ar) [9] can lead to electronic inelasticity, relaxing $CH_2(\tilde{a})$ to its ground triplet state. Collision-induced intersystem crossing (CIISC) [16] is of key importance in the relaxation kinetics of CH_2.

In Chap. 2 we introduced the mixed state model for intersystem crossing, developed initially by Freed and co-workers. [43] In this model transitions between different electronic states are facilitated by accidental degeneracies between the rotational levels in the two states. In the particular case of CH_2 these degeneracies involve the ground vibrational level of the $\tilde{a}$ state and the $v_b = 2$ and 3 bending vibrational levels of the $\tilde{X}$ state, as shown in Fig. 5.2. Rotational levels in the $\tilde{a}(0,0,0)$ and in the $\tilde{X}(0,2,0)$ and $(0,3,0)$ vibrational manifolds which are nearly degenerate and, further, have the same total angular momentum, are mixed by the small spin-orbit coupling between the $\tilde{a}$ and $\tilde{X}$ electronic states.

These mixed levels are called "gateway" states. Because the rotational level spacing is large in a hydride molecule, there are only a small number of nearly degenerate $\tilde{X}, \tilde{a}$ pairs with the same value of j. Bley and Temps have identified these, experimentally. [10] These pairs are shown in high resolution in Fig. 2.7. The relevant quantum numbers, and the degree of mixing, are enumerated in Tab. 2.2.

As discussed in Sec. 2.2.4, in the mixed-state model inter-electronic-state transitions can be simulated by pairwise mixing of the pure-state T-matrix elements. Chapters 4 and 5, [17, 18] describe our quantum scattering studies of scattering within, separately, the $\tilde{a}$ and the $\tilde{X}$ states. Here, we assumed no electronic state mixing. We compared in Figs. 4.10 and 5.14 calculated total removal rate constants for some $k_a = 1$ rotational levels of $CH_2(\tilde{a})$ with experimental results from Kommisarov, Hall, Sears and their co-workers. [12, 14] As shown in Figs. 4.10 and 5.14, for most levels, our results are about 20% larger than the experimental results.

This is not the case for the $(0,0,0)8_{18}$ level of the $\tilde{a}$ state, which forms a mixed pair with the $(0,2,0)9_{37}$ level of the $\tilde{X}$ state (see Tab. 2.2). The calculated removal rate constant for the united 8_{18} state is about 70% larger than the experimental rate constant for the nominally $\tilde{a}$ (singlet) component of the mixed pair, while the calculated removal rate constant for the unmixed 9_{37} level is about 10% smaller than the experimental rate constant for the nominally $\tilde{X}$ (triplet) component of the mixed pair. The difference between our theoretical results, calculated under the assumption of no state mixing, and the experimental observations shows the importance of the mixing between the $\tilde{a}$ and $\tilde{X}$ states.

In this chapter we investigate collision-induced intersystem crossing between

115

the $\tilde{a}$ and the $\tilde{X}$ states of CH_2, still in collision with He. The next subsection summarizes the mixed-state quantum scattering calculations. In subsection 6.3 we introduce a simple kinetic model for the relaxation kinetics in the presence of two coupled electronic states. We follow this with a full solution of the relaxation master equation for both states simultaneously. Here, we include also the three-fold spin degeneracy for the ground triplet state. For each mixed pair, only one of the spin triplets will be coupled with an $\tilde{a}$ state rotational level. In last subsection of this chapter, we compare our mixed-state rate constants with Hall and Sears' experimental results and summarize what we have learned about collision-induced intersystem crossing in CH_2.

6.2   Scattering Calculations

As discussed earlier in subsection 2.2.4, in the presence of the weak spin-orbit mixing between the $\tilde{X}$ and $\tilde{a}$ states, the mixed-state model allows us to calculate elements of the two-state $\mathbf{T}$ matrix from the $\mathbf{T}$ matrix for collisions of He with, separately, $CH_2(\tilde{a})$ and $CH_2(\tilde{X})$. These we have already determined.

We will further assume that the gateway process occurs through only one mixed-pair at a time. In other words, we ignore interference between two different gateways. We concentrate on pairs in which the mixing is $> 10\%$, and with rotational energies < 2000 cm^{-1}, above the lowest rotational level of the (0,2,0) vibrational level of the $\tilde{X}$ state. There are only 4 pairs which satisfy these criteria, all four in the ground (0,0,0) vibrational manifold of the $\tilde{a}$ state. For *para*-CH_2, we have the $\tilde{a}$

state rotational levels 4_{31} and 6_{33} and their mixed partners, $(0,3,0)3_{12}$ and $(0,3,0)6_{16}$. For *ortho*-CH_2, we have the $\tilde{a}$ state rotational levels 7_{16} and 8_{18}, with their $\tilde{X}$ state mixed partners $(0,3,0)6_{15}$ and $(0,2,0)9_{37}$. All four pairs are listed in Table 2.2.

Scattering calculations at a collision energy of 300 cm^{-1} for these four pairs were carried out with the HIBRIDON suite of programs (see Chaps. 4 and 5 and Ref. [45]). Additional scattering calculations at various collision energies (up to 1300 cm^{-1}) for the $8_{18} - 9_{37}$ pair were carried out to compute the rate constants for transitions involving this mixed pair. This was done by numerical integration of Eq. (3.31) using repeated trapezoidal integration on a grid of collision energies (E_c) of width 20 cm^{-1} extending up to 2500 cm^{-1}.

6.3 Relaxation Kinetics

6.3.1 A Simplistic Model

We will first consider a simplistic model for the relaxation of a mixed pair, in which collisions can transfer population between these levels as well as into two separate baths consisting of all the other $\tilde{a}$ and $\tilde{X}$ rotational levels. Population will not be allowed to return from the bath to the mixed pair. We designate the two mixed-state levels with, respectively, nominal $\tilde{a}$ and nominal $\tilde{X}$ character as "A" and "X". These levels will be interconnected and coupled to the two baths by 6 rate constants, as illustrated in Fig. 6.1.

With a realistic choice of rate constants, determination the time dependence of the populations in the "X" and "A" levels will give us qualitative insight into the
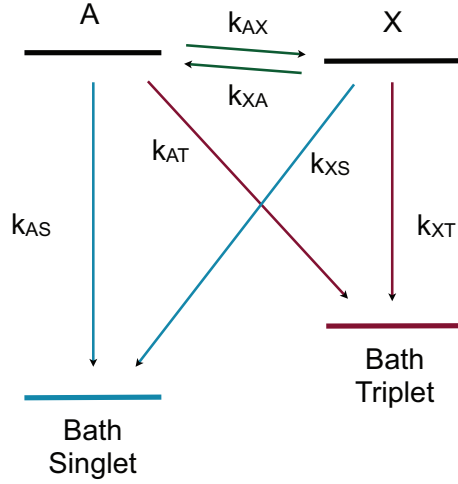
Figure 6.1: A simple model for the relaxation of a pair of mixed levels and two baths made up of all singlet and, respectively, all triplet levels, exclusive of the pair of levels which are mixed. Return of population from the baths to the mixed levels is not allowed.

relaxation kinetics of a mixed level system. The master equation for relaxation of the populations in these two levels is

$$\frac{dn_A}{dt} = \rho[-k_{AX}n_A - k_{AS}n_A - k_{AT}n_A + k_{XA}n_X] = \rho[-k_A n_A + k_{XA}n_X] \qquad (6.1)$$

and

$$\frac{dn_X}{dt} = \rho[-k_{XA}n_X - k_{XS}n_X - k_{XT}n_X + k_{AX}n_A] = \rho[k_{AX}n_A - k_X n_X] \qquad (6.2)$$

where ρ is the number density of the buffer gas,

$$k_A = k_{AX} + k_{AS} + k_{AT}, \qquad (6.3)$$

and

$$k_X = k_{XA} + k_{XS} + k_{XT} \qquad (6.4)$$

118

Since the gateway states have the same rotational quantum number and have nearly the same energy (see Table 2.2), we assume $k_{AX} = k_{XA}$. The 2×2 symmetric rate matrix

$$\mathbf{K} = \begin{bmatrix} -k_A & k_{AX} \\ k_{AX} & -k_X \end{bmatrix} \tag{6.5}$$

can be diagonalized with an orthogonal transformation $\mathbf{D}$, so that

$$\mathbf{D}^T \mathbf{K} \mathbf{D} = \boldsymbol{\lambda}$$

where $\boldsymbol{\lambda}$ is a diagonal matrix with elements λ_1 and λ_2. The master equation can be rewritten in matrix notation as

$$\frac{d}{dt}\left(\mathbf{D}^T \begin{bmatrix} n_A \\ n_X \end{bmatrix} \right) = \rho \left(\mathbf{D}^T \mathbf{K} \mathbf{D} \right) \left(\mathbf{D}^T \begin{bmatrix} n_A \\ n_X \end{bmatrix} \right), \tag{6.6}$$

or more simply,

$$\frac{d}{dt}\begin{bmatrix} \mathcal{N}_A \\ \mathcal{N}_X \end{bmatrix} = \rho \begin{bmatrix} \lambda_1 & 0 \\ 0 & \lambda_2 \end{bmatrix} \begin{bmatrix} \mathcal{N}_A \\ \mathcal{N}_X \end{bmatrix}. \tag{6.7}$$

where the vector $\mathcal{N}$ is the product of matrix $\mathbf{D}^T$ and the vector $\mathbf{n}$. These transformations lead to a master equation which is uncoupled. Thus, the time-dependence of $\mathcal{N}_A$ and $\mathcal{N}_X$ is

$$\mathcal{N}_i(t) = \exp\left(\rho \lambda_i t\right) \mathcal{N}_i(t=0) = \exp\left(\rho \lambda_i t\right) \mathcal{N}_i^{(0)} \tag{6.8}$$

From our prior calculations on the unmixed $\tilde{X}$ and $\tilde{a}$ states, one can estimate reasonable values for rate constants which appear in the model rate matrix of Eq. (6.5). We obtain

$$\mathbf{K} = \begin{bmatrix} -7.15 & 5.26 \\ 5.26 & -6.78 \end{bmatrix} \tag{6.9}$$

in units of 10^{-10}molecule·cm^{-3}·s^{-1}. The eigenvectors $\mathbf{D}$ and eigenvalues $\boldsymbol{\lambda}$ are

$$\mathbf{D} = \begin{bmatrix} -0.719 & 0.695 \\ -0.695 & -0.719 \end{bmatrix} \quad \text{and} \quad \boldsymbol{\lambda} = \begin{bmatrix} -12.228 \\ -1.702 \end{bmatrix}. \tag{6.10}$$

Again, the units of λ are 10^{-10}molecule·cm^{-3}·s^{-1}. Thus the populations of the mixed states are

$$
\begin{aligned}
n_A &= -0.719\mathcal{N}_A - 0.695\mathcal{N}_X \\
&= -0.719\mathcal{N}_A^{(0)} \exp\left(-12.228\tau\right) - 0.695\mathcal{N}_X^{(0)} \exp\left(-1.702\tau\right)
\end{aligned} \tag{6.11}
$$

and

$$
\begin{aligned}
n_X &= 0.695\mathcal{N}_A - 0.719\mathcal{N}_X \\
&= 0.695\mathcal{N}_A^{(0)} \exp\left(-12.228\tau\right) - 0.719\mathcal{N}_X^{(0)} \exp\left(-1.702\tau\right)
\end{aligned} \tag{6.12}
$$

Here, τ is time in units of 10^{10}cm^3·molecule^{-1}·ρ^{-1}·s

Figure 6.2 shows the time dependence of the populations in the two mixed levels A and X under initial conditions of: (Left Panel) initial population in the A level; (Middle Panel) initial population in the X level; and (Right Panel) A/X

120
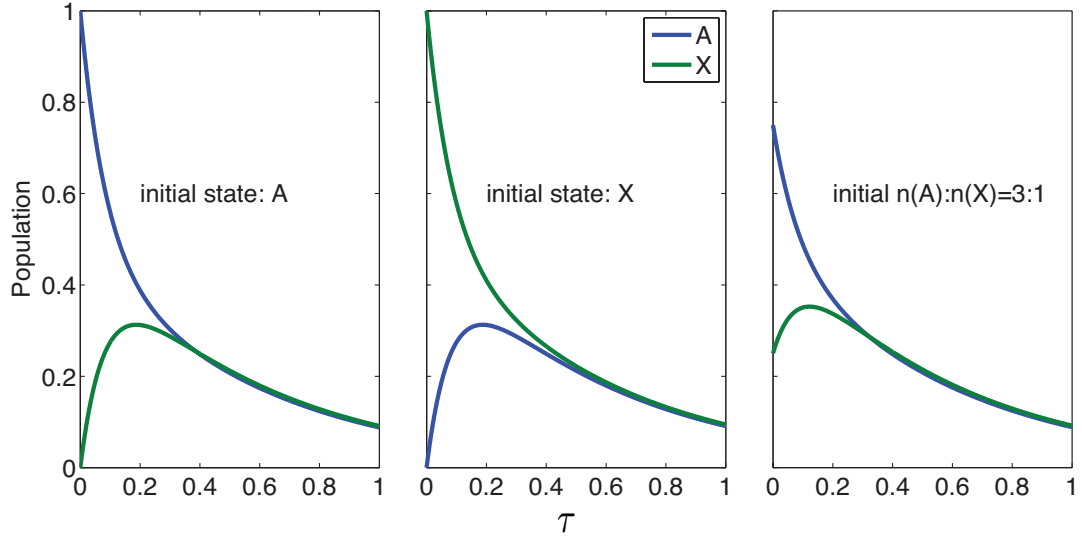
Figure 6.2: Time dependence of the populations of the two mixed levels in Fig. 6.1 with (left panel) initial population solely in the nominally singlet state (designated "A"), (middle panel) solely in the nominally triplet state (designated "X"), and (right panel) distributed 3:1 between singlet and triplet.

initially populated in a 3:1 ratio. Under all three initial conditions, the population of the level with higher initial population decreases rapidly while the population of the other level increases relatively slower, but still quickly. Once the populations of the two levels are equal, the two relax at the same rate.

Equations (6.11) and (6.12) show that the population evolution is governed by the two values of λ. As an illustration, Fig. 6.3 displays the contribution of the two terms in these equations to the population evolution of the A and X states with an initial 3:1 population distribution. This corresponds to the right panel of Fig. 6.2. The term corresponding to the large eigenvalue (shown in cyan) is responsible for the rapid population change at short time ($\tau < 0.25$), but then rapidly drops to zero. For $\tau > 0.25$ the second term (shown in red) dominates and describes the overall relaxation of the two states. We anticipate, then, that this picture - the populations in the mixed pair rapidly equilibrate and then relax in concert – will
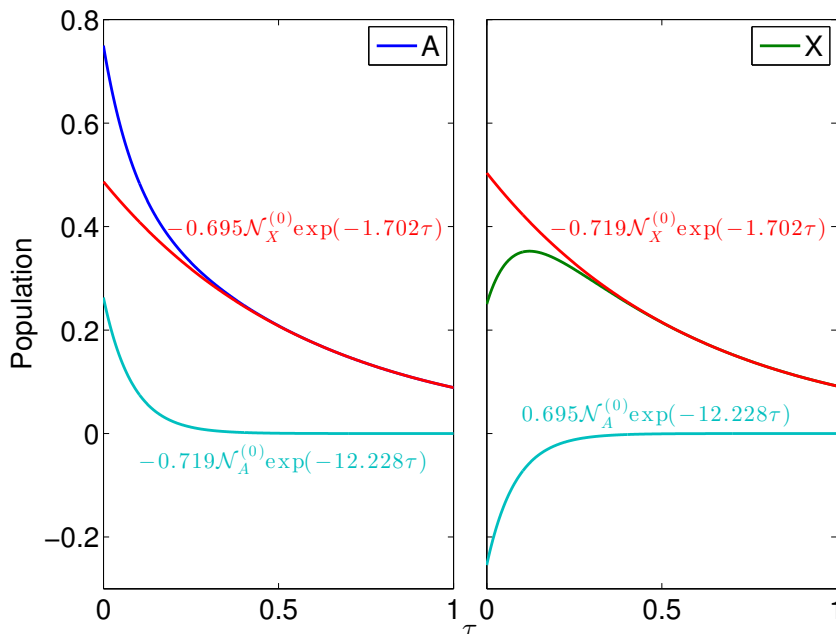
Figure 6.3: Contribution of the two terms in Eqs. (6.11) and (6.12) to the time evolution of the populations in the two levels of the mixed-state model. The initial distribution with an initial 3:1 A:X distribution.

remain valid when all the rotational levels are included.

6.3.2 The Full Master Equation for Relaxation

In the simplistic model (Fig. 6.1) we treat all the unperturbed singlet and triplet levels as two separate baths and further assume that the population lost to baths does not return. A more accurate picture includes transitions into and out of all levels. For a system with p rotational levels in the $\tilde{a}$ state and q rotational levels in the triplet $\tilde{X}$ state, relaxation is governed by a master equation of dimensionality $p + q$. Following Section 3.4, we write the master equation in matrix notation as [Eq. 3.32)]

$$\frac{d\mathbf{N}}{dt} = \rho\mathbf{KN} \qquad (6.13)$$

122

Here $\mathbf{N}$ is a column vector of the populations in the $p + q$ levels, namely (here we save space by giving the transpose of this column vector)

$$\mathbf{N}^T = \begin{bmatrix} N_{s_1} & \cdots & N_A & \cdots & N_{s_p} & N_{t_1} & \cdots & N_X & \cdots & N_{t_q} \end{bmatrix}$$

The ij^{th} element of the matrix of rate constants $\mathbf{K}$ is the rate constant, at temperature T for a transition between level i and level j.

In the absence of mixing, the rate constant matrix is block diagonal in the electronic state index, namely

$$\mathbf{K} = \begin{bmatrix} \mathbf{K}_a & \mathbf{0} \\ \mathbf{0} & \mathbf{K}_X \end{bmatrix} \tag{6.14}$$

where $\mathbf{K}_a$ and $\mathbf{K}_X$ are the full $p \times p$ and $q \times q$ matrices of the rate constants for transitions within, respectively, the $\tilde{a}$ and $\tilde{X}$ states. We will treat, separately, each pair of mixed levels. These two levels we designate, as in the simplistic model, "A" and "X". As discussed formally in Sec. 2.2.4, levels A and X will couple with all levels, in both electronic states. Thus, the rate constant matrix will be modified from the block-diagonal form of Eq. (6.14) by changing the rows and columns corresponding to the indices of the A and X levels into full columns and full rows. This is illustrated, schematically, in Fig. 6.4.

Each rate constant is an integral over collision energy of the appropriate cross section [see Eq. (3.31)]. To simply the problem, the upper triangle of the rate matrix were computed with a scattering calculation, while the lower triangle were computed

$$
\left[\begin{array}{ccccc|ccccc}
k_s & \cdots & k_s & \cdots & k_s & 0 & \cdots & 0 & \cdots & 0 \\
\vdots & \ddots & \vdots & \ddots & \vdots & \vdots & \ddots & \vdots & \ddots & \vdots \\
k_s & \cdots & k_s & \cdots & k_s & 0 & \cdots & 0 & \cdots & 0 \\
\vdots & \ddots & \vdots & \ddots & \vdots & \vdots & \ddots & \vdots & \ddots & \vdots \\
k_s & \cdots & k_s & \cdots & k_s & 0 & \cdots & 0 & \cdots & 0 \\
\hline
0 & \cdots & 0 & \cdots & 0 & k_t & \cdots & k_t & \cdots & k_t \\
\vdots & \ddots & \vdots & \ddots & \vdots & \vdots & \ddots & \vdots & \ddots & \vdots \\
0 & \cdots & 0 & \cdots & 0 & k_t & \cdots & k_t & \cdots & k_t \\
\vdots & \ddots & \vdots & \ddots & \vdots & \vdots & \ddots & \vdots & \ddots & \vdots \\
0 & \cdots & 0 & \cdots & 0 & k_t & \cdots & k_t & \cdots & k_t
\end{array}\right]
\qquad
\left[\begin{array}{ccccc|ccccc}
k_s & \cdots & k_{As} & \cdots & k_s & 0 & \cdots & k_{Xs} & \cdots & 0 \\
\vdots & \ddots & \vdots & \ddots & \vdots & \vdots & \ddots & \vdots & \ddots & \vdots \\
k_{sA} & \cdots & k_{AA} & \cdots & k_{sA} & k_{tA} & \cdots & k_{XA} & \cdots & k_{tA} \\
\vdots & \ddots & \vdots & \ddots & \vdots & \vdots & \ddots & \vdots & \ddots & \vdots \\
k_s & \cdots & k_{As} & \cdots & k_s & 0 & \cdots & k_{Xs} & \cdots & 0 \\
\hline
0 & \cdots & k_{At} & \cdots & 0 & k_t & \cdots & k_{Xt} & \cdots & k_t \\
\vdots & \ddots & \vdots & \ddots & \vdots & \vdots & \ddots & \vdots & \ddots & \vdots \\
k_{sX} & \cdots & k_{AX} & \cdots & k_{sX} & k_{tX} & \cdots & k_{XX} & \cdots & k_{tX} \\
\vdots & \ddots & \vdots & \ddots & \vdots & \vdots & \ddots & \vdots & \ddots & \vdots \\
0 & \cdots & k_{At} & \cdots & 0 & k_t & \cdots & k_{Xt} & \cdots & k_t
\end{array}\right]
$$

Figure 6.4: Schematic of the rate constant matrix for a pair of mixed levels. (Left matrix) the **K** matrix in the absence of mixing, block-diagonal in the multiplicity (singlet or triplet) [see Eq. (6.14)]. (Right matrix) In the presence of spin-orbit coupling the two rows and two columns (indicated by orange stripes) corresponding the the A/X mixed pair, now extend across both the singlet and triplet levels.

by detailed balance

$$
g_i \exp\left(-E_i/k_B T\right) k_{i \to j} = g_j \exp\left(-E_j/k_B T\right) k_{j \to i}, \tag{6.15}
$$

where g_i is the degeneracy of the ith level, k_B is the Boltzmann constant and E is the internal energy of the level.

For transitions between two unperturbed levels, the rate constants are identical to those calculated for purely $\tilde{a}$ and $\tilde{X}$ states, described in Chaps. 4 and 5 and in our previously published articles. [17, 18] Thus we only need to determine the two modified rows and two modified columns which correspond to the transitions to and from the two mixed levels (shown schematically in yellow in Fig. 6.4).

To solve the master equation set, we adopted the method presented by Alexander, Hall and Dagdigian in a recent paper, [48] as we did for the simple model. Unlike the simple model, in this simulation the rate matrix is not symmetric but the off-

diagonal elements are related by detailed balance [Eq. (6.15)]. Following Eqs. 8–13 of Ref. [48], we transform the rate matrix $\mathbf{K}$ to a symmetric matrix

$$\tilde{\mathbf{K}} = (\mathbf{\Pi}^{1/2})^{-1}\mathbf{K}\mathbf{\Pi}^{1/2}, \tag{6.16}$$

Here $\mathbf{\Pi}$ is a diagonal matrix whose elements are the Boltzmann populations in each level, [48] namely

$$\mathbf{\Pi}_{ij} = \delta_{ij}g_j \exp(-E_j/k_BT)/Z$$

where Z, the partition function is the sum of this factor over all values of j.

This results in a modified master equation

$$d\tilde{\mathbf{n}}/dt = \rho\tilde{\mathbf{K}}\tilde{\mathbf{n}}, \tag{6.17}$$

where $\tilde{\mathbf{n}} = (\mathbf{\Pi}^{1/2})^{-1}\mathbf{n}$ and the square root of a diagonal matrix is a diagonal matrix of the square roots of the diagonal elements. Now, following the same procedure as in the simple model (Sec. 6.3.1), we can diagonalize $\tilde{\mathbf{K}}$ and solve for the time evolution of all rotational levels in both the $\tilde{a}$ and $\tilde{X}$ states.

6.3.3 Triplet Multiplet Levels

In Chap. 5 we ignored the spin-splitting of each rotational level of the $\tilde{X}$ state, since the splitting is only a fraction of a wavenumber, [37] treating the molecule as a singlet with the same rotational level structure. Since the interaction potential does not explicitly depend on the spin, one can use the spin-free T-matrix elements

to generate those for transitions between the spin-resolved multiplets. [121, 122]

For simplicity, here, as in Sec. 3.2, we will first assume that the CH_2 molecule is a symmetric top. In the spin-free approximation, we determine T-matrix elements between the $|nklJM\rangle$ states defined in Eq. (3.14). If spin is included, then we need to first vector couple the spin-free CH_2 rotational states ($|nkm_n\rangle$) with the spin-states $|SM_S\rangle$, with $S = 1$ for a triplet. We have then

$$|nkSjm_j\rangle = \sum_{m_n, M_S} (nm_n SM_S | jm_j) |nkm_n\rangle |SM_S\rangle$$

where j is the total molecular angular momentum (rotational plus spin) with space-fixed projection M_S. These states are then coupled with the orbital angular momentum states $|lm_l\rangle$ corresponding to the rotation of the He atom in the same way

$$
\begin{aligned}
|nkSjl\mathcal{J}\mathcal{M}\rangle &= \sum_{m_j, m_l} (jm_j lm_l | \mathcal{J}\mathcal{M}_\mathcal{J}) |nkSjm_j\rangle |lm_l\rangle \qquad (6.18) \\
&= \sum_{m_j, m_l} \sum_{m_n, M_S} (jm_j lm_l | \mathcal{J}\mathcal{M}_\mathcal{J})(nm_n SM_S | jm_j) |nm_n k\rangle |SM_S\rangle |lm_l\rangle
\end{aligned}
$$

Here, $\mathcal{J}$ is the total angular momentum of the atom + molecule (including spin) and $\mathcal{M}_\mathcal{J}$ is its space-frame projection.

Now, from the orthogonality properties of the Clebsch-Gordon coefficients, [123] we can reverse Eq. (3.14), obtaining

$$|lm_l\rangle |nm_n k\rangle = \sum_{JM} (nm_n lm_l | JM) |nklJM\rangle$$

Inserting this result in Eq. (6.18) we find

$$
\begin{aligned}
|nkSjl\mathcal{J}\mathcal{M}\rangle &= \sum_{m_j,m_l} \sum_{m_n,M_S} \sum_{JM} (jm_j lm_l|\mathcal{J}\mathcal{M}_\mathcal{J})(nm_n SM_S|jm_j) \\
&\times (nm_n lm_l|JM)|nklJM\rangle|SM_S\rangle
\end{aligned}
\tag{6.19}
$$

Thus, a matrix element of the T operator in the basis [Eq. (6.18)] containing the spin is

$$
\langle n'k'S'j'l'\mathcal{J}\mathcal{M}|\hat{T}|nkSjl\mathcal{J}\mathcal{M}\rangle \equiv T^{\mathcal{J}\mathcal{M}}_{n'k'S'j'l',nkSjl} = \sum_{\substack{m_j,m_l,m_n,M_S,J,M \\ m_{j'},m_{l'},m_{n'},M_{S'},J',M'}} (jm_j lm_l|\mathcal{J}\mathcal{M}_\mathcal{J})
$$

$$
\times (j'm_{j'} l'm_{l'}|\mathcal{J}\mathcal{M}_\mathcal{J})(nm_n SM_S|jm_j)(n'm_{n'} S'M_{S'}|j'm_{j'})(nm_n lm_l|JM)(n'm_{n'} l'm_{l'}|J'M')
$$

$$
\times \langle n'k'l'J'M'|\langle S'M_{S'}|\hat{T}|SM_S\rangle|nklJM\rangle
\tag{6.20}
$$

Now, if we neglect spin-orbit coupling, the T operator is independent of spin (since the interaction potential does not depend on the spin) so that

$$
\langle S'M_{S'}|\hat{T}|SM_S\rangle = \delta_{S'S}\delta_{M_{S'}M_S}\hat{T}
$$

Further, the matrix elements of the T operator in the $|nklJM\rangle$ (the basis we used for the spin-free scattering calculations) is diagonal in the total angular momentum J (in the spin-free treatment) and its projection M, so that

$$
\langle n'k'l'J'M'|\hat{T}|nklJM\rangle = \delta_{J'J}\delta_{M'M}T^{JM}_{n'k'l',nkl}
$$

Thus, Eq. (6.20) simplifies to

$$T^{\mathcal{J}\mathcal{M}}_{n'k'S'j'l',nkSjl} = \delta_{SS'} \sum_{\substack{m_j,m_l,m_n,M_S,J,M \\ m_{j'},m_{l'},m_{n'}}} (jm_jlm_l|\mathcal{J}\mathcal{M}_\mathcal{J})(j'm_{j'}l'm_{l'}|\mathcal{J}\mathcal{M}_\mathcal{J}) \quad (6.21)$$
$$\times (nm_nSM_S|jm_j)(n'm_{n'}SM_S|j'm_{j'})(nm_nlm_l|JM)(n'm_{n'}l'm_{l'}|JM)T^{JM}_{n'k'l',nkl}$$

Thus, we see that the T-matrix elements in the $S = 1$ basis can be written as sums, multiplied by vector coupling coefficients, of the T-matrix elements in the spin-free basis, which we have already calculated in Chap. 5. In reality, of course, the rotational states of the asymmetric top CH_2 are linear combinations of the $|nk\rangle$ symmetric top functions. Thus, the T-matrix elements between the asymmetric top states will be a double sum (over k' and k) of the $T^{\mathcal{J}\mathcal{M}}_{n'k'S'j'l',nkSjl}$ matrix elements.

6.4 Results

6.4.1 Cross Sections and Rate Constants

As shown in Eq. (3.25), inelastic cross sections can be determined as sums over the total angular momentum J of the absolute value squared of T-matrix elements between individual nkl states. In the presence of the spin-orbit mixing, the individual T matrix elements, for transitions between a mixed level and an unperturbed level are modified as described in Eqs. (2.22), (2.23), (2.24), and (2.25). Similarly, the T matrix elements between the two mixed states are modified as described in Eqs. (2.26), (2.27), and (2.28).

All the necessary T matrix elements were determined in the single-electronic-

128

state calculations described in Chaps. 4 and 5. In this part, we will attempt to probe the changes of inelastic and elastic cross sections for collision-induced rotational transitions within the $CH_2(\tilde{a})$ and $CH_2(\tilde{X})$ after including the spin-orbit coupling in the scattering calculations. Moreover, we aim at examining the time evolution of the collision kinetics by analyzing the state-to-state cross sections.

In Tab. 6.1, we list several integral cross sections out of the four levels of o-CH_2 which constitute the two *ortho* pairs in Tab. 2.2. The cross sections were first computed (upper three rows in Tab. 6.1) without including the spin-orbit mixing between the two electronic states. Thus, these cross sections are identical to those published earlier. [17,18] Then, we recomputed the same cross sections after including the coupling between the first pair, and, in a separate calculation, the second pair of states.

The mixed-pair provides the "gateway" between the singlet and triplet manifolds. The collisional coupling between these two gateway states is of particular interest. As discussed in Sec. 2.2.4, this coupling will be large, since the cross sections "borrow" strength from the scattering amplitudes for elastic transitions of the unmixed levels [see also Eq. (2.28)]:

$$T_{AX} = \cos\theta\sin\theta(T_{tt} - T_{ss}),\tag{6.22}$$

while the elastic transitions are weaker after including the mixing effect [see also

Table 6.1: Elastic, total removal and the largest state-to-state cross sections for transitions from selected levels of o-CH$_2$: $\tilde{a}, 8_{18}$ and $\tilde{X}, 9_{37}(0,2,0)$ as well as $\tilde{a}, 7_{16}$ and $\tilde{X}, 6_{15}(0,3,0)$, by collision with He at a collision energy of 300 cm^{-1}. In the mixed-state model these two pairs of levels ($8_{18}/9_{37}$ and $7_{16}/6_{15}$) are "gateways". We list cross sections computed first by neglecting, and then including (in the mixed-state model) the spin-orbit mixing between these pairs of gateway levels.

Transitions	Cross Sections / Å^2			
	$\tilde{a}\ 8_{18}$	$\tilde{X}\ 9_{37}(0,2,0)$	$\tilde{a}\ 7_{16}$	$\tilde{X}\ 6_{15}(0,3,0)$
	without spin-orbit coupling			
Elastic	65.3	73.0	65.3	73.9
Total removal	16.0[a]	5.7[a]	18.4	4.7
Largest state-to-state cross section	4.3[b]	1.3[c]	1.5[d]	2.3[e]
	with spin-orbit coupling			
Elastic	35.0	38.2	30.5	31.2
To the other mixed-pair level	32.7	32.5	38.8	38.7
Removal to all other singlet levels	11.3[a]	4.7[a]	9.9	8.5
Removal to all other triplet levels	1.6[a]	4.0[a]	2.2	2.5
Largest state-to-state cross section	3.1[b]	0.9[c]	0.8[d]	1.2[e]

[a] The sum of the two total removal cross sections in blue in the upper table are equal to the sum of the four removal cross sections in red in the lower table.
[b] $\tilde{a}\ 8_{18} \rightarrow \tilde{a}\ 7_{34}$.
[c] $\tilde{X}\ 9_{37}(j=8) \rightarrow \tilde{X}\ 8_{35}(j=7)$.
[d] $\tilde{a}\ 7_{16} \rightarrow \tilde{a}\ 7_{07}$.
[e] $\tilde{X}\ 6_{15}(j=7) \rightarrow \tilde{X}\ 4_{13}(j=5)$.

Eqs. (2.26) and (2.27)]:

$$T_{aa} = \cos^2\theta\ T_{ss} + \sin^2\theta\ T_{tt}$$

$$T_{XX} = \sin^2\theta\ T_{ss} + \cos^2\theta\ T_{tt}. \tag{6.23}$$

The results in the lower portion of Tab. 6.1 show, that the elastic cross sections are smaller after including the mixing, for all four initial levels. On the other hand, the cross sections for transitions to the other perturbed state($8_{18} \longleftrightarrow 9_{37}$, $7_{16} \longleftrightarrow 6_{15}$), are significantly larger than all the other inelastic cross sections. In particular, for the 7_{16} and 6_{15} pair, where the mixing is nearly maximal ($\sim 50\%$), the cross sections to the other perturbed level are even larger than the elastic cross sections, due to the maximized mixing angle. To a good approximation, in the presence of mixing the elastic flux is partitioned among the purely elastic transition ($A \to A$ and $X \to X$) and the inter-pair transitions ($X \to A$ and $A \to X$).

Also, as revealed by Eqs. (2.22) and (2.24), the cross sections from the mixed singlet level to the other singlet levels, and from the mixed triplet level to the other triplet level is reduced by a factor of $|\cos \theta|^2$. But, Eqs. (2.23) and (2.25) show that this loss is partially compensated for by the addition of transitions from the nominally singlet component of the mixed pair to the triplet rotational levels and, vice-versa, from the nominally triplet component of the mixed pair to the singlet rotational levels, both of which appear with an intensity factor of $|\sin \theta|^2$. Thus, since $\cos \theta^2 + \sin \theta^2 = 1$, the sum of the removal cross sections out of the two unmixed levels of the nearly-degenerate pair are very close in magnitude to the sum of the removal cross sections to the rotational manifolds of both the $\tilde{a}$ and $\tilde{X}$ states out of these same levels when they are mixed. This is seen by comparing the sum of the two blue entries in the upper section of Tab. 6.1 with the sum of the four red entries in the lower section.

Figure 6.5 shows graphically the crosss section tabulated in the lower section of

Tab. 6.1. These cross sections are at a collision energy of 300 cm^{-1}. Notwithstand-
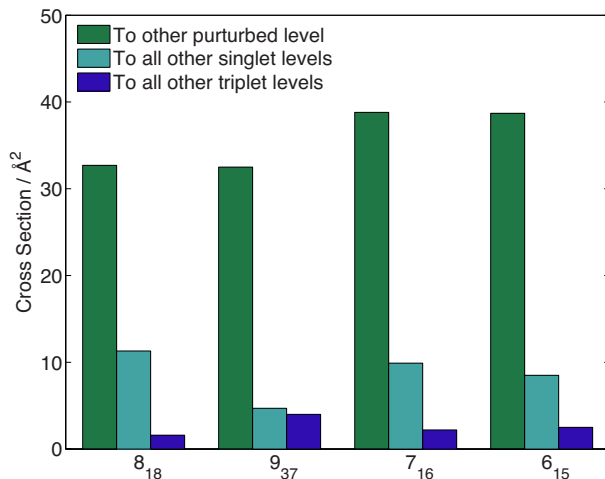
Figure 6.5: Bar plot of cross sections for transitions from both components of the two mixed pairs: $8_{18}(\tilde{a})$ and $9_{37}(\tilde{X}, v_b = 2)$ as well as $7_{16}(\tilde{a})$ and $6_{15}(\tilde{X}, v_b = 3)$, to the other component of the mixed level, to all other $^1\tilde{a}$ levels and to all other $^3\tilde{X}$ levels, by collision with He at a collision energy of 300 cm^{-1}.

ing, we can use the results shown in Tab. 6.1 and Fig. 6.5 to make a few qualitative predictions about the relaxation of a non-equilibrium sample of CH$_2$ in the two electronic states. Relaxation between two mixed states will be the most rapid process. Since the two states in a mixed pair have the same j and nearly the same energy, their thermal distributions will be equal. Thus, the fastest relaxation process will be the restoration of equal populations in the two mixed levels. Subsequently, these two levels will relax to the other unperturbed $\tilde{a}$ state levels. However, the largest state-to-state cross sections for this process (3.1 Å^2), is an order of magnitude slower than those for equilibration of population between the two mixed levels. Finally, transitions to other unperturbed $\tilde{X}$ state levels will be somewhat slower.

Since the (0,2,0) bending vibrational level of the $\tilde{X}$ state lies more than 1300 cm^{-1} lower than the (0,0,0) vibrational level of the $\tilde{a}$ state (see Fig. 5.2),

for calculations in which the collision energy in the $\tilde{a}$ state is ~ 1000 cm^{-1}, the comparable collision energy for the levels of the $\tilde{X}(0,2,0)$ state will be greater than 2000 cm^{-1}. To simplify the computational requirements, we carried out scattering calculations for collision energies only up to 1300 cm^{-1} and set cross sections for collision energies greater than 1300 cm^{-1} equal to the value at that energy. Because the Boltzmann weighting in Eq. (3.31) $[E_c \exp(-E_c/k_B T)]$ decreases rapidly at high collision energy, test calculations indicate that the error in the room temperature rate constants introduced by this extrapolation will be at most 1%.

The mixed pair involves only one j, n multiplet of the $\tilde{X}$ state. Since the interaction potential is independent of the spin, it is possible, as outlined in Sec. 6.3.3 to determine T-matrix elements for transitions between the spin-multiplets $|jnk\rangle$ from the T-matrix elements in the spin-free ($|nk\rangle$) basis; see Eq. (6.22). Table 6.2 presents cross sections for transitions out of the nominally triplet component of the $8_{18}/9_{37}$ mixed pair, the $|jnk_ak_c\rangle = |8937\rangle$ level, into (a) the other two $n = 9$ levels ($j = 9$ and $j = 10$) and (b) into the three spin-multiplets of the $n = 7$ level.

We see a strong propensity for transitions where $\Delta j = \Delta n$. Initially, $\vec{S}$ and $\vec{n}$ are coupled to form $\vec{j}$. The collision affects only $\vec{n}$. After the collision $\vec{n}'$ recouples with $\vec{S}$. Because $\vec{S}$ is unaffected, in this recoupling the relative orientation of $\vec{S}$ and $\vec{n}'$ is preserved. This has been seen before in studies of spin-resolved transitions of O_2 in its $^3\Sigma^-$ states (which, with a triplet coupled $\pi_x^1 \pi_y^1$ electron occupancy, is comparable to linear CH_2 in the $^3\tilde{X}$ state). [124] A similar effect is found in collisional coupling of molecular hyperfine levels. [125]

This $\Delta j = \Delta n$ propensity is seen in transitions both elastic in n ($j = n-1, n \to$

133

$j = n, n$ and $j = n + 1, n$), and inelastic ($n = 9 \to 7$). Cross sections for transitions which do not obey this rule are 3 orders of magnitude smaller, comparable to the vibrationally inelastic cross sections examined in Sec. 5.4.2.

When spin is included, one $n \to n'$ transition in the spin-free limit becomes partitioned into nine $j, n \to j', n'$ transitions. We see from Tab. 6.2 that to a very good approximation, the spin-resolved cross sections obey a simple conservation rule

$$\sigma_{n \to n'}^{(\text{spin-free})} \approx \frac{1}{2S + 1} \sum_{j=n-1}^{n+1} \sum_{j'=n'-1}^{n'+1} \sigma_{j,n \to j',n'}$$

Table 6.2: Cross sections for transfer between the spin multiplets of the $\tilde{X}$ state.

Transitions	Cross Sections / Å^2			
	Multiplet ignored	Multiplet included		
Elastic	73.09	73.04		
Total removal	5.61	5.66		
		$j = 8$	$j = 9$	$j = 10$
to other 9_{37} levels	73.09	73.04	4.23×10^{-2}	5.55×10^{-4}
		$j = 6$	$j = 7$	$j = 8$
to 7_{35} levels	1.09	1.05	3.73×10^{-2}	6.92×10^{-4}

6.4.2 Master Equation Simulation

Making use of our calculated rate constants, we wrote a MATLAB script to solve the relaxation master equation [Eq. (6.13)]. This allows us to explore the time dependence of the populations of rotational levels in both the $\tilde{a}$ and $\tilde{X}$ states. In these simulations, we include 48 rotational levels in the (0,0,0) vibrational manifold of the $^1\tilde{a}$ state and 160 rotational levels in the (0,2,0) vibrational manifold of the $^3\tilde{X}$ state. The three fine-structure components for each triplet $n_{k_a k_c}$ level [with $j = n - 1, n, n + 1$] are included as distinct levels.

We ignore relaxation of the bending mode, consistent with the results of Chap. 5 in which we concluded that for CH_2 vibrational relaxation is at least of two orders of magnitude slower. Thus, for mixing between the 8_{18} level of the $\tilde{a}$ state and the $9_{37}(0, 2, 0)$ level of the $\tilde{X}$ state, both in o-CH_2, we included only rotational levels in the (0,2,0) manifold of the $\tilde{X}$ state.

In Chaps. 4 and 5, we have seen that the $\Delta k_a = 0, \Delta n = \pm 1$ and $\Delta k_a = 2, \Delta n = 0$ transitions make the dominant contribution to the total removal cross sections out of a single rotational level of the $\tilde{a}$ state. Similarly the $\Delta k_a = 0, \Delta n = -1/-2$ and $\Delta k_a = -1, \Delta n = 2$ transitions are the strongest for relaxation of the $\tilde{X}(0,2,0)$ state. For the $8_{18}/9_{37}(0, 2, 0)$ pair, these strong transitions lead to $\tilde{a}$ state final levels of 7_{16}, 9_{18} and, in the $\tilde{X}$ state, the final levels 8_{36} and 8_{35}, 7_{35} and $11_{2,10}$. All these levels, and also some at higher energy, are included in the simulation.

We set both the translation and rotational temperature to 300 K and the bath pressure to 2 Torr. These values are consistent with ongoing experimental
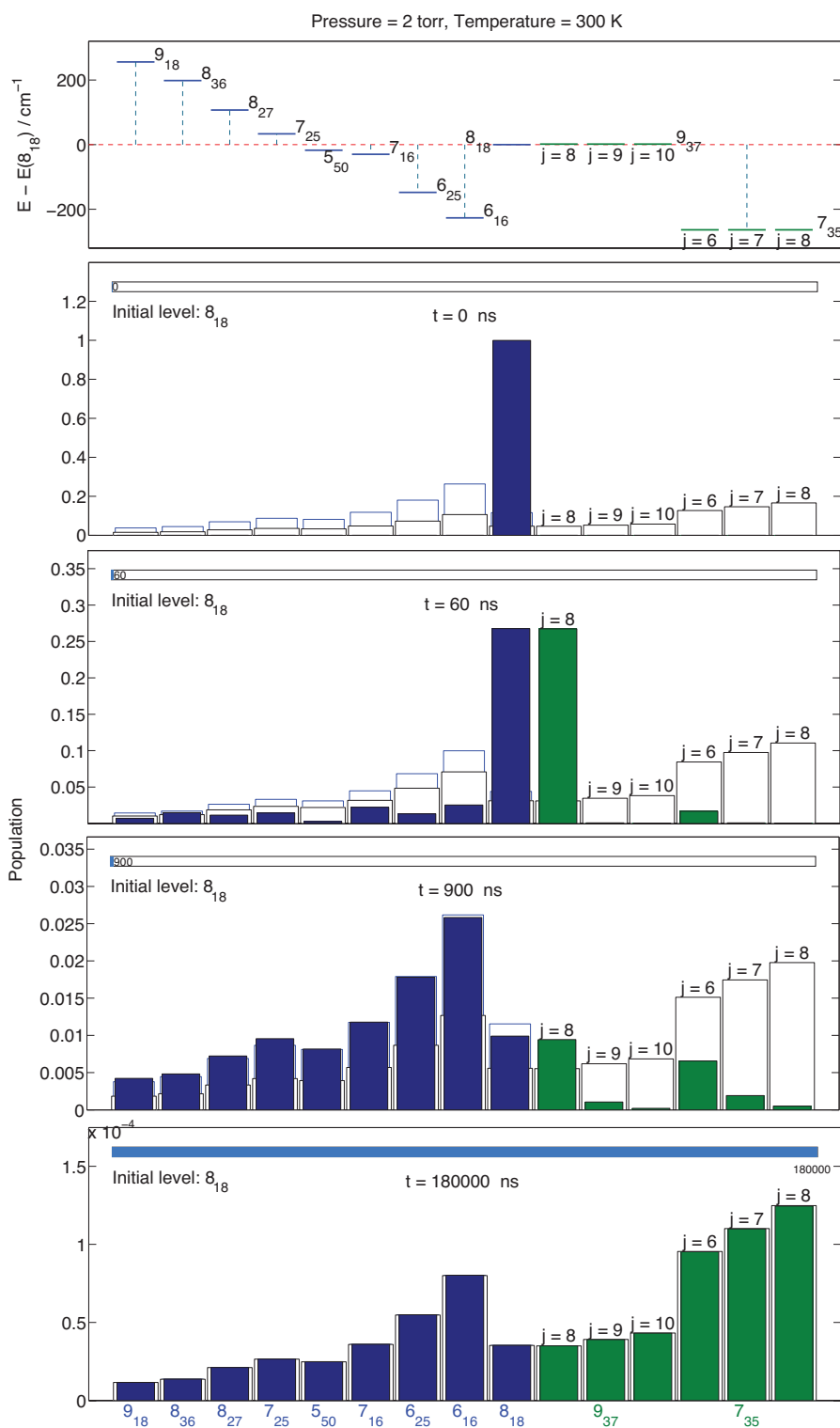
Figure 6.6: Rotational distribution of selected singlet and triplet levels at various times. Initial population in the 8_{18} component of the mixed pair.

investigation. [14] We assume that both T and p do not change. The pressure affects the number density of the collision partners ρ in Eq. (3.32), but not the rate matrix. By varying the initial distribution of rotational levels, we can access the time dependence of rotational populations at different initial conditions. Especially, we are interested in starting from one particular rotational level, and observing the time evolution of the re-distribution process.

Our MATLAB script allows us to visualize the entire time evolution, as a histogram of changing populations. The first example is the evolution of the population subsequent to initial population in the nominal 8_{18} (nominal $\tilde{a}$) component of the $8_{18}/9_{37}$ mixed pair. Figure 6.6 presents three snapshots, following initial population of the 8_{18} level, the nominally $\tilde{a}$ level of the particular mixed-pair of o-CH$_2$ under study at Brookhaven. [12, 46] In the top panel, we plot the positions of some of the nearby rotation levels in both the $\tilde{a}$ (blue) state and the $\tilde{X}$ (green) states. For the triplet levels we include both the other mixed pair (9_{37}) and the 7_{35} level. The $9_{37} \rightarrow 7_{35}$ transition is one of the strongest relaxation pathways in the $\tilde{X}$ state. We show explicitly each of the three fine-structure components of these two rotational levels (these are degenerate to within the resolution of the figure). For the $\tilde{a}$ state we include more final rotational states, covering transitions with $\Delta k_a = [0, 1, 2]$, $\Delta n = [-3, -2, -1, 0, 1]$, and $\Delta E = -200 \sim 200$ cm^{-1}.

The four lower panels of Fig. 6.6 display bar histogram plots of the initially normalized populations at three different times (chosen on a logarithmic scale). Two square empty boxes are plotted for each of the $\tilde{a}$ state levels, of which the black one represents the Boltzmann population including all $\tilde{a}$ and $\tilde{X}$ levels, while

the blue empty box represents the relative Boltzmann population among the $\tilde{a}$ levels in the absence of coupling to the $\tilde{X}$ state. The lower panels present populations of these selected levels at different times. By 90 ns (middle panel), the populations in the two mixed levels, 8_{18} and $9_{37}(j = 8)$ have already equilibrated, considerably before significant population is seen in any of the other levels. This immediate re-distribution between the mixed levels is consistent with the large size of the cross section for transitions between the two mixed levels, which borrows intensity from the elastic scattering amplitudes in the two states [see Eq. (2.28)].

In the fourth panel of the figure, at $t = 900$ ns, the blue boxes for the $\tilde{a}$ state levels are almost fully filled. By this time rotational relaxation within the $\tilde{a}$ state has reached equilibrium. From this point the population of all $\tilde{a}$ state levels decay at the same rate. Since the 8_{18} level lies ~ 1900 cm^{-1} above the lowest level in the simulation [the $0_{00}(j = 1)$ rotational level in the (0,2,0) vibrational manifold of the $\tilde{X}$ state], at 300 K, eventually all the population will have decayed out of the levels considered explicitly in this figure.

At $t = 900$ ns, the populations of the $\tilde{X}$ state levels (except the $\tilde{X}$ component in the mixed pair) are still low, as their black boxes for the Boltzmann distribution are still empty. This is true even for the 7_{35} level, which is relatively strongly correlated with the mixed-pair level 9_{37}. Note that even after evolving from 60 (middle panel) to ~ 900 ns (fourth panel), the populations of the two mixed levels remain equal, even though the population in both has decreased from ~ 0.25 to ~ 0.1.

Finally, the bottom panel shows the population distribution when relaxation among the levels displayed is essentially complete ($t = 180,000$ ns).
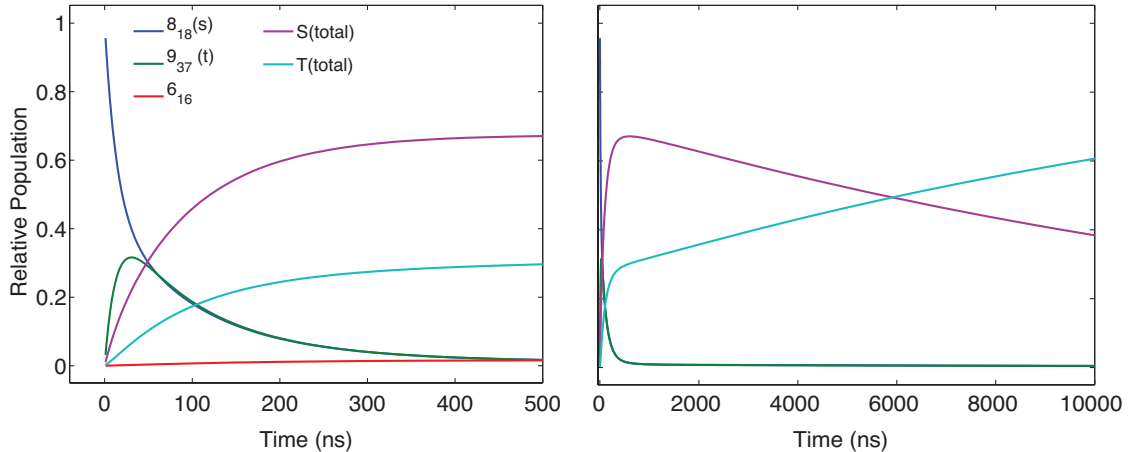
Figure 6.7: Time dependence of the (normalized) populations of the mixed singlet, the mixed triplet, an unperturbed level, all unperturbed singlet levels and all unperturbed triplet levels. Initial population was solely in the mixed singlet 8_{18} level. The left and right panels correspond to two different time ranges.

In Fig. 6.7 we show the evolution of some rotational populations over two different time scales. We include the two mixed states(8_{18} and 9_{37}), one unperturbed level 6_{16} as well as the total population in all singlet [designated S(total)] and all triplet [designated T(total)] unperturbed levels. This figures shows again that the two mixed states merge quickly to the same depletion rates within 50 ns. The $\tilde{a}$ state population then maximizes (at $t \approx 1000$ ns) only to diminish at longer time, as population recedes into the rotational levels of the energetically lower $\tilde{X}$ state in its (0,2,0) vibrational manifold.

In conclusion, for initial population in the singlet component of one of the mixed pairs, the relaxation process is composed of three major steps: very fast energy transfer to the mixed partner ($8_{18} \rightarrow 9_{37}$ in this case), the relatively fast rotational re-distribution within the $\tilde{a}$ state (900 ns), and the longer-time rotational re-distribution within the $\tilde{X}$ state.

Population confined initially not to one of the mixed-state levels but to a near

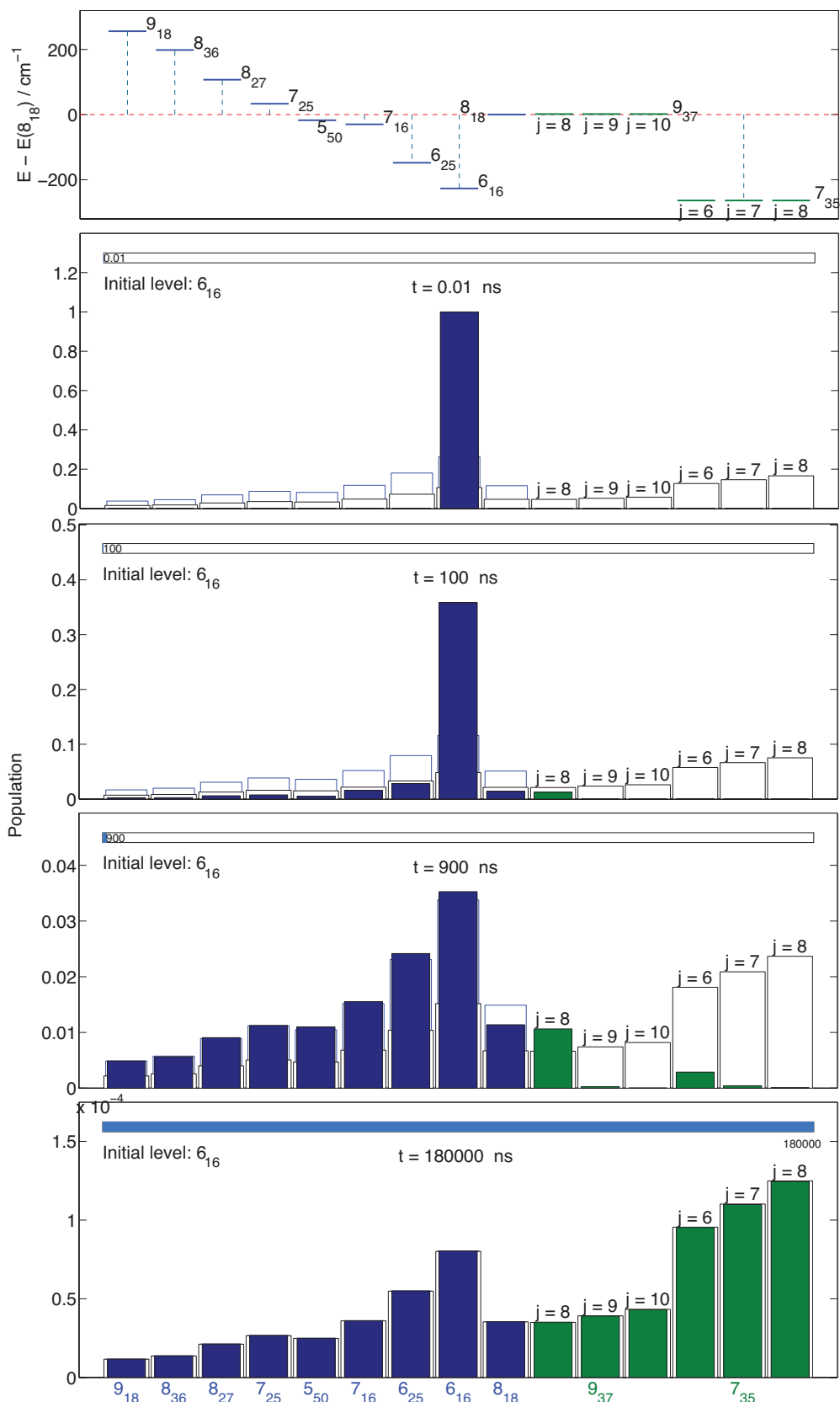Figure 6.8: Rotational distribution of selected singlet and triplet levels at various times. The system was initially populated to the 6_{16} unperturbed level.

by unperturbed level, for example $\tilde{a}\,6_{16}$, provides an interesting contrast. This is shown in Fig. 6.8.

Here the initial relaxation is slower, corresponding to redistribution of population among the other rotational levels of the $\tilde{a}$ state. We see, though, evidence of the strong mixing between the 8_{18} and 9_{37} levels. As population appears in the 8_{18} level, it shows up simultaneously in the other mixed-pair. The prompt re-distribution between the two mixed-state levels is not as obvious in this simulation because there the mixed levels are initially empty. However, once population is transferred into one, it appears in the other. Their populations are already equal at $t = 100$ ns.

By $t = 900$ ns, the relative populations are very similar to those shown in Fig. 6.6. Once population has equilibrated in the $\tilde{a}$ state levels, the subsequent population evolution is independent of which $\tilde{a}$ state level was populated initially. This is true both for the relative and absolute populations.

6.5   Discussion

As discussed in Chaps. 4 and 5, for most of $k_a = 1$ levels of $CH_2(\tilde{a})$ if we ignore mixing with the $\tilde{X}$ state, the calculated total removal rate constants are about 20% higher than the experimental observations by Hall and Sears. Surprisingly, for the 8_{18} level, the discrepancy between the calculated and experimental total removal rate constants, is much larger, about 70% [see Figs. 4.10 and 5.14]. In this chapter, we applied the mixed-state model to the CH_2He system, concentrating on 8_{18} as the $\tilde{a}$ "gateway" level. Table 6.1 shows that inclusion of the spin-orbit coupling leads to

a significant decrease in the total removal cross sections of 12.9 Å^2 for transitions from the mixed 8_{18} level to all unperturbed singlet and triplet levels. This should be compared to our earlier estimate of 16.0 Å^2 in the absence of spin-orbit coupling of CH$_2$. Similarly, our estimate for the total removal rate out of the other component of the mixed pair $[\tilde{X}\,9_{37}(0,2,0)]$ is *larger* (8.7 as compared to 5.7 Å^2) when spin-orbit coupling is included. By ignoring spin-orbit coupling, we overestimate the total removal cross sections for the 8_{18} level but underestimate the it for the 9_{37} level.

The comparison in Tab. 6.1 refers to cross sections at a fixed collision energy. The total removal thermal rate constants at 300 K are 1.89×10^{-10} cm^3·molecule^{-1}·s for the 8_{18} level and 1.36×10^{-10} (in the same units) for the 9_{37} level. These two numbers should be compared with the points marked, respectively, "S" and "T" in Fig. 4.10. They are in considerably better agreement with experiment than the calculated rates under the approximation of neglect of spin-orbit coupling [see Fig. 4.10)] but still $\approx 30\%$ higher for the singlet and $\approx 10\%$ higher for the triplet. The overall relaxation from the mixed 9_{37} level is lower than that of the 8_{18} level, since the latter possesses greater singlet character. The degree of disagreement with experiment is comparable to what we have found for other $k_a = 1$ levels. This confirms the accuracy of the mixed-state model for CH$_2$.

In this Chapter we presented a simplistic and more complete simulation of relaxation involving the ground and the first-excited states of CH$_2$, by collisions with He. In the simplistic model, we treated all unperturbed singlet and triplet levels as two large baths. The predicted time evolution of the populations of the two mixed

levels was double exponential: a rapid equilibration of these two levels at short time followed by a slower overall relaxation. The complex simulation reproduced this double-exponential behavior [Fig. 6.7] for the two mixed levels.

We ignored vibrationally inelastic processes, which we believe, based on our work in Chap. 5, will be totally unimportant. In addition, we only included one mixed-pair. The next level of complexity would be to include both (and, even higher) pairs of mixed levels for either of the nuclear-spin modifications of CH_2, see Tab. 2.2. For o-CH_2 we would need to add the $7_{16}/6_{15}$ pair, which are mixed nearly completely. Thus, this more complete relaxation simulation will involve two simultaneous gateways.

We now have a better understanding of $^1\tilde{a} \rightarrow^3 \tilde{X}$ relaxation in CH_2. Whatever the initial conditions, the populations in both components of the mixed pair rapidly equilibrate, and then decay at the same rate. The next most efficient process, is rotational relaxation within the $\tilde{a}$ state, which is ≈ 3 times faster than within the $\tilde{X}$ state. Eventually, the bulk of the population transfers to the $\tilde{X}$ state, not only because of the threefold greater degeneracy of this latter, but because the zero-point levels of both the (0,2,0) and (0,3,0) vibrational manifolds lie lower than the origin of the $\tilde{a}$ state, as seen in Fig 5.2.

Chapter 7:   Global Conclusions and Future Work

Our research goal was to investigate, theoretically, energy transfer within and between the triplet ground state and the singlet first excited state of CH_2, in collisions with the helium atom. To do so we first calculate the $CH_2(\tilde{a}/\tilde{X})$+He potential energy surfaces and then carried out scattering calculations separately for each of the two states. We then investigated purely rotational relaxation within each electronic state, and, in the case of the $\tilde{X}$ state, rovibrational relaxation involving the $v_b = 0, 1, 2$ CH_2 bending vibrational states. We then included the spin-orbit coupling and explored the electronic energy transfer within the mixed-state model.

For the interaction of He with $CH_2(\tilde{a})$, *ab initio* calculations were conducted on a grid of 19 R values and 190 (θ, ϕ) combinations, for a total of 3610 points. The presence of a filled lone pair in the orbital along the molecular axis as well as the total hole in the empty orbital perpendicular to the molecular plane, leads to a significant anisotropy in the potential energy surfaces. At short-range, the largest terms in the expansion of the PES reflect this electronic asymmetry and the repulsion of the He by the two hydrogens.

Again for collisions involving $CH_2(\tilde{a})$, at a collision energy of 300 cm^{-1} the largest state-to-state cross sections are for transitions with $\Delta k_a = 0$, $\Delta n = \pm 1$ and

$\Delta k_a = 2$, $\Delta n = 0$. Here too, we found no correlation between the magnitude of the cross sections and the the energy gap between the initial and final states. For collisions out of levels in the $k_a = 1$ stack, we found strong even-odd alternation in the dependence of the total removal cross sections and room temperature rate constants on the initial CH_2 rotational angular momentum. This propensity is reversed for *ortho* (as compared with *para*) CH_2. This propensity is related to the strong variation in the energy gaps in the $k_a = 1$ stack, which is a consequence of the rotational asymmetry of the CH_2 molecule.

Chapter 5 summarizes out *ab initio* calculations for $CH_2(\tilde{X})$–He PES. Because of the low barrier to linearity in this electronic state, we treated the molecule as a semi-rigid bender with a fixed bond length and a variable bending angle. The grid of *ab initio* calculations was defined by 19 CH_2–He distances, 52 (θ, ϕ) orientation combinations and additional 13 values of the CH_2 bond angle γ, for a total of 12,844 points. We determined the potential energy surface for use in the scattering calculation by averaging the bending-dependent potential weighted by the the square of the bending wave function (in the case of transitions within a vibrational manifold) or by the product of the vibrational wave functions (in the case of transitions inelastic in the bending vibration). Since the $3a_1$ and $1b_1$ orbitals are each singly occupied in the $\tilde{X}$ state, the strongest anisotropy of $CH_2(\tilde{X})$–He PES corresponds to rotation of the He in a plane perpendicular to the molecular plane, and, also, to the repulsion with the two H atoms, as the He rotates around in the plane of the molecule.

Because CH_2 in the $\tilde{X}$ is much less strongly bent (much more linear) the energy splitting between the k_a stacks of the $CH_2(\tilde{X})$ is considerably larger than

that $CH_2(\tilde{a})$. Thus, the rotational inelasticity is primarily confined to a single k_a stack. The largest cross sections at a collision energy of 300 cm^{-1} belong to the transitions with $\Delta k_a = 0$ and $\Delta n = -2$. This transition is directly coupled by the strongest term in the expansion of the anisotropy of the PES.

Because the PES is less anisotropic (compared to that for $CH_2(\tilde{a})$+He), the state-to-state cross sections, as well as the room temperature rate constants, are much smaller. In addition, there is a weaker even-odd alternation with n in the magnitude of the total removal cross sections. This is the affect of a cancellation between an alternation in the $k_a = 1 \rightarrow 0$ cross sections and a reversed alternation in the $k_a = 1 \rightarrow 1$ cross sections.

For collisions of $CH_2(\tilde{X})$ the relative magnitudes of the state-to-state rotational cross sections within a particular bending vibration manifold vary with the bending vibrational quantum number. For example, for transitions out of the 4_{14} level of the *ortho* $CH_2(\tilde{X})$, the largest cross sections belong to different transitions in different $(0,v_b,0)$ vibrational manifolds. This difference in cross sections is again due to the distinction in the energy splitting between the k_a stacks. To fully understand the vibrational energy transfer of the $\tilde{X}$ state, we calculated the interaction between rotational levels in different vibrational manifolds and carried out scattering calculations for the ro-vibrational relaxation within the $\tilde{X}$ state. The ro-vibrational relaxation, is found to be at least of two order of magnitude smaller than the rotational relaxation in a single vibrational manifold of the $\tilde{X}$ state. We then concluded that the vibrational relaxation for CH_2 after collisions with He is ignorable in most circumstances.

For collisions of $CH_2(\tilde{a})$ with He, we compared the total removal rate constants calculated from our scattering calculations to the experimental results reported by Hall and Sears, for transitions out of the $n = 2, 4, 5, 6$ levels of *ortho* $CH_2(\tilde{a})$ in the $k_a = 1$ stack. The calculated removal rate constants were only $\approx 20\%$ higher than the experimental estimates. In particular, the even-odd alternation seen experimentally corresponded identically to our predictions. However, the predicted removal rate for the $n = 8, k_a = 1$ level is $\approx 70\%$ greater than the experimental estimate.

This level forms a nearly degenerate with the $9_{37}(j = 8)$ level in the (0,2,0) vibrational manifold of the $\tilde{X}$ state. These two levels are mixed by the weak spin-orbit coupling. They form a degenerate pair: each level has both singlet and triplet character. This mixed pair can then form a "gateway" for energy transfer between the $\tilde{a}$ state and the triplet rotational levels.

In Chap. 6 we included the mixing between this degenerate pair $(8_{18}/9_{37})$. The cross sections and removal rates of these two mixed levels are strongly effected. The disagreement with experiment drops to $\approx 30\%$ higher (calculation as compared to experiment) for the mixed-pair level of nominal singlet character and only $\approx 10\%$ higher for the level of nominal triplet character.

In the same chapter 6, we solved the full relaxation master equation assuming only one pair of mixed states: 8_{18} and 9_{37}. We can then simulate the kinetic relaxation of all the rotational levels of the $\tilde{a}$ state and the (0,2,0) manifold of the $\tilde{X}$ state. The populations of the two mixed states merge immediately to the same decay rate, and perform double-exponential behaviors as we have predicted using the simple model simulation. At short time the mixed states rapidly achieve an equality

of population. Rotational relaxation then occurs to the other levels of the $\tilde{a}$ state, and, on a somewhat slower timescale, to the other levels of the $\tilde{X}$ state. At very long times, equilibration occurs between the spin-multiplets of the $\tilde{X}$ states. The cross sections for this process are very small, comparable to those for vibrational relaxation.

To sum up, then, in one paragraph, in this dissertation we reported accurate potential energy surfaces, state-to-state and overall removal cross sections, and room temperature rate constants for collisions of He with CH_2, in both its ground and first excited electronic states. We investigated intersystem crossing between the two electronic states by including the small spin-orbit coupling of pairs of gateway states. In addition, we initiated a detailed simulation on relaxation kinetics of CH_2 by solving the relaxation master equation, to help in understanding collisional-induced electronic energy transfer in small molecules like CH_2. This work is the first investigation of rotational-electronic relaxation in collisions of a polyatomic molecule.

In future work, we can extend the scattering calculation for energy transfer between the $\tilde{a}$ and the $\tilde{X}$ rotational levels by including both $[8_{18}/9_{37}(0,2,0)]$ and $[7_{16}/6_{15}(0,3,0)]$ gateway pairs of *ortho* CH_2, in a single calculation. In Sec. 2.2.4 we demonstrated how to calculate the two-state (with one gateway pair) T-matrix elements from the T-matrix elements for collisions of He with, separately, $CH_2(\tilde{a})$ and $CH_2(\tilde{X})$. For a system with both gateway pairs, the equations in Sec. 2.2.4 are still valid in calculating the T-matrix elements for transitions between an unmixed level and a gateway state, as well as for transitions between two paired gateway

states.

The calculation for the T-matrix elements for transitions between gateway pairs (for example, $8_{18} \rightarrow 7_{16}$), which is not discussed in detail in this dissertation, will be more complicated. As the wave functions of both pairs can be written as linear combinations of the pure singlet and triplet states, the transition between two unpaired gateway states will involve two mixing angles. It will be of interest and challenge to explore these transitions. The total removal rate constant for the $\tilde{a}$ 8_{18} level is expected to be even closer to the experimental result.

Once determine the cross sections for transitions between unpaired gateway states, we can calculate the corresponding rate constants. The master equation simulation can then be expanded by including the interference between two different gateways ($[8_{18}/9_{37}(0,2,0)]$ and $[7_{16}/6_{15}(0,3,0)]$ for o-CH_2). This proposed simulation will involve three vibrational manifolds: both $(0,2,0)$ and $(0,3,0)$ of the $\tilde{X}$ state as well as $(0,0,0)$ of the $\tilde{a}$ state.

In this dissertation, we used a fixed collisional partner, He. Further investigation can be carried out using another collider, for example, Ar. We can then evaluate the dependence of the efficiency of the gateway on collision partners and compare the results with Gannon and Seakin's experiment (see Sec. 2.3).

Appendix A: Symmetry of CH_2 Wave Functions (with respect to Interchange of the Two H Nuclei)

This Appendix draws heavily from some earlier, unpublished notes by Dr. Paul Dagdigian.

Fermi-Dirac statistics apply to electrons, but also to protons, neutrons, and, in general, nuclei with odd mass numbers. Nuclei with even mass numbers obey Bose-Einstein statistics. [16]

The total wave function of a molecule can be written, formally, as

$$\Phi_{tot} = \Phi_{el} \ \Phi_{vib} \ \Phi_{rot} \ \Phi_{ns}, \tag{A.1}$$

where Φ_{el}, Φ_{vib}, Φ_{rot} and Φ_{ns} are, respectively, the wave functions for the electronic, vibrational, rotational and nuclear spin degrees of freedom. The CH_2 molecule has two H atoms. Since these are fermions, Φ_{tot} must be anti-symmetric with respect to the interchange of the two hydrogens.

In the coordinate system we are using in this dissertation, [Fig. 2.5], the interchange of the two hydrogens in CH_2 is equivalent to a rotation of $180°$ around the x axis, the C_2 axis for the molecule. Thus the total wavefunction must be

anti-symmetric with respect to this operation:

$$\hat{C}_2(x)\ \Phi_{tot} = -\Phi_{tot}. \tag{A.2}$$

The symmetry of the rotational wavefunction of a asymmetric top around the b axis (also x axis in our coordinate system) is given by [34]

$$\hat{C}_2(x)\ |njk_ak_c\rangle = (-1)^{k_a-k_c}\ |njk_ak_c\rangle. \tag{A.3}$$

Although the bending vibrational wavefunction is always symmetric with respect to $\hat{C}_2$, the electronic wavefunctions in the $\tilde{a}$ and $\tilde{X}$ states have different symmetries.

a) The $^3\tilde{X}$ ground state

The overall symmetry of the electronic wave function in the ^3X state is B_1. As shown in Table 2.1,

$$\hat{C}_2(x)\ |B_1\rangle = -|B_1\rangle. \tag{A.4}$$

Thus the electronic wavefunction is anti-symmetric with respect to this operation.

Just as in the H_2 molecule, in the *ortho* nuclear spin species the nuclear spin wavefunction is symmetric with respect to exchange of the two H atoms. Consequently, the symmetry of the total wavefunction for CH_2 in its ground electronic state is

$$\hat{C}_2(x)\ \Phi_{tot}^{(o),B_1} = (-1)^{k_a-k_c+1}\ \Phi_{tot}^{(o),B_1}, \tag{A.5}$$

here the superscript (o) designates *ortho*. Comparing this equation to Eq. (A.2),

we see that the only allowed rotational levels for the *ortho* nuclear spin species are those for which $k_a + k_c =$ even (k_a and k_c must be both even or both odd).

Similarly, in the *para* species, the nuclear spin wave function is antisymmetric with respect to exchange of the two H atoms. Thus,

$$\hat{C}_2(x) \ \Phi_{tot}^{(p),B_1} = (-1)^{k_a - k_c} \ \Phi_{tot}^{(p),B_1}, \tag{A.6}$$

which tells us that for p-CH$_2$ the only rotational levels allowed are those for which $k_a + k_c =$ odd.

b) The $\tilde{a}$ state

The only difference between the $\tilde{a}$ state and the $\tilde{X}$ state CH$_2$ of relevance to the discussion here is the symmetry of the electronic wavefunction with respect to the interchange of the two hydrogens. The overall symmetry of the ground state is A_1, where,

$$\hat{C}_2(x) \ |A_1\rangle = +|A_1\rangle, \tag{A.7}$$

which is opposite to the symmetry of the ground state. Thus the attribution of rotational levels to the *ortho* and *para* nuclear spin species is reversed in the $\tilde{a}$ state: odd values of $k_a + k_c$ are associated with the *ortho* species, while even values of $k_a + k_c$ are associated with the *para* species.

Appendix B: Spin-orbit Coupling in the $\tilde{X}\,^3B_1$ state of CH_2

This appendix, originally written by Dr. Millard Alexander, but unpublished, is included in this dissertation for completeness.

B.1 Linear Molecules

For a molecule with π^2 electron occupancy, as, for example NH, OH^+, or linear CH_2 and linear H_2O^+, there are three valence electronic states: $^3\Sigma^-$, $^1\Delta$, and $^1\Sigma^+$. Their Slater determinantal wave functions are:

$$\left|^3\Sigma^-, M_S = 1\right\rangle = |\pi_1 \pi_{-1}|$$

then, by application of the operator $S_- = s_{1-} + s_{2-}$,

$$\left|^3\Sigma^-, M_S = 0\right\rangle = 2^{-1/2}\left(|\pi_1 \bar{\pi}_{-1}| + |\bar{\pi}_1 \pi_{-1}|\right)$$

and

$$\left|^3\Sigma^-, M_S = -1\right\rangle = |\bar{\pi}_1 \bar{\pi}_{-1}|$$

Also

$$\left|^1\Delta, M_L = 2\right\rangle = |\pi_1\bar{\pi}_1|$$

and

$$\left|^1\Delta, M_L = -2\right\rangle = |\pi_{-1}\bar{\pi}_{-1}|$$

Finally, since the $^1\Sigma^+$ and $^3\Sigma^-$, $M_S = 0$ states are orthogonal, we have

$$\left|^1\Sigma^+\right\rangle = 2^{-1/2}\left(|\pi_1\bar{\pi}_{-1}| - |\bar{\pi}_1\pi_{-1}|\right)$$

As Hund's rules [16] predict, the lowest state energetically is $^3\Sigma^-$, followed by $^1\Delta$ and, successively, by $^1\Sigma^+$.

If we neglect spin-other-orbit terms, then the spin-orbit coupling can be represented as a one electron operator

$$\hat{h}_{so} = a\left[\hat{l}_z\hat{s}_z + \frac{1}{2}\left(\hat{l}_+\hat{s}_- + \hat{l}_-\hat{s}_+\right)\right]$$

where a is a constant. The spin-orbit operator for the two-electron system is

$$\hat{H}_{so}(1,2) = \hat{h}_{so}(1) + \hat{h}_{so}(2)$$

The only non-vanishing elements of $\hat{H}_{so}$ are between the $^1\Sigma^+$ and the $M_S = 0$ component of the $^3\Sigma^-$ state. Specifically, these are coupled by the $\hat{l}_z\hat{s}_z$ term. We find

$$\left\langle^1\Sigma^+\right|\hat{H}_{so}\left|^3\Sigma^-\right\rangle = a$$

B.2 Molecules with C_{2v} Symmetry

When a triatomic linear molecule bends, the electronic states take on one of the C_{2v} symmetry characters. Specifically, the $^1\Sigma^+$ state ($x^2 + y^2$ in character) and the $x^2 - y^2$ component of the $^1\Delta$ state become states of $^1A_1$ symmetry, the xy component of the $^1\Delta$ state becomes a state of $^1B_1$ symmetry, and the $^3\Sigma^-$ state becomes a state of $^3B_1$ symmetry. The two states of $^1A_1$ symmetry mix, substantially so as the bending increases. In a 3-state model, one can write the wave functions at any HCH angle θ as

$$\left|1_1^A\right\rangle = \cos\gamma \left|^1\Delta_{x^2-y^2}\right\rangle + \sin\gamma \left|^1\Sigma^+\right\rangle$$

and

$$\left|2_1^A\right\rangle = -\sin\gamma \left|^1\Delta_{x^2-y^2}\right\rangle + \cos\gamma \left|^1\Sigma^+\right\rangle$$

where the "mixing angle" γ vanishes in linear geometry. Thus, the matrix of the spin-orbit operator is

$$
\hat{\mathbf{H}}_{so} =
\begin{bmatrix}
 & 1^1A_1 & 2^1A_1 & ^3B_1(M_S = 0) \\
\hline
1^1A_1 & 0 & 0 & a\sin\gamma \\
2^1A_1 & 0 & 0 & a\cos\gamma \\
^3B_1(M_S = 0) & a\sin\gamma & a\cos\gamma & 0
\end{bmatrix}
$$

so that

$$\gamma = \arctan\left(\langle 1^1A_1|\,\hat{H}_{so}\,|^3B_1\rangle \,/\, \langle 2^1A_1|\,\hat{H}_{so}\,|^3B_1\rangle\right)$$

B.3 Results for the CH_2 Molecule

We carried out a three-state CASSCF calculation on the CH_2 molecule as a function of the HCH angle, using the MOLPRO program suite. [51] The results, with an *avtz* basis, are presented in Fig. B.1. We see that the spin-orbit coupling is
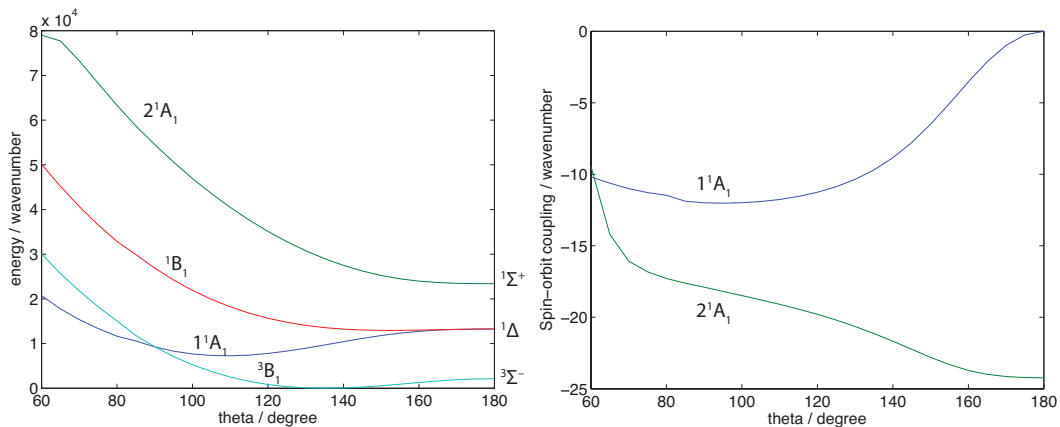

Figure B.1: (Left panel) Energies of the CH_2 molecule as a function of the HCH angle; *avtz* basis, CASSCF, 4,1,1 active space. (Right panel) Spin-orbit coupling matrix elements between the $^3B_1$ state and the 1^1A_1 and 2^1A_1 states.

on the order of 10's of wave numbers.

In reality, the coupling must be averaged over the product of the vibrational wave functions of the $^3B_1$ and the 1^1A_1 states. Since the former is much less bent than the latter, the Franck-Condon overlap will be substantially less than unity, so that these matrix elements will be reduced, resulting in spin-orbit coupling on the order of a few wave numbers, as reported by Bley and Temps. [10]

Bibliography

[1] M. J. Perkins, *Radical Chemistry: The Fundamentals* (Oxford University Press, New York, 2000), p. 83.

[2] C. Wentrup, *Reactive Molecules: The Neutral Reactive Intermediates in Organic Chemistry* (John Wiley & Sons, New York, 1984), p. 162.

[3] S. P. McManus, *Organic Reactive Intermediates* (Academic Press, New York and London, 1973), p. 61.

[4] T. J. Frankcombe and S. C. Smith, Farad. Discuss. **119**(1), 159 (2001).

[5] W. M. Shaub and M. C. Lin, in *Laser Probes for Combustion Chemistry*, edited by D. R. Crosley (American Chemical Society, Washington D. C., 1980), p. 408.

[6] J. S. Levine, in *The Photochemistry of Atmospheres: EARTH, THE OTHER PLANETS AND COMETS* (Academic Press Inc., London, 1985), p. 15.

[7] Y. L. Yung and W. B. DeMore, *Photochemistry of Planetary Atmospheres* (Oxford University Press, New York, 1999), p. 144.

[8] D. F. Strobel, in *The Photochemistry of Atmospheres: EARTH, THE OTHER PLANETS AND COMETS*, edited by J. S. Levine (Academic Press Inc., London, 1985), p. 428.

[9] D. L. Baulch, C. T. Bowman, C. J. Cobos, R. A. Cox, T. Just, J. A. Kerr, M. J. Pilling, D. Stocker, J. Troe, W. Tsang, *et al.*, J. Phys. Chem. Ref. Data **34**(3), 757 (2005).

[10] U. Bley and F. Temps, J. Chem. Phys. **98**(2), 1058 (1993).

[11] K. Kobayashi, G. E. Hall, and T. J. Sears, J. Chem. Phys. **124**(18), 184320 (2006).

[12] A. V. Komissarov, A. Lin, T. J. Sears, and G. E. Hall, J. Chem. Phys. **125**(8), 084308 (2006).

[13] Z. Wang, Y. Kim, G. E. Hall, and T. J. Sears, J. Phys. Chem. A **112**(39), 9248 (2008).

[14] G. E. Hall and T. J. Sears, private communications (2010–2013).

[15] K. L. Gannon, M. A. Blitz, T. Kovacs, M. J. Pilling, and P. W. Seakins, J. Chem. Phys. **132**(2), 024302 (2010).

[16] J. I. Steinfeld, *Molecules and Radiation: An Introduction to Modern Molecular Spectroscopy* (Dover Publications, Cambridge, Mass, 2005).

[17] L. Ma, M. H. Alexander, and P. J. Dagdigian, J. Chem. Phys. **135**(4), 154307 (2011).

[18] L. Ma, P. J. Dagdigian, and M. H. Alexander, J. Chem. Phys. **136**(22), 224306 (2012).

[19] P. R. Bunker, P. Jensen, W. P. Kraemer, and R. Beardsworth, J. Chem. Phys. **85**(7), 3724 (1986).

[20] M. N. R. Ashfold, M. A. Fullstone, G. Hancock, and G. W. Ketley, Chem. Phys. **55**(2), 245 (1981).

[21] A. O. Langford, H. Petek, and C. Moore, J. Chem. Phys. **78**(11), 6650 (1983).

[22] G. Hancock and V. Haverd, Chem. Phys. Lett. **372**(1-2), 288 (2003).

[23] W. R. Kuhn, S. K. Atreya, and S. Chang, Geophys. Res. Lett. **4**(5), 203 (1977).

[24] F. Hayes, W. Lawrance, W. Staker, and K. King, J. Phys. Chem. **100**(27), 11314 (1996).

[25] M. A. Blitz, M. J. Pilling, and P. W. Seakins, Phys. Chem. Chem. Phys. **3**(12), 2241 (2001).

[26] D. C. Darwin, A. T. Young, H. S. Johnston, and C. B. Moore, J. Phys. Chem. **93**(3), 1074 (1989).

[27] R. A. Alvarez and C. B. Moore, J. Phys. Chem. **98**(1), 174 (1994).

[28] V. Seidler, F. Temps, H. G. Wagner, and M. Wolf, J. Phys. Chem. **93**(3), 1070 (1989).

[29] Y. Hidaka, K. Hattori, T. Okuno, K. Inami, T. Abe, and T. Koike, Combust. Flame **107**(4), 401 (1996).

[30] M. J. Pilling, J. Phys. Chem. A **117**(18), 3697 (2013).

[31] P. Jensen, P. R. Bunker, and A. R. Hoy, J. Chem. Phys. **77**(11), 5370 (1982).

[32] H. Petek, D. J. Nesbitt, D. C. Darwin, P. R. Ogilby, C. B. Moore, and D. A. Ramsay, J. Chem. Phys. **91**(11), 6566 (1989).

[33] G. V. Hartland, D. Qin, and H. L. Dai, J. Chem. Phys. **102**(17), 6641 (1995).

[34] C. H. Townes, *Microwave Spectroscopy* (Dover Publications, New York, 1975).

[35] P. F. Bernath, *Spectra of Atoms and Molecules* (Oxford University Press, New York, 2005).

[36] D. M. Brink and G. R. Satchler, *Angular Momentum* (Clarendon Press, Oxford, 1968), p. 146.

[37] T. J. Sears, P. R. Bunker, A. R. W. McKellar, K. M. Evenson, D. A. Jennings, and J. M. Brown, J. Chem. Phys. **77**(11), 5348 (1982).

[38] H. Petek, D. J. Nesbitt, D. C. Darwin, and C. B. Moore, J. Chem. Phys. **86**(3), 1172 (1987).

[39] H. Petek, D. J. Nesbitt, C. B. Moore, F. W. Birss, and D. A. Ramsay, J. Chem. Phys. **86**(3), 1189 (1987).

[40] M. D. Marshall and A. R. W. Mckellar, J. Chem. Phys. **85**(7), 3716 (1986).

[41] W. M. Gelbart and K. F. Freed, Chem. Phys. Lett. **18**(4), 470 (1973).

[42] B. Pouilly, J. M. Robbe, and M. H. Alexander, J. Phys. Chem. **88**(1), 140148 (1984).

[43] K. F. Freed, in *Potential Energy Surfaces*, edited by K. P. Lawley (John Wiley & Sons, New York, 1980), p. 207.

[44] M. E. Jacox, J. Phys. Chem. Ref. Data **32**(1), 1 (2003).

[45] HIBRIDON is a package of programs for the time-independent quantum treatment of inelastic collisions and photodissociation written by M. H. Alexander, D. E. Manolopoulos, H.-J. Werner, B. Follmeg, Q. Ma, and P. J. Dagdigian, with contributions by P. F. Vohralik, D. Lemoine, G. Corey, R. Gordon, B. Johnson, T. Orlikowski, A. Berning, A. Degli-Esposti, C. Rist, B. Pouilly, G. van der Sanden, M. Yang, F. de Weerd, S. Gregurick, J. Klos and F. Lique. More information and/or a copy of the code can be obtained from the website http://www2.chem.umd.edu/groups/alexander/hibridon/hib43.

[46] G. E. Hall, A. V. Komissarov, and T. J. Sears, J. Phys. Chem. A **108**(39), 7922 (2004).

[47] C. C. Hayden, D. M. Neumark, K. Shobatake, R. K. Sparks, and Y. T. Lee, J. Chem. Phys. **76**(7), 3607 (1982).

[48] M. H. Alexander, G. E. Hall, and P. J. Dagdigian, J. Chem. Educ. **88**(11), 1538 (2011).

[49] I. N. Levine, *Quantum Chemistry (5th Edition)* (Prentice Hall, New Jersey, 1999), p. 366.

[50] M. Born and J. R. Oppenheimer, Ann. Phys. (Berlin) **85**(1), 458 (1927).

[51] H.-J. Werner, P. J. Knowles, G. Knizia, F. R. Manby, M. Schütz, P. Celani, T. Korona, R. Lindh, A. Mitrushenkov, G. Rauhut, *et al.*, *Molpro, version 2012.1, a package of ab initio programs* (2012), see http://www.molpro.net.

[52] K. Raghavachari, G. W. Trucks, J. A. Pople, and M. Head-Gordon, Chem. Phys. Lett. **157**(6), 479483 (1989).

[53] C. Hampel, K. A. Peterson, and H. J. Werner, Chem. Phys. Lett. **190**(1-2), 1 (1992).

[54] R. J. Bartlett, in *Modern Electronic Structure Theory, Part II*, edited by D. R. Yarkony (World Scientific, Singapore, 1995), p. 1047.

[55] F. M. Floris and A. Tani, in *Molecular Dynamics: From Classical to Quantum Methods*, edited by P. B. Balbuena and J. M. Seminario (Elsevier, Amsterdam, 1999), p. 369.

[56] T. Helgaker and P. R. Taylor, in *Modern Electronic Structure Theory, Part II*, edited by D. R. Yarkony (World Scientific, Singapore, 1995), p. 783.

[57] S. F. Boys and F. Bernardi, Mol. Phys. **19**(4), 553 (1970).

[58] R. A. Kendall, T. H. Dunning, and R. J. Harrison, J. Chem. Phys. **96**(9), 6796 (1992).

[59] F. M. Tao and Y. K. Pan, J. Chem. Phys. **97**(7), 4989 (1992).

[60] H. Koch, B. Fernandez, and O. Christiansen, J. Chem. Phys. **108**(7), 2784 (1998).

[61] A. M. Arthurs and A. Dalgarno, Proc. Roy. Soc. London Ser. A **256**(1287), 540 (1960).

[62] H. Goldstein, C. P. J. Poole, and J. L. Safko, *Classical Mechanics, 3rd Edition* (Addison-Wesley, San Francisco, 2000).

[63] S. Green, J. Chem. Phys. **64**(8), 3463 (1976).

[64] D. A. Varshalovich, A. N. Moskalev, and V. K. Khersonski, *Qauntovya Theoria Uglovogo Momenta (in Russian)* (Nauka, Moscow, 1969).

[65] D. A. Varshalovich, A. N. Moskalev, and V. K. Khersonski, *Quantum Theory of Angular Momentum* (World Scientific, Singapore, 1988).

[66] P. L. Houston, *Chemical Kinetics and Reaction Dynamics* (Courier Dover Publications, New York, 2006).

[67] I. W. M. Smith, *Kinetics and Dynamics of Elementary Gas Reaction* (Buttersworths, London, 1980).

[68] P. J. Dagdigian, in *The Chemical Dynamics and Kinetics of Small Radicals, Part I*, edited by K. Liu and A. F. Wagner (World Scientific, Singapore, 1995), p. 315.

[69] A. Schiffman and D. W. Chandler, Int. Rev. Phys. Chem. **14**(2), 371 (1995).

[70] M. H. Alexander, X. Yang, P. J. Dagdigian, A. Berning, and H.-J. Werner, J. Chem. Phys. **112**(2), 781 (2000).

[71] M. Islam, I. W. M. Smith, and M. H. Alexander, Phys. Chem. Chem. Phys. **2**(4), 473 (2000).

[72] M. Kind, F. Stuhl, Y. R. Tzeng, M. H. Alexander, and P. J. Dagdigian, J. Chem. Phys. **114**(10), 4479 (2001).

[73] K. M. Hickson, C. M. Sadowski, and I. W. M. Smith, Phys. Chem. Chem. Phys. **4**(22), 5613 (2002).

[74] D. A. Hostutler, T. C. Smith, G. D. Hager, G. C. McBane, and M. C. Heaven, J. Chem. Phys. **120**(16), 7483 (2004).

[75] A. Khachatrian, P. J. Dagdigian, D. I. G. Bennett, F. Lique, J. Klos, and M. H. Alexander, J. Phys. Chem. A **113**(16), 3922 (2009).

[76] P. E. S. Wormer, J. A. Klos, G. C. Groenenboom, and A. van der Avoird, J. Chem. Phys. **122**(24), 244325 (2005).

[77] A. K. Dham, G. C. McBane, F. R. W. McCourt, and W. J. Meath, J. Chem. Phys. **132**(2), 024308 (2010).

[78] F. Lique, A. Spielfiedel, N. Feautrier, I. F. Schneider, J. Klos, and M. H. Alexander, J. Chem. Phys. **132**(2), 024303 (2010).

[79] P. J. Dagdigian, J. Chem. Phys. **90**(5), 2617 (1989).

[80] S. J. Dearden, R. N. Dixon, and D. Field, J. Chem. Soc. Faraday Trans. II **78**(8), 1423 (1982).

[81] J. Schleipen, J. J. Termeulen, G. C. M. van der Sanden, P. E. S. Wormer, and A. van der Avoird, Chem. Phys. **163**(2), 161 (1992).

[82] H. Meyer, J. Chem. Phys. **101**(8), 6686 (1994).

[83] G. C. M. van der Sanden, P. E. S. Wormer, A. van der Avoird, J. Schileipen, and J. J. Termeulen, J. Chem. Phys. **97**(9), 6460 (1992).

[84] W. B. Chapman, A. Schiffman, J. M. Hutson, and D. J. Nesbitt, J. Chem. Phys. **105**(9), 3497 (1996).

[85] W. B. Chapman, A. Kulcke, B. W. Blackmon, and D. J. Nesbitt, J. Chem. Phys. **110**(17), 8543 (1999).

[86] J. A. Miller, R. J. Kee, and C. K. Westbrook, Annu. Rev. Phys. Chem. **41**, 345 (1990).

[87] A. J. Orr-Ewing and R. N. Zare, Annu. Rev. Phys. Chem. **45**(1), 315 (1994).

[88] A. J. McCaffery, M. J. Proctor, and B. J. Whitaker, Annu. Rev. Phys. Chem. **37**(1), 223 (1986).

[89] M. C. van Beek, G. Berden, H. L. Bethlem, and J. J. ter Meulen, Phys. Rev. Lett. **86**(18), 4001 (2001).

[90] E. A. Wade, K. T. Lorenz, D. W. Chandler, J. W. Barr, G. L. Barnes, and J. I. Cline, Chem. Phys. **301**(2-3), 261 (2004).

[91] Y. Kim, H. Meyer, and M. H. Alexander, J. Chem. Phys. **121**(3), 1339 (2004).

[92] M. Brouard, A. Bryant, Y. P. Chang, R. Cireasa, C. J. Eyles, A. M. Green, S. Marinakis, F. J. Aoiz, and J. Klos, J. Chem. Phys. **130**(4), 044306 (2009).

[93] G. Paterson, S. Marinakis, M. L. Costen, and K. G. McKendrick, Phys. Scripta **80**(4), 048111 (2009).

[94] B. J. Garrison, W. A. Lester, and W. H. Miller, J. Chem. Phys. **65**(6), 2193 (1976).

[95] A. Palma, S. Green, D. J. Defrees, and A. D. Mclean, J. Chem. Phys. **89**(3), 1401 (1988).

[96] M. J. O. Deegan and P. J. Knowles, Chem. Phys. Lett. **227**(3), 321 (1994).

[97] P. J. Dagdigian and M. Alexander, Mol. Phys. **108**(7-9), 1159 (2010).

[98] K. Patkowski, T. Korona, R. Moszynski, B. Jeziorski, and K. Szalewicz, J. Mol. Struct.: THEOCHEM **591**(1-3), 231 (2002).

[99] H. W. Kroto, *Molecular Rotation Spectra* (Courier Dover Publications, New York, 1992).

[100] B. J. Whitaker and P. Bréchignac, Laser Chem. **6**(1), 61 (1986).

[101] S. Green, Chem. Phys. **40**(1-2), 1 (1979).

[102] C. H. Chang, G. E. Hall, and T. J. Sears, J. Chem. Phys. **133**(14), 144310 (2010).

[103] G. Herzberg, *Molecular Spectra and Molecular Structure: III. Electronic Spectra and Electronic Structure of Polyatomic Molecules* (D. Van Nostrand, Princeton, 1967).

[104] A. D. Walsh, J. Chem. Soc. **466**(1), 2260 (1953).

[105] J. T. Hougen, P. R. Bunker, and J. W. C. Johns, J. Mol. Spectrosc. **34**(1), 136 (1970).

[106] P. R. Bunker and B. M. Landsberg, J. Mol. Spectrosc. **67**(1-3), 374 (1977).

[107] P. J. Knowles, C. Hampel, and H.-J. Werner, J. Chem. Phys. **99**(7), 5219 (1993).

[108] P. J. Knowles, C. Hampel, and H.-J. Werner, J. Chem. Phys. **112**(6), 3106 (2000).

[109] Initially, we used 23 expansion terms ($0 \leq \lambda \leq 8$, $0 \leq \mu \leq 6$, with $\lambda + \mu$ constrained by symmetry to even values) to fit the 52 points. We subsequently found that for these geometries, the [$\lambda = 7$, $\mu = 1$], [8,0] and [8,2] expansion terms were not linearly independent of the other terms. Consequently, these three terms were eliminated from the expansion in Eq. (5.4).

[110] T. V. Tscherbul, T. A. Grinev, H. G. Yu, A. Dalgarno, J. Klos, L. Ma, and M. H. Alexander, J. Chem. Phys. **137**(10), 104302 (2012).

[111] A contour plot of the repulsive region of the $CH_2(\tilde{X})$–He PES is contained in supporting information at http://dx.doi.org/10.1063/1.4729050.

[112] This illustrates the advantage of expanding the atom-hydride PES in spherical harmonics oriented along the principal axis, [17, 97] rather than around the symmetry axis. [63] Only in the former case can we infer directly which rotational levels will be coupled by the largest terms in the expansion of the PES.

[113] P. Jensen and P. R. Bunker, J. Chem. Phys. **89**(3), 1327 (1988).

[114] P. Jensen, J. Mol. Spectrosc. **128**(2), 478 (1988).

[115] P. Jensen, private communication (2010).

[116] For an electronic state with non-zero electron angular momentum, the rotational angular momentum is denoted as n and the total total angular momentum by j.

[117] Numerical values for all the cross sections shown in Figs. 5.8 and 5.10 are tabulated in supporting information at http://dx.doi.org/10.1063/1.4729050.

[118] In any singlet state, such as $CH_2(\tilde{a})$, the total molecular angular momentum j is equal to the rotational angular momentum of the nuclei n.

[119] Q. Ma, P. J. Dagdigian, and M. H. Alexander, J. Chem. Phys. **138**(10), 104317 (2013).

[120] P. J. Dagdigian, Int. Rev. Phys. Chem. **32**(2), 229 (2013).

[121] M. H. Alexander, J. Chem. Phys. **76**(7), 3637 (1982).

[122] G. C. Corey and F. R. McCourt, J. Phys. Chem. **87**(15), 2723 (1983).

[123] A. R. Edmonds, *Angular Momentum in Quantum Mechanics* (Princeton University Press, Princeton, 1974), 2nd ed.

[124] G. C. Corey, M. H. Alexander, and J. Schaefer, J. Chem. Phys. **85**(5), 2726 (1986).

[125] M. H. Alexander and P. J. Dagdigian, J. Chem. Phys. **83**(5), 2191 (1985).